2008-12-07

Investigation of Heterogeneity of FSW Inconel 718 Coupled with Welding Thermal Cycle

Dong Fang Huang
Brigham Young University - Provo

INVESTIGATION OF HETEROGENEITY OF FSW INCONEL 718 COUPLED WITH WELDING THERMAL CYCLES

by

Dongfang Huang

A dissertation submitted to the faculty of

Brigham Young University

in partial fulfillment of the requirements for the degree of

Doctor of Philosophy

Department of Mechanical Engineering

Brigham Young University

April 2009

BRIGHAM YOUNG UNIVERSITY

GRADUATE COMMITTEE APPROVAL

of a dissertation submitted by

Dongfang Huang

This dissertation has been read by each member of the following graduate committee and by majority vote has been found to be satisfactory.

Date	Carl D. Sorensen
Date	Tracy Nelson
Date	Michael P. Miles
Date	Robert H. Todd
Date	Brian D. Jensen

BRIGHAM YOUNG UNIVERSITY

As chair of the candidate's graduate committee, I have read the dissertation of Dongfang Huang in its final form and have found that (1) its format, citations, and bibliographical style are consistent and acceptable and fulfill university and department style requirements; (2) its illustrative materials including figures, tables, and charts are in place; and (3) the final manuscript is satisfactory to the graduate committee and is ready for submission to the university library.

Date

Carl D. Sorensen
Chair, Graduate Committee

Accepted for the Department

Larry L. Howell
Graduate Coordinator

Accepted for the College

Alan R. Parkinson
Dean, Ira A. Fulton College of Engineering and Technology

ABSTRACT

INVESTIGATION OF HETEROGENEITY OF FSW INCONEL 718

COUPLED WITH WELDING THERMAL CYCLES

Dongfang Huang

Department of Mechanical Engineering

Doctor of Philosophy

In order to develop a better understanding of the property, microstructure evolution and thermal history of FSW Inconel 718's, the strain, strain rate and thermal cycles need to be determined.

The strain field in a deformed body can be determined if the displacement field is known. However, the displacement field is generally unknown. For an arbitrary linear displacement function, the displacement field can be determined from three orthogonal shape measurements. Three orthogonal planes cut a rectangular box deformed by a linear displacement function, which leads to deformed quadrilaterals in one each of 3 planes. The shape parameters (L, H, θ_1 and θ_2) on the three orthogonal planes can be expressed as the functions of displacement coefficients. Although the displacement coefficients

cannot be expressed in the forms of the shape parameters symbolically, a numerical solution can be found using numerical optimization methods. The shape parameters were obtained from 3 different sets of known displacement coefficients. Numerical optimization was carried out to determine the displacement coefficients. The solved displacement coefficients are the same as the assumed ones, which shows that this inverse problem can be solved, and this method is robust.

A numerical/experimental methodology was developed to estimate the thermal history in the stir zone of FSW Inconel 718.The thermocouple experiment was conducted to measure the thermal cycles in Heat Affected Zone (HAZ). Using the measured temperature in HAZ and a numerical model, the peak temperature (1039 ºC) and cooling rate (58.18 ºC/s) were determined. The microstructure in different regions was characterized and co-related with the thermal cycles. In order to understand the microstructure evolution in the stir zone, the strain rate (12.6 s^{-1}) was estimated using the mathematical model as mentioned above. According to the estimated thermal history and strain rate, the assumption that the dynamic recrystallizaiton occurred during FSW was made. The grain size in the nugget zone affects the hardness. The relationship among the microstructure, mechanical properties, and thermal cycles is discussed.

ACKNOWLEDGMENTS

I would like to first thank my parents, for their encouragement and patience throughout this process.

I would also like to thank my advisor Dr. Carl D. Sorensen, this project would not have been possible without his support and direction. I would also like to thank my graduate committee for their help and guidance and my colleagues in the Friction Stir Research Lab for learning along with me.

TABLE OF CONTENTS

LIST OF TABLES

LIST OF FIGURES

1 Introduction

1.1 Background

Friction Stir Welding (FSW), a process invented at TWI, Cambridge, England, involves the joining of metals without fusion or filler materials. It is used already in both routine and critical applications, for the joining of structural components made of aluminum and its alloys. Indeed, it has been convincingly demonstrated that the process results in strong and ductile joints, sometimes in systems which have proved difficult for conventional welding techniques [1, 2]. The welds are created by the combined action of frictional heating and mechanical deformation due to a rotating tool. The maximum temperature reached is of the order of 0.8 of the melting temperature.

The process advantages result from the fact that the FSW process (as all friction welding of metals) takes place in the solid phase below the melting point of the material to be joined [2, 3]. The benefits therefore include the ability to join materials which are difficult to fusion weld, for example 2000 and 7000 aluminum alloys. Other advantages are as follows: low distortion, even in long welds; excellent mechanical properties as proven by fatigue, tensile and bend tests; no arc, fume, and porosity; low shrinkage; can operate in all positions; energy efficient.

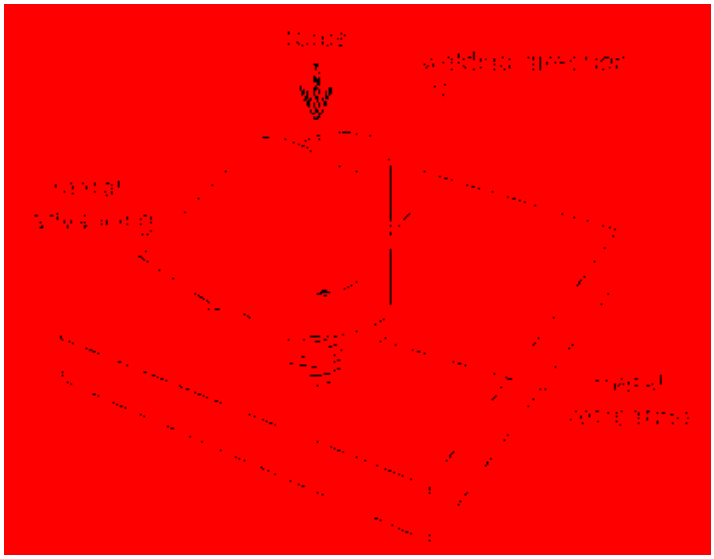

Figure 1-1 Friction stir welding

In the early stages, FSW was applied to aluminum and its alloys. Later on, as the technology has been improved, FSW can be applied to high melting temperature materials such as nickel based alloys. But, only have limited knowledge of the FSW process applied to nickel based alloys. In particular, developing a better understanding of the microstructure, mechanical properties, thermal cycles across the weld, and the relationship between thermal cycles and microstructure is desired. The thermal cycles affect the microstructure evolution in every thermal zone such as the stir zone, heat affected zone (HAZ) and thermal mechanical affected zone (TMAZ). The strain and strain rate also govern the microstructure evolution in the nugget. Therefore, determination of the strain rate is necessary for us to understand the change of the microstructure in the nugget zone as the process is applied.

In order to know the thermal cycles produced during FSW of Inconel 718, a 3D thermocouple experiment needs to be conducted. The experimental results, the numerical

model, and the precipitates observation help to estimate the thermal history in the nugget zone. For a better understanding of the nugget zone, the microstructure is characterized using stereological methods, which allows us to obtain a complete 3 dimensional picture of the grains in the nugget zone. Estimation of the strain field is always a challenging task, since it depends on the displacement function, and the displacement function is difficult to determine. A model to estimate the displacement coefficients of a displacement function is required in order to estimate the strain rate. As a result, combined with the estimated thermal cycles, we will be able to understand the microstructure in the nugget zone. Therefore, determination of the strain rate in the nugget zone is necessary in the study of the FSW Inconel 718.

1.2 Objective

The objectives of the current study include: (1) Develop a 3D mathematical model to determine the displacement coefficients. (2) Reveal how the thermal cycles of FSW Inconel 718 govern its microstructure and properties. (3) Develop a better understanding of the microstructure evolution at the boundary of the stir zone through estimation of the thermal cycles and strain rate in the stir zone.

1.3 About this Dissertation

This dissertation is composed of two papers that will be submitted for publication. The two papers are: (a) Estimation of Three Dimensional Strains from Three Orthogonal Planes and (b) Investigation of Heterogeneity of Inconel 718 Coupled with Welding Thermal Cycles.

2 Determine Linear Displacement Coefficients Using A 3D Deformation Model

2.1 Introduction

Determination of a 3D strain field is a fundamental objective when we study such fields as materials and mechanics. This paper describes a method to determine the 3D strain field by finding the displacement coefficients from the measurement of the microstructure in three orthogonal planes. The 3D strain field is a function of displacement coefficients [4], which can be determined by measuring the shape parameters of the microstructure in three orthogonal planes.

In a study of Friction Stir Welding (FSW) of Inconel 718, the 3D strain field at the boundary of the stir zone needs to be determined. This determination will aid in a better understanding of the evolution of the microstructure of the material as a result of applying the FSW process to the material. The 3D strain field is needed in order to determine the localized work hardening of the material as well as validating large deformation constitutive models when the material is deformed. Determination of the 3D strain field is a challenge since there are no known ways to measure 3D strains from the observable plane or from two dimensional cross-sections.

Jata [5] described a method to estimate the strain rate at the boundary of the stir zone of FSW Al-Li alloys. In his study, the one dimensional shear deformation at the

boundary of the stir zone in a transverse section of FSW Al-Li alloy was measured. Rather than determining the 3D strain field, Jata [5] assumed one dimensional shear strain. However, since the strain field is a matrix and not a scalar [4], the single dimensional shear strain estimation probably cannot possibly interpret the whole strain field very well. Jata [5] used the estimated strain rate of the Al-Li alloy to calculate "z" parameter, and then correlated the "z" parameter with the hot working experimental results from other researchers. Although Jata stated that the estimated strain rate using his method matched other's experimental data, it is still not a convincing approach. Therefore, developing a new method to determine 3D strain fields is desired so the material properties and microstructure evolution of the material at the boundary of the stir zone during FSW can be studied.

When study the microstructure and properties of materials, Orientation Imaging Microscopy (OIM) or other tools can be used to characterize the 2D microstructure in three orthogonal planes. Analyzing or quantifying the deformation of the microstructure in each orthogonal plane may help us determine the 3D strain field in the material.

This 3D strain estimated method can be applied to materials in general which allows measurement of the 2D microstructure in the three orthogonal planes. One of the applications of this current model is in FSW materials. Determining the 3D strain field by this method allows estimation of the strain rate of the FSW material. The strain, strain rate, and thermal cycles are key to predicting the microstructure evolution in the material. These findings will enable a prediction of material properties to be made for the material.

A 3D deformation model was created in this study and the numerical solutions proved to work well. A case study of FSW Inconel 718 is presented as a reference. The

3D strain and strain rate were estimated at the boundary of the stir zone, and the strain was found to be reasonable when compared with the deformation maps [35 and 36]. The strain and strain rate were then used to develop a better understanding of the microstructure evolution and predict material properties of the material.

2.2 Model

In order to determine the 3D strain field, a mathematical model was created. The microstructure of FSW Inconel 718 measured in the three orthogonal planes was applied to this model. The strains were determined using this model, which is based on a linear displacement function. Since the 3D strain field depends on the displacement function [4], the determination of the displacement function from the deformed microstructure in three orthogonal planes could be a proper approach to estimate 3D strain.

2.2.1. Deform a Block of Material, Define a_{ij}

Imagine there is a standard box L_1 x L_2 x L_3 as shown in Fig 2-1. This box undergoes the deformation following a linear displacement function which is expressed as follows:

$$\begin{aligned} u_1 &= a_{11}x_1 + a_{12}x_2 + a_{13}x_3 \\ u_2 &= a_{21}x_1 + a_{22}x_2 + a_{23}x_3 \\ u_3 &= a_{31}x_1 + a_{32}x_2 + c_{33}x_3 \end{aligned} \qquad \textbf{(2-1)}$$

Or in a matrix form

$$U = D \cdot X \quad \text{, where } D = \begin{bmatrix} a_{11} & a_{12} & a_{13} \\ a_{21} & a_{22} & a_{23} \\ a_{31} & a_{32} & a_{33} \end{bmatrix} \text{ is displacement coefficient matrix} \quad \textbf{(2-2)}$$

Knowing the displacement function (Eq.2-1) is a necessary step to determine the strain field. The strain can be determined using [4]

$$\varepsilon_{ij} = \frac{1}{2} \cdot (U_{i,j} + U_{j,i}) \quad \textbf{(2-3)}$$

The strain is determined from the assumed linear displacement function and can be expressed as follows:

$$\varepsilon_{3D} = \begin{bmatrix} a_{11} & \frac{1}{2} \cdot a_{21} + \frac{1}{2} \cdot a_{12} & \frac{1}{2} \cdot a_{31} + \frac{1}{2} \cdot a_{13} \\ \frac{1}{2} \cdot a_{21} + \frac{1}{2} \cdot a_{12} & a_{22} & \frac{1}{2} \cdot a_{32} + \frac{1}{2} \cdot a_{23} \\ \frac{1}{2} \cdot a_{31} + \frac{1}{2} \cdot a_{13} & \frac{1}{2} \cdot a_{32} + \frac{1}{2} \cdot a_{23} & a_{33} \end{bmatrix} \quad \textbf{(2-4)}$$

As shown in Eq.2-4, the 3D strain is a function of the displacement coefficients. In order to reach the goal in determining the 3D strain, the first step is to determine the displacement coefficients. The following paragraphs detail the mathematical model used

to discover the relationship between the grain shape in three orthogonal planes and the displacement coefficients.

The effective strain [4] can be calculated using

$$\bar{\varepsilon} = \sqrt{\frac{2}{3}} * \sqrt{\varepsilon_{ij} \cdot \varepsilon_{ij}} \qquad \textbf{(2-5)}$$

Begin by creating an un-deformed box as shown in Fig 2-1 with eight original vertices (*A*, *E*, *C*, *D*, *E*, *F*, *G*, and *H*) and with the original edges of the box being parallel to the coordinate axes. The coordinates of the eight original vertices are A(0,0,0), B(L_1,0,0), C(L_1,L_2,0), D(0,L_2,0), E(0,0,L_3), F(L_1,0,L_3), G(L_1,L_2,L_3), and H(0,L_2,L_3).

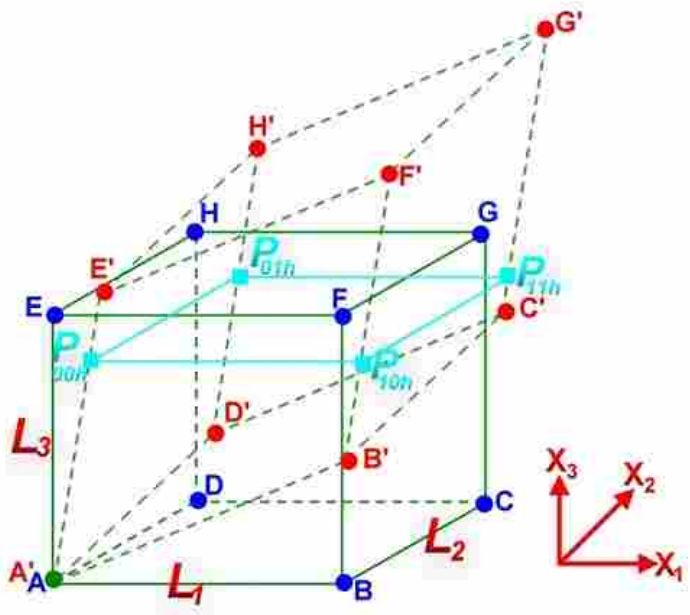

Figure 2-1 3D Undeformed and deformed box

This rectangular box (L_1 x L_2 x L_3) then undergoes deformation following the linear displacement function shown in Eq. 2-2. Eight new vertices (A', B', C', D', E', F', G', and H') are generated.

The coordinates of eight new vertices (A', B', C', D', E', F', G', and H') can be determined using the displacement function displayed in Eq. 2-6.

$$X_{new} = D \cdot X_{original} + X_{original} \quad \textbf{(2-6)}$$

The eight new vertices coordinates of the deformed box were calculated in accordance with the above equation (Eq.2-6) and expressed as

$$\begin{aligned}
P_G' &= (a_{11}l_1 + a_{12}l_2 + a_{13}l_3 + l_1 \quad a_{21}l_1 + a_{22}l_2 + a_{23}l_3 + l_2 \quad a_{31}l_1 + a_{32}l_2 + a_{33}l_3 + l_3) \\
P_H' &= (a_{21}l_2 + a_{31}l_3 \quad a_{21}l_2 + a_{32}l_3 + l_2 \quad a_{32}l_2 + a_{33}l_3 + l_3) \\
P_F' &= (a_{11}l_1 + a_{31}l_3 + l_1 \quad a_{21}l_1 + a_{23}l_3 \quad a_{31}l_1 + a_{33}l_3 + l_3) \\
P_E' &= (a_{31}l_3 \quad a_{32}l_3 \quad a_{33}l_3 + l_3) \\
P_C' &= (a_{11}l_1 + a_{12}l_2 + l_1 \quad a_{21}l_1 + a_{22}l_2 + l_2 \quad a_{31}l_1 + a_{32}l_2) \\
P_D' &= (a_{12}l_2 \quad a_{22}l_2 + l_2 \quad a_{32}l_2) \\
P_B' &= (a_{12}l_1 + l_1 \quad a_{21}l_1 \quad a_{31}l_1) \\
P_A' &= (0 \quad 0 \quad 0)
\end{aligned} \quad \textbf{(2-7)}$$

2.2.2. Determine a 2D Cross Sections of Deformed Block

After deformation, three orthogonal planes (x_3=constant, x_2=constant, and x_1=constant) cut this deformed box. Three intersection areas and 12 intersection points (4 intersection points for each orthogonal plane) were generated. Fig 2-1 illustrates the case that a plane x_3=h (where h is between 0 and L_3) cut the deformed box. In this case,

four intersection points (P_{00h}, P_{10h}, P_{11h}, and P_{01h}) were obtained in the plan-view section. In a similar manner, the intersection points P_{0g0}, P_{1g0}, P_{1g1}, and P_{0g1} were obtained in the plane x_2=g (transverse section) and the intersection points P_{m00}, P_{m10}, P_{m11}, and P_{m01} were obtained in the plane x_1=m (longitudinal section).

The original shape plus the deformed shape of a region in each orthogonal plane needs to be quantified in order to determine the displacement coefficients. This process is described below.

2.2.3. Define Shape Parameters

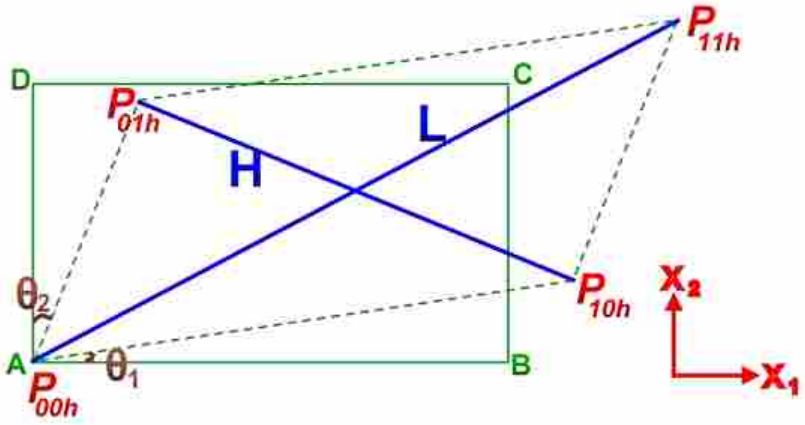

Figure 2-2 Plan-view section of the deformed box

The 2D shape parameters were introduced to describe the deformation in each orthogonal plane and must be defined before going through the calculation details. Fig 2-2 illustrates the deformation in the plan-view section. The rectangle $ABCD$ is located at the bottom section in Fig 2-1. The parallelogram $P_{00h}P_{10h}P_{11h}P_{01h}$ can be regarded as a

deformed rectangle. Four parameters can be used to determine the size, shape, and orientation of a parallelogram. For convenience, the parameters L, H, θ_1 and θ_2 which are illustrated in Fig 2-2 were selected in this study. The parameters L and H represent the major and minor diagonals of the parallelogram $P_{00h}P_{10h}P_{11h}P_{01h}$. θ_1 and θ_2 are the angles between one side of the deformed rectangle with the x and y directions. The parameters L, H, θ_1 and θ_2 are used to represent the shape of the deformed planes and correlate with the displacement functions. Therefore, L, H, θ_1 and θ_2 are defined as the shape parameters. The main purpose for introducing the shape parameters is to quantify the deformed shape in the three orthogonal planes in the form of the displacement coefficients a_{ij}. Thus, the relationship between the deformed shapes in three orthogonal planes with the displacement coefficients a_{ij} can be discovered.

2.2.4. Shape Parameters as Function of Displacement Coefficients

The shape parameters (L, H, θ_1 and θ_2) which result from a known deformation are determined by measuring microstructures. The following paragraphs detail how to determine the shape parameters of a cross-section view by determining the intersection points of the deformed box for each orthogonal plane, given the displacement coefficients.

The x_3=h plane is taken as an example to demonstrate the determination of the intersection points. As shown in Fig 2-1, the four intersection points in plan-view section are P_{00h}, P_{10h}, P_{11h}, and P_{01h}, which are on the lines $A'E'$, $B'F'$, $C'G'$, and $D'H'$ respectively. The line $B'F'$ was selected as an example for the coordinate of the intersection point P_{10h} as shown in Fig 2-3.

Let a plane x_3=h cut the line $B'F'$ as shown in Fig 2-3, and the intersection point P_{10h} is generated. The x_3 coordinate (x_3=h is known), the x_1 and x_2 coordinates of the intersection point P_{10h}must be determined. Geometrical calculation can be utilized to determine the coordinates of the intersection points. For convenience, the lines and points shown in Fig 2-3 are defined. The line $B'O$ is the projection of the line $B'F'$ in the plane x_3=0 and the point O is projection of point F' in the plane x_3=0; the lines OB'' and $P_{10h}'P_{10h}''$ are parallel to the x_2 direction; the lines $B'B''$ and $P_{10h}P_{10h}''$ are parallel to the x_1 direction; and the lines $B'O$ and $P_{10h}P_{10h}'$ are parallel to each other. It is noticed that $\Delta F'P_{10h}P_{10h}'$ is similar to $\Delta F'B'O$; $\Delta F'P_{10h}'P_{10h}''$ is similar to $\Delta F'OB''$; and $\Delta F'P_{10h}P_{10h}''$ is similar to $\Delta F'B'B''$. Moreover, $\Delta F'OB''$ is parallel to x_2-x_3 plane, and $\Delta F'B'B''$ is parallel to x_1-x_3 plane.

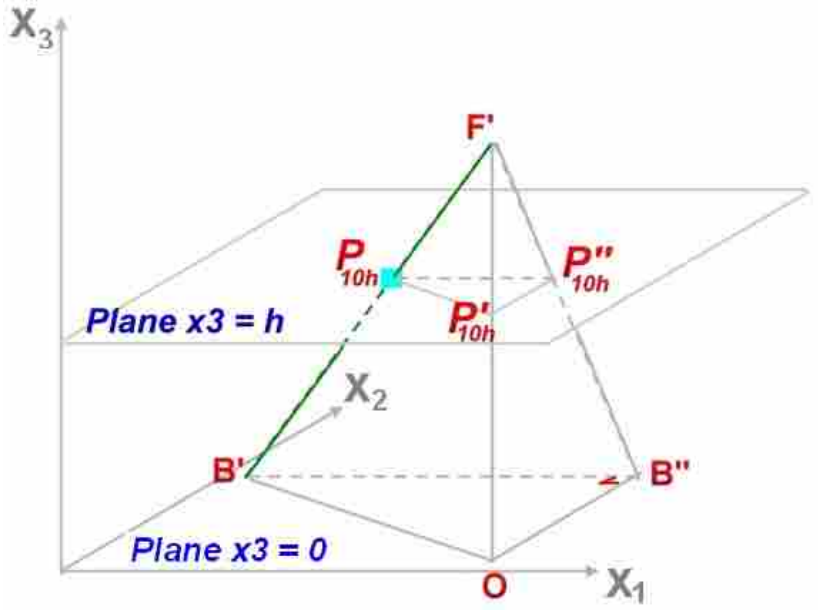

Figure 2-3 Determination of the intersection points in a 2D plane

There is a relationship among the line segments of similar triangles. (Note that the upper bar represents the length of a segment. For example, $\overline{F'O}$ stands for the length between the points F' and C.)

$$\frac{\overline{F'P_{10h}'}}{\overline{F'O}} = \frac{\overline{P_{10h}P_{10h}''}}{\overline{B'B''}} = \frac{\overline{P_{10h}'P_{10h}''}}{\overline{OB''}} \tag{2-8}$$

The lengths of segments $\overline{F'O}$, $\overline{F'P_{10h}'}$, $\overline{OB''}$, and $\overline{B'B''}$ can be calculated as follows:

$$\begin{aligned}
\overline{F'O} &= x_3(F') - x_3(B') \\
\overline{F'P_{10h}'} &= x_3(F') - h \\
\overline{OB''} &= x_2(F') - x_2(B') \\
\overline{B'B''} &= x_1(F') - x_1(B')
\end{aligned} \tag{2-9}$$

and

$$\frac{x_3(F') - h}{x_3(F') - x_3(B')} = \frac{\overline{P_{10h}P_{10h}''}}{x_1(F') - x_1(B')} \quad , \; x_1(P_{10k}) = x_1(F') - \overline{P_{10h}P_{10h}''} \tag{2-10}$$

$$\frac{x_3(F') - h}{x_3(F') - x_3(B')} = \frac{\overline{P_{10h}'P_{10h}''}}{x_2(F') - x_2(B')} \quad , \; x_2(P_{10k}) = x_2(F') - \overline{P_{10h}'P_{10h}''} \tag{2-11}$$

where

$$\overline{P_{10h}P_{10h}''} = \frac{(x_3(F') - h) \cdot (x_1(F') - x_1(B'))}{x_3(F') - x_3(B')} \tag{2-12}$$

and

$$\overline{P_{10h}{}'P_{10h}{}''} = \frac{(x_3(F')-h)\cdot(x_2(F')-x_2(B'))}{x_3(F')-x_3(B')} \qquad \textbf{(2-13)}$$

Note that the plane $F'OB''$ is parallel to the plane $x_1 = 0$. Therefore, the x_1 coordinate of the points in the plane $F'OB''$ are identical and the intersection points P_{10h} can be determined.

$$P_{10h}:\left(x_1(F')-\frac{(x_3(F')-h)\cdot(x_1(F')-x_1(B'))}{x_3(F')-x_3(B')} \quad x_2(F')-\frac{(x_3(F')-h)\cdot(x_2(F')-x_2(B'))}{x_3(F')-x_3(B')} \quad h\right) \qquad \textbf{(2-14)}$$

By the same means, the remaining 3 intersection points in the plane x_3=h were determined. The four intersection points in the plane x_3=h can be expressed by the displacement coefficients shown in Eq.2-15.

$$P_{11h}=\left[a_{11}\cdot l_1+a_{12}\cdot l_2+a_{13}\cdot l_3+l_1-\left(a_{31}\cdot l_1+a_{33}\cdot l_2+a_{33}\cdot l_3+l_3-h\right)\cdot a_{13}\cdot\frac{l_3}{\left(a_{33}\cdot l_3+l_3\right)} \quad a_{21}\cdot l_1+a_{22}\cdot l_2+a_{23}\cdot l_3+l_2-\left(a_{31}\cdot l_1+a_{32}\cdot l_2+a_{33}\cdot l_3+l_3-h\right)\cdot a_{23}\cdot\frac{l_3}{\left(a_{33}\cdot l_3+l_3\right)} \quad h\right]$$

$$P_{10h}=\left[a_{11}\cdot l_1+a_{13}\cdot l_3+l_1-\left(a_{31}\cdot l_1+a_{32}\cdot l_3+l_3-h\right)\cdot a_{13}\cdot\frac{l_3}{\left(a_{33}\cdot l_3+l_3\right)} \quad a_{21}\cdot l_1+a_{23}\cdot l_3-\left(a_{31}\cdot l_1+a_{33}\cdot l_3+l_3-h\right)\cdot a_{23}\cdot\frac{l_3}{\left(a_{33}\cdot l_3+l_3\right)} \quad h\right]$$

$$P_{01h}=\left[a_{12}\cdot l_2+a_{13}\cdot l_3-\left(a_{33}\cdot l_2+a_{33}\cdot l_3+l_3-h\right)\cdot a_{13}\cdot\frac{l_3}{\left(a_{33}\cdot l_3+l_3\right)} \quad a_{22}\cdot l_2+a_{23}\cdot l_3+l_2-\left(a_{32}\cdot l_2+a_{33}\cdot l_3+l_3-h\right)\cdot a_{23}\cdot\frac{l_3}{\left(a_{33}\cdot l_3+l_3\right)} \quad h\right]$$

$$P_{00h}=\left[a_{13}\cdot l_3-\left(a_{33}\cdot l_3+l_3-h\right)\cdot a_{13}\cdot\frac{l_3}{\left(a_{33}\cdot l_3+l_3\right)} \quad a_{23}\cdot l_3-\left(a_{33}\cdot l_3+l_3-h\right)\cdot a_{23}\cdot\frac{l_3}{\left(a_{33}\cdot l_3+l_3\right)} \quad h\right] \qquad \textbf{(2-15)}$$

In the similar manner, the eight intersection points in the planes x_2=g and x_1=m were also determined. The eight intersections points in the plane x_2=g, and x_1=m are expressed in Eq.2-16, and Eq.2-17 respectively.

$$P_{1g1} = \left[a_{11}\cdot l_1 + a_{12}\cdot l_2 + a_{13}\cdot l_3 + l_1 - \left(a_{21}\cdot l_1 + a_{22}\cdot l_2 + a_{23}\cdot l_3 + l_2 - g\right)\cdot a_{12}\cdot \frac{l_2}{\left(a_{22}\cdot l_2 + l_2\right)} \quad g \quad a_{31}\cdot l_1 + a_{32}\cdot l_2 + a_{33}\cdot l_3 + l_3 - \left(a_{21}\cdot l_1 + a_{22}\cdot l_2 + a_{23}\cdot l_3 + l_2 - g\right)\cdot a_{32}\cdot \frac{l_2}{\left(a_{22}\cdot l_2 + l_2\right)} \right]$$

$$P_{1g0} = \left[a_{11}\cdot l_1 + a_{12}\cdot l_2 + l_1 - \left(a_{21}\cdot l_1 + a_{22}\cdot l_2 + l_2 - g\right)\cdot a_{12}\cdot \frac{l_2}{\left(a_{22}\cdot l_2 + l_2\right)} \quad g \quad a_{31}\cdot l_1 + a_{32}\cdot l_2 - \left(a_{21}\cdot l_1 + a_{22}\cdot l_2 + l_2 - g\right)\cdot a_{32}\cdot \frac{l_2}{\left(a_{22}\cdot l_2 + l_2\right)} \right]$$

$$P_{0g1} = \left[a_{12}\cdot l_2 + a_{13}\cdot l_3 - \left(a_{22}\cdot l_2 + a_{23}\cdot l_3 + l_2 - g\right)\cdot a_{12}\cdot \frac{l_2}{\left(a_{22}\cdot l_2 + l_2\right)} \quad g \quad a_{32}\cdot l_2 + a_{33}\cdot l_3 + l_3 - \left(a_{22}\cdot l_2 + a_{23}\cdot l_3 + l_2 - g\right)\cdot a_{32}\cdot \frac{l_2}{\left(a_{22}\cdot l_2 + l_2\right)} \right]$$

$$P_{0g0} = \left[a_{12}\cdot l_2 - \left(a_{22}\cdot l_2 + l_2 - g\right)\cdot a_{12}\cdot \frac{l_2}{\left(a_{22}\cdot l_2 + l_2\right)} \quad g \quad a_{32}\cdot l_2 - \left(a_{22}\cdot l_2 + l_2 - g\right)\cdot a_{32}\cdot \frac{l_2}{\left(a_{22}\cdot l_2 + l_2\right)} \right]$$

(2-16)

$$P_{m11} = \left[m \quad a_{21}\cdot l_1 + a_{22}\cdot l_2 + a_{23}\cdot l_3 + l_2 - \left(a_{11}\cdot l_1 + a_{12}\cdot l_2 + a_{13}\cdot l_3 + l_1 - m\right)\cdot a_{21}\cdot \frac{l_1}{\left(a_{11}\cdot l_1 + l_1\right)} \quad a_{31}\cdot l_1 + a_{33}\cdot l_2 + a_{33}\cdot l_3 + l_3 - \left(a_{11}\cdot l_1 + a_{12}\cdot l_2 + a_{13}\cdot l_3 + l_1 - m\right)\cdot a_{31}\cdot \frac{l_1}{\left(a_{11}\cdot l_1 + l_1\right)} \right]$$

$$P_{m10} = \left[m \quad a_{21}\cdot l_1 + a_{22}\cdot l_2 + l_2 - \left(a_{11}\cdot l_1 + a_{12}\cdot l_2 + l_1 - m\right)\cdot a_{21}\cdot \frac{l_1}{\left(a_{11}\cdot l_1 + l_1\right)} \quad a_{31}\cdot l_1 + a_{32}\cdot l_2 - \left(a_{11}\cdot l_1 + a_{12}\cdot l_2 + l_1 - m\right)\cdot a_{31}\cdot \frac{l_1}{\left(a_{11}\cdot l_1 + l_1\right)} \right]$$

$$P_{m01} = \left[m \quad a_{21}\cdot l_1 + a_{23}\cdot l_3 - \left(a_{11}\cdot l_1 + a_{13}\cdot l_3 + l_1 - m\right)\cdot a_{21}\cdot \frac{l_1}{\left(a_{11}\cdot l_1 + l_1\right)} \quad a_{31}\cdot l_1 + a_{33}\cdot l_3 + l_3 - \left(a_{11}\cdot l_1 + a_{13}\cdot l_3 + l_1 - m\right)\cdot a_{31}\cdot \frac{l_1}{\left(a_{11}\cdot l_1 + l_1\right)} \right]$$

$$P_{m00} = \left[m \quad a_{21}\cdot l_1 - \left(a_{11}\cdot l_1 + l_1 - m\right)\cdot a_{21}\cdot \frac{l_1}{\left(a_{11}\cdot l_1 + l_1\right)} \quad a_{31}\cdot l_1 - \left(a_{11}\cdot l_1 + l_1 - m\right)\cdot a_{31}\cdot \frac{l_1}{\left(a_{11}\cdot l_1 + l_1\right)} \right]$$

(2-17)

Knowing the intersection points in the three orthogonal planes (Eq.2-15 to Eq.2-17) allows to calculate the shape of the intersection areas. The slopes of the four side lines of the deformed rectangle are calculated and compared to each other. The plan-view section of Fig 2-2 was taken as an example. The calculation showed that the slope of the line $P_{00h}P_{10h}$ was identical to the slope of the line $P_{01h}P_{11h}$ and the slope of the line $P_{00h}P_{10h}$ was equal the slope of the line $P_{10h}P_{11h}$, making this is a parallelogram. In a similar manner, the intersection areas in the x_1-x_3 plane and the x_2-x_3 plane were proved to be parallelograms.

As displayed in Eq.2-15, 2-16, and 2-17, the coordinates of these intersection points are expressed in the form of displacement coefficients a_{ij}. Therefore, the shape parameters L, H, L/H, θ_1 and θ_2 can also be determined as a function of the displacement coefficients for each orthogonal plane. Subsequently, a relationship between the strain in the plane sections and the displacement coefficients can be discovered. Quantifying the

shape parameters according to the coordinates obtained for the intersection points is a significant step toward solving the displacement coefficients and the 3D strain.

The shape parameters such as L, H, θ_1 and θ_2 can be calculated from the coordinates of the 12 intersection points using the routine trigonometric operation. As shown in Fig 2-2, the angles θ_1 and θ_2 in the x_1-x_2 plane can be calculated as follows.

$$\theta_{1\_PLV} = \tan^{-1}\left(\frac{x_2(P_{10h}) - x_2(P_{00h})}{x_1(P_{10h}) - x_1(P_{00h})}\right) \quad \textbf{(2-18)}$$

$$\theta_{2\_PLV} = \tan^{-1}\left(\frac{x_2(P_{01h}) - x_2(P_{00h})}{x_1(P_{01h}) - x_1(P_{00h})}\right) \quad \textbf{(2-19)}$$

Where $x_i(P_{jkh})$ represents the x_i coordinate of point P_{jkh}.

The two angles θ_1 and θ_2 as the functions of the displacement coefficients were then determined in the x_1-x_2 plane:

$$\begin{aligned} \tan(\theta_{1\_PLV}) &= \frac{(a_{21}a_{33} + a_{21} - a_{23}a_{31})}{(a_{11}a_{33} + a_{11} + a_{33} + 1 - a_{13}a_{31})} \\ \tan(\theta_{2\_PLV}) &= \frac{(a_{22}a_{33} + a_{22} + a_{33} + 1 - a_{23}a_{32})}{(a_{12}a_{33} + a_{21} - a_{13}a_{32})} \end{aligned} \quad \textbf{(2-20)}$$

In a similar manner, the angles in transverse and longitudinal sections such as $\theta_{1\_TS}, \theta_{2\_TS}$, θ_{1_LS}, and θ_{2_LS} were determined. The two angles as the function of the

displacement coefficients in the x_1-x_3 and the x_2-x_3 planes are expressed in the Eq.2-21 and Eq.2-22.

In the x_1-x_3 plane:

$$\tan(\theta_{1\_TS}) = \frac{(-a_{31}a_{22} - a_{31} + a_{32}a_{21})}{(-a_{11}a_{22} - a_{11} - a_{22} - 1 + a_{12}a_{21})}$$
$$\tan(\theta_{2\_TS}) = \frac{(a_{22}a_{33} + a_{22} + a_{33} + 1 - a_{23}a_{32})}{(a_{13}a_{22} + a_{13} - a_{12}a_{23})} \quad \textbf{(2-21)}$$

In the x_2-x_3 plane:

$$\tan(\theta_{1\_LS}) = \frac{-(a_{32}a_{11} + a_{32} - a_{31}a_{12})}{(-a_{11}a_{22} - a_{11} - a_{22} - 1 + a_{12}a_{21})}$$
$$\tan(\theta_{2\_LS}) = \frac{-(a_{11}a_{31} + a_{11} + a_{33} + 1 - a_{13}a_{31})}{(-a_{23}a_{11} - a_{23} + a_{21}a_{13})} \quad \textbf{(2-22)}$$

As shown in Fig 2-2, the major diagonal L_{PLV} is the length of $\overline{P_{00h}P_{11h}}$, and the minor diagonal H_{PLV} is the length of $\overline{P_{10h}P_{01h}}$. The calculation details of the major and minor diagonals are expressed as follows:

$$L_{PLV}^{\ 2} = (x_1(P_{11h}) - x_1(P_{00h}))^2 + (x_2(P_{11h}) - x_2(P_{00h}))^2 \quad \textbf{(2-23)}$$

$$H_{PLV}^{\ 2} = (x_1(P_{01h}) - x_1(P_{10h}))^2 + (x_2(P_{01h}) - x_2(P_{10h}))^2 \quad \textbf{(2-24)}$$

The major and minor diagonals in the remaining two plane sections such as L_{TS}, $H_{TS,}$ L_{LS}, and H_{LS} were determined in the same manner.

The major and minor diagonals in the three orthogonal planes are calculated and shown as follows:

The diagonal line for x_1-x_2 plane

$$L_{PLV}^2 = \left[\frac{\left(a_1 \cdot l_1 \cdot c_3 + a_1 \cdot l_1 + b_1 \cdot l_2 \cdot c_3 + b_1 \cdot l_2 + l_1 \cdot c_3 + l_1 - c_1 \cdot a_3 \cdot l_1 - c_1 \cdot b_3 \cdot l_2\right)}{\left(c_3 + 1\right)}\right]^2 + \left[\frac{\left(a_2 \cdot l_1 \cdot c_3 + a_2 \cdot l_1 + b_2 \cdot l_2 \cdot c_3 + b_2 \cdot l_2 + l_2 \cdot c_3 + l_2 - c_2 \cdot a_3 \cdot l_1 - c_2 \cdot b_3 \cdot l_2\right)}{\left(c_3 + 1\right)}\right]^2$$

$$H_{PLV}^2 = \left[\frac{-\left(a_1 \cdot l_1 \cdot c_3 + a_1 \cdot l_1 + l_1 \cdot c_3 + l_1 - c_1 \cdot a_3 \cdot l_1 - b_1 \cdot l_2 \cdot c_3 - b_1 \cdot l_2 + c_1 \cdot b_3 \cdot l_2\right)}{\left(c_3 + 1\right)}\right]^2 + \left[\frac{-\left(a_2 \cdot l_1 \cdot c_3 + a_2 \cdot l_1 - c_2 \cdot a_3 \cdot l_1 - b_2 \cdot l_2 \cdot c_3 - b_2 \cdot l_2 - l_2 \cdot c_3 - l_2 + c_2 \cdot b_3 \cdot l_2\right)}{\left(c_3 + 1\right)}\right]^2$$

(2-25)

The diagonal line for x_1-x_3 plane

$$L_{TS}^2 = \left[\frac{-\left(-a_1 \cdot l_1 \cdot b_2 - a_1 \cdot l_1 - c_1 \cdot l_3 \cdot b_2 - c_1 \cdot l_3 - l_1 \cdot b_2 - l_1 + b_1 \cdot a_2 \cdot l_1 + b_1 \cdot c_2 \cdot l_3\right)}{\left(b_2 + 1\right)}\right]^2 + \left[\frac{-\left(-a_3 \cdot l_1 \cdot b_2 - a_3 \cdot l_1 - c_3 \cdot l_3 \cdot b_2 - c_3 \cdot l_3 - l_3 \cdot b_2 - l_3 + b_3 \cdot a_2 \cdot l_1 + b_3 \cdot c_2 \cdot l_3\right)}{\left(b_2 + 1\right)}\right]^2$$

$$H_{TS}^2 = \left[\frac{\left(-a_1 \cdot l_1 \cdot b_2 - a_1 \cdot l_1 - l_1 \cdot b_2 - l_1 + b_1 \cdot a_2 \cdot l_1 + c_1 \cdot l_3 \cdot b_2 + c_1 \cdot l_3 - b_1 \cdot c_2 \cdot l_3\right)}{\left(b_2 + 1\right)}\right]^2 + \left[\frac{\left(-a_3 \cdot l_1 \cdot b_2 - a_3 \cdot l_1 + b_3 \cdot a_2 \cdot l_1 + c_3 \cdot l_3 \cdot b_2 + c_3 \cdot l_3 + l_3 \cdot b_2 + l_3 - b_3 \cdot c_2 \cdot l_3\right)}{\left(b_2 + 1\right)}\right]^2$$

(2-26)

The diagonal line for x_2-x_3 plane

$$L_{LS}^2 = \left[\frac{-\left(-b_2 \cdot l_2 \cdot a_1 - b_2 \cdot l_2 - c_2 \cdot l_3 \cdot a_1 - c_2 \cdot l_3 - l_2 \cdot a_1 - l_2 + a_2 \cdot b_1 \cdot l_2 + a_2 \cdot c_1 \cdot l_3\right)}{\left(a_1 + 1\right)}\right]^2 + \left[\frac{\left(b_3 \cdot l_2 \cdot a_1 + b_3 \cdot l_2 + c_3 \cdot l_3 \cdot a_1 + c_3 \cdot l_3 + l_3 \cdot a_1 + l_3 - a_3 \cdot b_1 \cdot l_2 - a_3 \cdot c_1 \cdot l_3\right)}{\left(a_1 + 1\right)}\right]^2$$

$$H_{LS}^2 = \left[\frac{-\left(-c_2 \cdot l_3 \cdot a_1 - c_2 \cdot l_3 + a_2 \cdot c_1 \cdot l_3 + b_2 \cdot l_2 \cdot a_1 + b_2 \cdot l_2 + l_2 \cdot a_1 + l_2 - a_2 \cdot b_1 \cdot l_2\right)}{\left(a_1 + 1\right)}\right]^2 + \left[\frac{\left(c_3 \cdot l_3 \cdot a_1 + c_3 \cdot l_3 + l_3 \cdot a_1 + l_3 - a_3 \cdot c_1 \cdot l_3 - b_3 \cdot l_2 \cdot a_1 - b_3 \cdot l_2 + a_3 \cdot b_1 \cdot l_2\right)}{\left(a_1 + 1\right)}\right]^2$$

(2-27)

Equations (2-22) to (2-27) describe the shape parameters in terms of displacement coefficients. The next section describes how the displacement coefficients can be determined from the shape parameters.

2.3 Numerical Solution

In order to determine strain from microstructure, the displacement coefficients from the known shape parameters must be determined. Attempts have been made to invert the twelve shape parameter equations (Eq.2-20 to Eq.2-27). However, these equations are non-linear and complicated so there are no ways to directly invert the equations. Numerical methods were utilized to determine the displacement coefficients as a typical inverse problem. It is possible that inverse solutions cannot be found numerically. Therefore, before carrying out the numerical analysis, it is required to check whether or not the inverse solution can be found.

To determine whether or not a solution can be found, a number of test cases were tried. For each test case, displacement coefficients were defined. The shape parameters were calculated, and then the numerical procedure was applied to the shape parameters to see if the known displacement coefficients could be obtained. The consequence paragraph details the procedure.

A set of displacement coefficients were assumed, and substituted into the shape parameter functions which are from Eq.2-20 through Eq.2-27 (Eq.2-20 to Eq.2-27). Thus, the shape parameters L/H, L, θ_1 and θ_2 in the three orthogonal planes were obtained. This is the first step of the checking procedure. Then, the second step where the obtained shape parameters are substituted to the shape parameter functions (from Eq.2-20 to Eq.2-27) was performed again. A total of 12 equations were generated to solve the 9 unknown displacement coefficients. Numerical optimization was carried out to determine the displacement coefficients and MathCAD was utilized to perform the numerical optimization solution. The optimization algorithm, in MathCAD, that was used was the

Gauss-Newton method. In this step, the nine displacement coefficients were determined. Finally, the solved displacement coefficients were compared with the assumed displacement coefficients. In this case, the solved and assumed displacement coefficients are identical, which suggests that this problem is solvable and this method to estimate the displacement coefficients can be used.

All deformation fields conforming to plastic deformation of real solids must satisfy the condition $trace(a_{ij}) = 0$. For deformation fields that don't follow the condition $trace(a_{ij}) = 0$, expansion or contraction must occur. In this study, the case without expansion or contraction draws more concerns. Therefore, the constraint of $trace(a_{ij}) = 0$ was taken into consideration, when three sets of displacement coefficients were selected. Otherwise, the three sets of displacement coefficients were selected arbitrarily. Three sets of different side lengths of the box L_1, L_2 and L_3 were selected as well, which are listed in Table 2-1.

Table 2-1 The assumed displacement coefficient and original size of rectangle

	a_{11}	a_{21}	a_{31}	a_{12}	a_{22}	a_{32}	a_{13}	a_{23}	a_{33}	L1	L2	L3
Case1	2	-1	1	-3	1	3	-1	-3	-3	2	1	2
Case2	-3	1	3	1	1	-2	1	-2	2	1	2	2
Case3	1	3	3	2	-3	2	0	-3	2	2	2	1

After substituting the assumed displacement coefficients as shown in Table 2-1 into the shape parameter equations (Eq.2-20 to Eq.2-27), the shape parameters were obtained. The obtained shape parameters are shown in Table 2-2.

The values of the shape parameters listed in Table2-2 were substituted into the shape parameter functions (Eq.2-20 to Eq.2-27), which are in the form of the displacement coefficients a_{ij}. There are a total of 12 equations to solve 9 unknowns for each case.

Table 2-2 The calculated shape parameters

Planes	Shape Parameters	Case1	Case2	Case3
PLV	Tan(θ*1)*	-0.6	-1	2.625
	Tan(θ2)	2	0.4	-0.25
	L(PLV)^2	85.78	63.22	136
	(L/H)^2	1.142	0.725	1.088
TS	Tan(θ*1)*	-0.33	-1.6	1.2
	Tan(θ2)	-1.2	0.5	-0.33
	L(TS)^2	464	101	212
	(L/H)^2	0.257	0.863	0.596
LS	Tan(θ*1)*	-2	-0.2	0.2
	Tan(θ2)	1.25	-3	-1.33
	L(LS)^2	124.89	72.5	170
	(L/H)^2	2.051	0.602	2.073

Numerical optimization was performed to determine the displacement coefficients.

$$|err| = |measured\ shape\ parameters - calculated\ shape\ parameters\ by\ a_{ij}| \quad \textbf{(2-28)}$$

The absolute value of the error was minimized when carrying out the optimization. As a result, the displacement coefficients were determined. Matlab was utilized to perform the optimization using the Newton algorithm.

Table 2-3 Comparison of the solved and assumed displacement coefficients

	Case 1	Case 2	Case 3
Assumed Coeffs			
Initial 01			
Result01			
Initial 02			
Result02			
Initial 03			
Result03			

Three sets of the initial values were selected to perform optimization in the three cases. The displacement coefficients were solved when input the proper initial values. However, for some initial guessing of values, no convergence happened. In these cases,

the initial guessing values need to be changed and make several tries . Iterating in this fashion leads to a real solution. The calculation details are shown in Appendix A.

After obtaining the solution of the displacement coefficients, these values were compared with the originally assumed displacement coefficients . The results (Table 2 -3) show that the solutions are identical to the initially set values of the displacement coefficients. This suggests that this inverse problem can be solved and the displacement coefficients can be determined numerically from the shape parameters.

2.4 Microstructure

The inverse problem to determine the displacement coefficients from the assumed given shape parameters in the three orthogonal planes has been shown in the previous sections. This indicates that the approach works mathematically. The remaining step is to apply this 3D deformation model to the microstructure of FSW Inconel 718 at the stir zone boundary.

This was accomplished by using OIM to characterize the microstructure in three orthogonal planes and at the boundary of the nugget zone on the AS. The following paragraphs detail this characterization process.

2.4.1. Measure the Deformed and Un-deformed Microstructure

In general, the TMAZ (Thermo Mechanical Affected Zone) is regarded as the transition area between the nugget zone and HAZ (Heat Affect Zone). The first challenge of this method is to find the boundary between the nugget and TMAZ. A macrograph of the FSW 718 (Fig 2-4) was utilized to identify the boundary between the nugget zone and

TMAZ on the advancing side (AS). The selected measurement boundary is at the position 2.96mm, 1.53mm, where the original point (0, 0) is located at the center of the weld as shown in Fig 2-4. Three adjacent samples were then cut in the transverse section. The selected position (2. 96mm, 1.53mm) can be found easily in three samples by means of Orientation Imaging Microscopy (OIM). The microstructure at this position was characterized by OIM, wh ich is illustrated in Fig 2-5. (Note that the bands marked by blue lines represent the TMAZ.) The grain size and grain shape are two major criteria used to determine the TMAZ. The average grain size in the nugget zone (close to the boundary) is approximately 2 -3μm. In the transition area, the grains become larger and larger, reaching between 9-12μm in the HAZ. The TMAZ is defined as the region where the grain size is between 3-9μm. One may also notice that the grains were aligned in this transition area, which can also help to identify TMAZ.

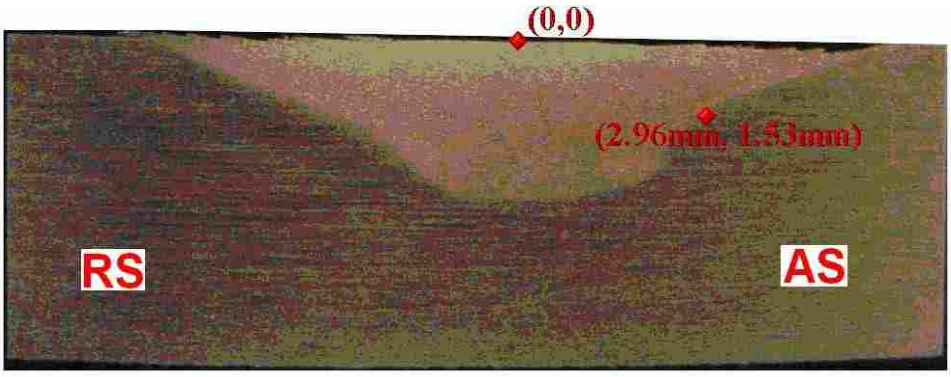

Figure 2-4 The selected boundary location

As shown in Fig 2-5, the mea sured position (2.96mm, 1.53mm) is located at the intersection point of the upper blue line (boundary between the nugget zone and TMAZ)

and the yellow line, where the yellow line's coordinate is x=2.96mm and the original point is the center point. The white points are located at the depth of 1.53mm.

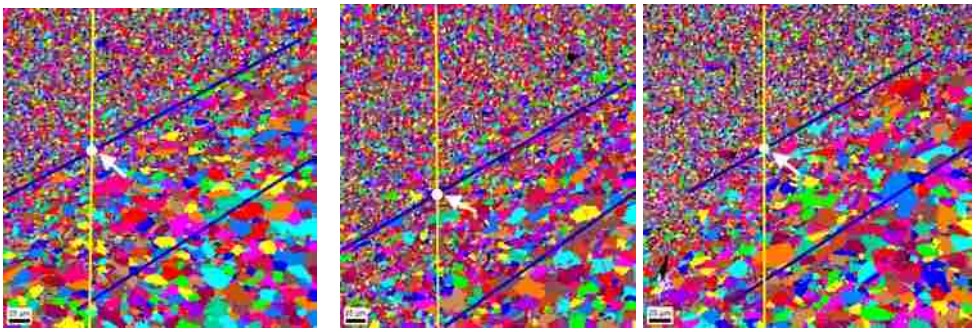

Figure 2-5 Microstructures at advancing side the boundary of nugget zone (three samples)

2.4.2. Determine Shape Parameters from Microstructure

The second challenge is in finding the tangent parallelogram for a given ellipse. The grains in TMAZ are regarded as ellipses. The tangent parallelogram is the deformed parallelogram for a given initial ellipse. The following figure (Fig 2-6) shows both deformed and undeformed grains with their tangent parallelogram.

The tangent parallelogram must be defined in order to measure the shape parameters (L, H, θ_1 and θ_2). Although there is an infinite number of parallelograms tangent to an ellipse, the correct parallelogram is needed. This parallelogram has the features that the four tangent points of the ellipse are the midpoints of the four sides of the tangent parallelogram. There is only one tangent parallelogram that has this feature. The procedure on how to define the tangent parallelogram of the ellipse is demonstrated in Appendix B.

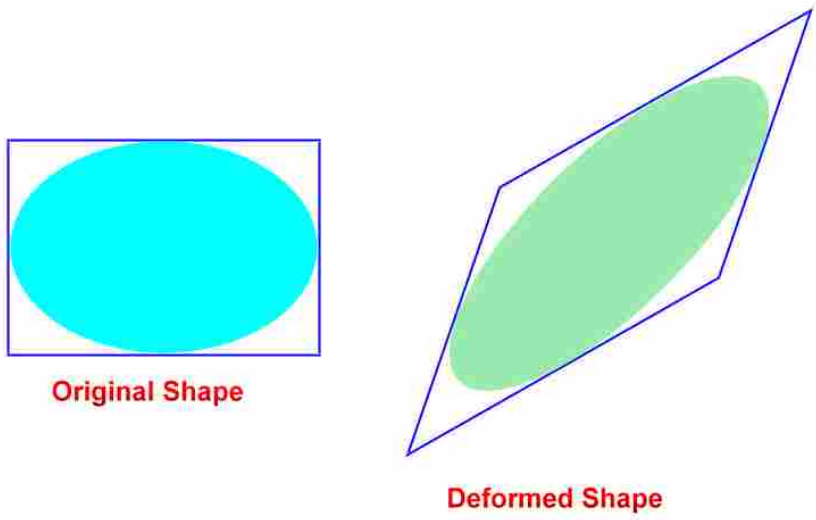

Figure 2-6 2D grain deformation

Fig 2-7 demonstrates how to define the tangent parallelogram for the undeformed and deformed grains.

Following this procedure, the tangent parallelograms of the measured grains can be determined and four parameters (L, H, θ_1 and θ_2) can be measured. Three samples for each orthogonal plane were measured and the results were averaged. Thus, a total of 12 shape parameters were obtained. The measurement results and average values in three orthogonal planes are displayed in the Table 2-4.

The shape parameters in three orthogonal planes were used in the equations from Eq.2-20 through Eq.2 -27. The displacement coefficients were first determined followed by the 3D strain.

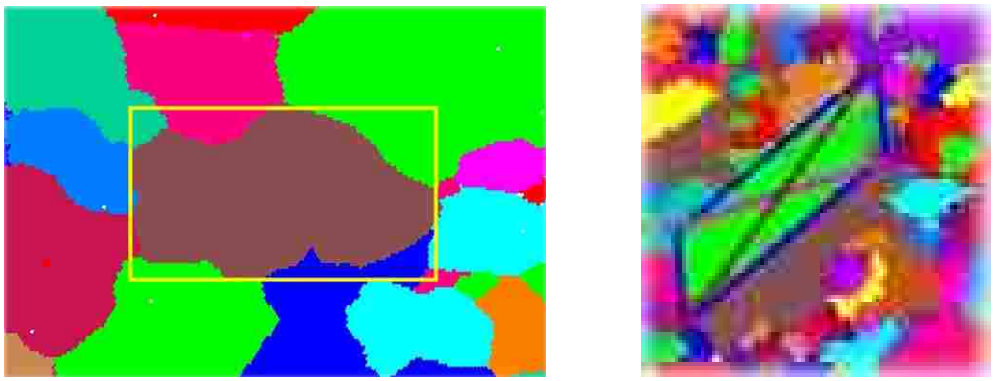

Figure 2-7 a) Grain of base metal and b)Grain at the boundary of nugget zone in AS

Measurements of the shape parameters L, H, θ_1 and θ_2 were obtained in three orthogonal planes and are contained in Table 2-4. Grain sizes and shapes changed significantly during the FSW process at the boundary of the stir zone as a result of recovery. Therefore, the aspect ratio of L/H was introduced. Note that the aspect ratio of L/H was used as one of the shape parameters because the size of the original box was unknown. The aspect ratio L/H is size independent. Either the parameter L or H needs to be included as a shape parameter to provide appropriate scaling for the deformed grains. In short, the system equations include the aspect ratio L/H, L or H, θ_1 and θ_2 in order to accomplish the calculation of the displacement coefficients.

The original grain size was 12-15 μm and the deformed grain size in the TMAZ was 4-7 μm as shown in Fig 2-7. In order to apply the 3D deformation model, an assumption that the original and deformed grains are in the same aspect ratio is made.

Table 2-4 Shape parameters

Planes	Parmtr	Sample 01	Sample 02	Sample 03	Avg.Value
	L	6.2	7.3	5.1	6.2
	H	3.2	3.9	2.7	3.27
	L/H	1.94	1.87	1.89	1.90
	Tan(Θ_1)	0.28	0.29	0.26	0.28
TS	**Tan(Θ_2)**	1.33	1.31	1.34	1.33
	L	7.58	7.42	7.51	7.50
	H	4.1	2.85	4.05	3.67
	L/H	1.85	2.60	1.85	2.10
	Tan(Θ_1)	0.32	0.32	0.31	0.32
PLV	**Tan(Θ_2)**	2.57	2.39	2.47	2.48
	L	6.92	6.59	6.58	6.70
	H	4.6	4.3	4.5	4.47
	L/H	1.50	1.53	1.46	1.50
	Tan(Θ_1)	0.20	0.21	0.21	0.21
LS	**Tan(Θ_2)**	4.73	4.77	4.60	4.70

As shown in Fig 2 -8, the tangent parallelogram of the original grain is $L_1 X L_2$ and has a large area. The area of the tangent parallelogram for the deformed grain is much smaller than the or iginal one. In order to make the two parallelograms in the same scaling, it was assumed that the area of the undeformed parallelogram is the same as the deformed parallelogram. Using the measured shape parameters of the deformed grain and the side lengths of the original parallelogram, the normalized side lengths , S_1 and S_2, (shown in Fig 2-8) can be determined. This normalized parallelogram was applied to the

3D deformation model to determine the 3D strain field at the boundary of the stir zone for FSW Inconel 718.

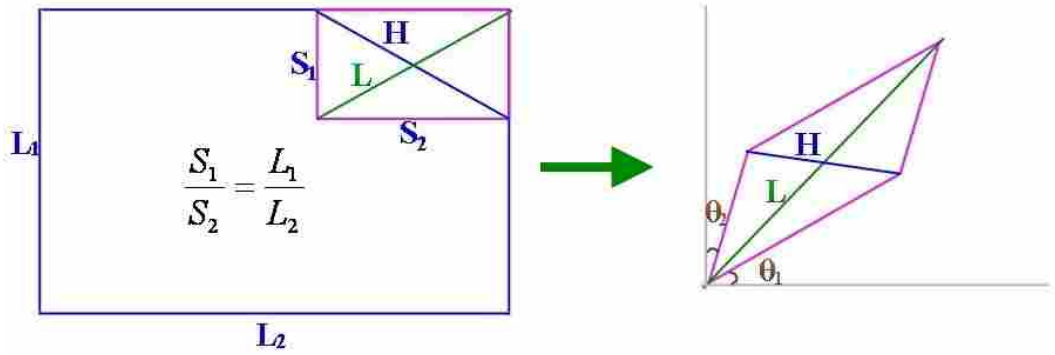

Figure 2-8 Normalizing the parallelogram of the original grain

2.4.3. Solve for a_{ij} and 3D Strain Field

By performing numerical optimization using Matlab and Mathcad as described in section 2.3 , the nine displacement coefficients were determined . The obtained displacement matrix is displayed in Eq. 2-29. (Note that this is a constraint volume deformation, $tr(a_{ij}) = 0$.) The calculation procedure is shown in Appendix C

$$D = \begin{bmatrix} .255 & .6573 & .9444 \\ .6756 & .4345 & .6952 \\ .8018 & .7105 & -.6895 \end{bmatrix} \quad \textbf{(2-29)}$$

The 3D strain field can be determined directly from Eq.2-4.

Then, the obtained displacement coefficients were substituted in the above equation, the strain field at the boundary of the nugget zone was obtained as follows:

$$\varepsilon_{Strain\_Nugget} = \begin{bmatrix} .255 & .736 & .973 \\ .736 & .4345 & .653 \\ .973 & .653 & .6895 \end{bmatrix} \quad \textbf{(2-30)}$$

2.4.4. Determine the Effective Strain Rate

Given the effective strain, Jata's method [5] to calculate the strain rate was used and the average effective strain rate was calculated as the quotient of the effective strain and the deformation time [5]. The deformation time was taken to be equal to the pin diameter (6.096 mm) divided by the transverse speed (6 in/min) [30]. The effective strain rate was then calculated as the quotient of the effective shear strain and the deformation time, making the estimated strain rate is $\dot{\varepsilon} = 12.6\ s^{-1}$.

The effective strain can be calculated using Eq.2-5 [4]. (Note this formula is used popularly for von Mises materials.) Metal is thought a typical von Mises material. By this means, the effective strain obtained is $\varepsilon_{eff} = 8.373$.

2.4.5. Discussion

In contrast with Jata's one dimensional shear strain estimation, 3D deformation model allows to determine the 3D strain field (3D matrix) in three planes. The 3D deformation model was created based on the classic mechanics theory [4].

The estimated strain rate using the 3D deformation model and the estimated peak temperature were used to predict the microstructure evolution at the boundary of the stir zone. Although the accurate temperature at the boundary of the stir zone is not known, it is assumed to be below 1000°C. The estimated strain rate is $\dot{\varepsilon} = 12.6\ s^{-1}$ and

$\log(\dot{\varepsilon}) = 1.101$. As shown in Fig 2-9, the dynamic recovery occurs below the 1040 °C when $\log(\dot{\varepsilon}) = 1.101$. This result matches the microstructures at the TMAZ.

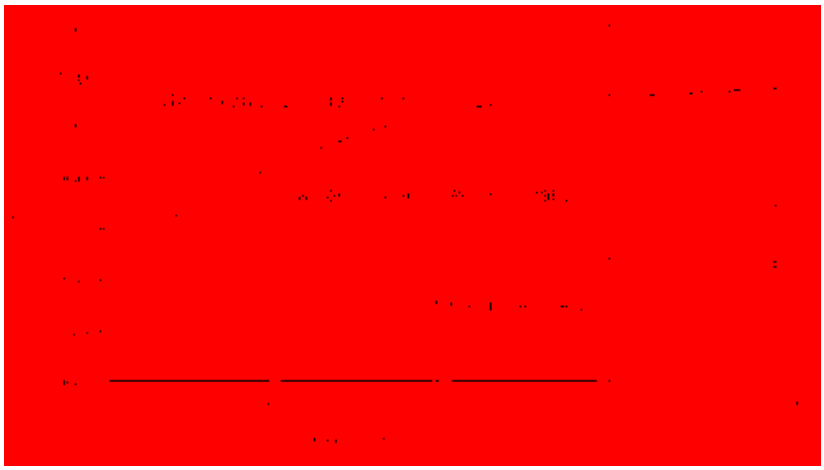

Figure 2-9 Distribution map of dynamic microstructure at a strain of 0.76 for solution treated Inconel 718.

Although this approach can be used for strain estimation in processed materials, there are still limitations. It doesn't apply if recrystallization occurs.

2.5 Conclusion

A mathematical model has been created to determine the 3D strain field, using the microstructure measurement in three orthogonal planes. The shape parameters for the model were expressed in the form of the displacement coefficients. The displacement coefficients were determined successfully using the numerical optimization method successfully.

This mathematical model was then applied to determine the 3D strain field at the boundary of the nugget zone for a Nickel base material Inconel 718. The microstructure

in the TMAZ was quantified and the shape parameters were determined. The measured shape parameters were input into the 3D deformation model. As a result, the effective strain was obtained ($\varepsilon_{eff} = 8.373$). This effective strain was used to calculate the strain rate ($\dot{\varepsilon} = 12.6\ s^{-1}$). Knowing the estimated strain rate and thermal cycles of the FSW, Inconel 718 allows us to develop a better understanding of the microstructure evolution and properties of the material. The results obtained from 3D deformation model match the related experimental results very well (Chapter 3).

The 3D deformation model developed in this study is not only applicable to the FSW process, but also for other processes which allow for the microstructure measurement in the three orthogonal planes. Based on the results of this model, the approach of estimating the strain rate was successfully developed for the FSW process. This 3D deformation model combined with the method of estimation of the strain rate can be used to analyze the microstructure evolution of FSW process under one parameter set.

3 Investigation of the Heterogeneity of Inconel 718 Coupled with Welding Thermal Cycles

3.1 Abstract

The Friction Stir Welding (FSW) materials have been studied since FSW technology was introduced. The microstructure, process parameters, thermal cycles, and mechanical properties are major topics. To discover how process parameters influence the thermal cycles and affect the microstructure and the mechanical properties would be a significant step towards a better understanding of the FSW materials. Finding the relationship among the microstructure, thermal cycles and mechanical properties is the objective of this study.

In order to reach this goal, a 3D thermocouple experiment/numerical method has been developed to determine the thermal cycles in the Heat Affected Zone (HAZ) and estimate the thermal cycles in the stir zone. A stereological method [31] was used to characterize the microstructure. The estimated strain field which has been depicted in another paper combined with the results yielded by 3D thermocouple experiment/numerical method allowed prediction of the microstructure evolution in HAZ. The peak temperature and cooling rate in the stir zone were estimated to be 1040ºC and 58 ºC/s. The strain rate was estimated to be 12.6 s^{-1} by the 3D deformation model. The

estimated strain and resultant thermal history helped to discover the microstructure evolution during the FSW process. The precipitates in different thermal zones were predicted using the estimated cooling rate and a published time-temperature transformation (TTT) diagram of wrought Inconel 718. The resultant 3-D microstructure by the stereological method shows that there are relatively rod-like grains rather than equiaxial grains in the stir zone. The mechanical properties of the weld were also investigated. The maximum hardness was found at the bottom level in the stir zone as determined by a micro-hardness test. The small grain size led to an increased hardness in the stir zone.

3.2 Introduction

Friction Stir Welding (FSW), a process invented at TWI, Cambridge, involves the joining of metals without fusion or filler materials. FSW is used in routine as well as other critical applications for the joining of structural components made of aluminum and its alloys. Recently the application of the FSW process has been extended to high melting temperature materials like Nickel based alloys.

Nickel based alloys are used in a wide variety of applications, the majority of which involve corrosion resistance and/or heat resistance [6-8]. The nickel-chromium and nickel-chromium-iron series of alloys, such as Inconel 718, provide higher strength and corrosion resistance at elevated temperatures. Inconel 718 plays an important role in industrial applications. Some of these applications include aircraft gas turbines, metal processing mills, nuclear power systems, etc. Therefore, it is desirable to develop a better understanding of FSW Inconel 718.

3.2.1 Problem Statement

Discovering the relationships among the thermal cycles, microstructure, process parameters, and mechanical properties would be important to broaden the FSW application.

The FSW process is considered a complicated thermo-mechanical process [1, 5, 6, 7]. Both thermal history and strain field need to be known in order to find how thermal cycles affect the microstructure and mechanical properties. The measurement of the thermal cycle in the stir zone is difficult due the elevated temperature and high speed moving pins during the process. Estimating the 3D strain field (Chapter 2) is another complicated task in this study. In order to determine the thermal cycles and 3D strain fields, new methods must be developed.

The overall goal of this study is to predict the properties of FSW Inconel 718 by determining the thermal cycles and estimating the 3D strain field. The 3D microstructure characterization is required in this study.

3.2.2 Microstructure and Properties of Inconel 718

Wrought Inconel 718 was selected for the current study. The original wrought Inconel 718 has a grain size of approximately 10 μm as illustrated in Fig 3-1 (a). This figure shows a large fraction of twin boundaries in the material (Fig 3-1 (a) and (b)).

Inconel 718 is hardened by γ" (Ni_3Nb) and γ' (Ni_3Al, Ni_3 (Al, Ti)) precipitates in a face-centered cubic (fcc) matrix. The γ" and γ' phases have unique morphologies which help identify the different phases [19]. The γ' phase is reported as small cuboidal or spherical particles. The γ" phase has more of a disk shape nature whose length is 5 or 6

times its thickness and is distributed in the grain [19]. The δ phase is also presented in Inconel 718. The δ phase is found mostly as plates growing on the (111) planes or nucleating on the grain boundaries and is associated with a loss of strength in this alloy. The δ phase in the grain boundaries is used to control grain size in wrought materials and seems to be important for notch ductility as well [19].

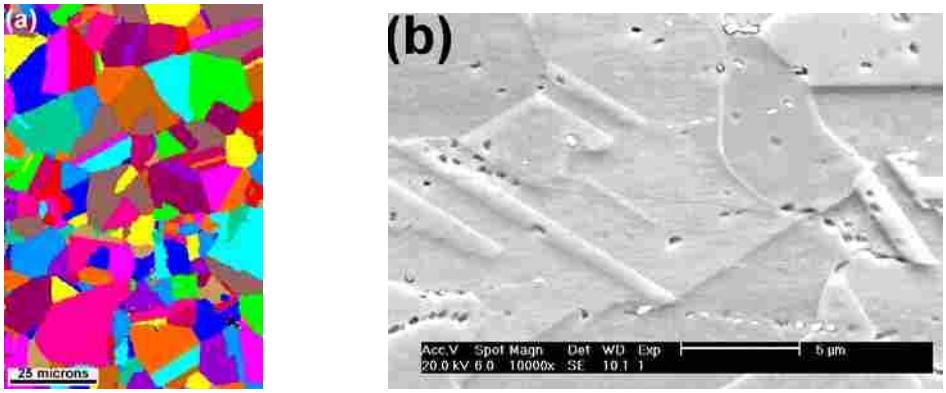

Figure 3-1 (a) OIM Scan (b) Microstructure of the base metal of Inconel 718

3.2.3 Previous Work

During FSW, the stir zone undergoes severe deformation [5, 33, 34]. Although many studies [5, 23, 24, 28, 29, 33, 34] have been done in this field, the resulting deformations and strains of Inconel 718 subjected to FSW have not been reported. Jata [5] estimated the two-dimensional strain rate in the stir zone of FSW AA7075. However, his method has limitations. Jata measured the shear strain in the thermo mechanical affected zone (TMAZ) and then extrapolated the data to the stir zone. Only two-dimensional strain was measured. Ideally the strain field should be represented in three

dimensions. Therefore, a new approach is required to determine the 3D strain field in the TMAZ of FSW Inconel 718.

Although no FSW Inconel 718 work was found in the literature, the hot working of Inconel 718 has been well reported [6, 7, 8, 15, and 16]. Yuan [35] and Wang [36] have completed systematic experiments of the hot working of Inconel 718 and plotted the relationship between the strain rate and temperature. Although their results did not provide the strain rate and temperature information for FSW Inconel 718 directly, their results do allow us to predict the microstructure evolution and properties if the thermo-mechanical history of FSW Inconel 718 are determined. Therefore, the strain, strain rate and thermal cycles of FSW 718 in the stir zone are key to develop a better understanding of the microstructure evolution and properties of FSW 718.

Two methods, thermocouples and infrared surface images, have been used to measure the temperature profile in the FSW workpiece. Using thermocouples, Owen [17] conducted two experiments to determine the time constant and temperature profile of the FSW material at different places in the workpiece. It was found that the 0.032 inch grounded thermocouples had a time constant of 0.385 second. Owen explains the process used to obtain FSW temperature measurements in 304L Stainless Steel using sixteen thermocouples in a single plane parallel to the workpiece surface.

Covington [18] employed a combination of thermocouples and an infrared image of the tool's shank as a means of optimizing the tool's heat flux and boundary conditions. His work was limited to the tool's heat input.

Owen and Covington's works provide a hint of how to measure thermal cycles across FSW Inconel 718 in the three dimensions using thermocouples.

The precipitates of Inconel 718 have been reported in the literature. Burger [7] and his colleagues have documented the effects of the starting condition on the aging response of as-forged 718 alloy. The condition of solutionized 718 alloy at 1800 ˚F started with a δ phase in the microstructure and spherodized with time.

Radavich [18] analyzed the physical metallurgy of both cast and wrought 718. The result shows that the γ″ and γ′ phase are the main strengthening phases. Their precipitation behavior is determined primarily by the amount of Nb and the temperature and time of exposure. The long time stability of 718 alloy is related to the stability of the γ″ phase, which transforms to a δ phase with increasing time and temperature.

Several papers about precipitation of intermetallic phases in the Inconel 718 have been published [6, 7, 8, 19, and 20]. It has been found that the major intermetallic phases that precipitate from the austenite matrix are the metastable γ"(DO_{22} structure) and γ′ (Ll_2 structure) phases and the equilibrium δ (DO_{α}) phase.

3.2.4 Research Objective and Methodologies Used to Reach This Goal

Predicting the precipitates and microstructure evolution in the TMAZ of FSW Inconel 718 using estimated strain rate and thermal cycles is the objective of this research. Material properties are a function of precipitates and microstructures in the material. Therefore, knowing the precipitates and microstructure evolution helps us reach the overall goal of predicting the properties of FSW materials at the boundary of the stir zone.

In order to reach the desired objective, the methodologies were developed. The thermal cycles of FSW Inconel 718 outside the stir zone were measured using thermocouple experiments. The measurement results then were used to estimate the

thermal history of stir zone using a 3D numerical methodology. The 3D deformation mode (Chapter 2), were employed to estimate the strain field at the boundary of the stir zone. A stereological approach was used to characterize the microstructure in the stir zone of FSW Inconel 718. The thermal history combined with the estimated strain allowed predicting the microstructure in the thermal mechanical affected zone (TMAZ). The relationships among the microstructure, mechanical properties, and thermal cycles were then analyzed.

The results of this study can be used to understand the properties of FSW Inconel 718. This thermocouple experimental/numerical methodology and stereological approach [31] can also be applied to the general study of other FSW materials.

3.3 Microstructure Description

To develop a better understanding of FSW Inconel 718, the microstructure in the TMAZ to be known. The properties of FSW Inconel 718 are the function of the microstructure. The objectives of this section are 1) to quantify the microstructure 2) to find the relationships among the microstructure's mechanical properties.

3.3.1 Quantification of the Grains in the Stir Zone

In order to gain a whole picture of the microstructure of FSW Inconel 718, the microstructure was characterized in three orthogonal planes using Orientation Imaging Microscopy (OIM). The three orthogonal planes are plan view (PLV), longitudinal view section (LS), and transverse view section (TS) respectively, and shown in Fig 3-2.

TS is in the plane with X and Z axes in Cartesian coordinate (Fig 3-2 (a)), while it is the plan perpendicular to the welding direction in the welding coordinate. Similarly, PVS and LS are defined by X, Y axes and Y, Z axes in Cartesian coordinate.

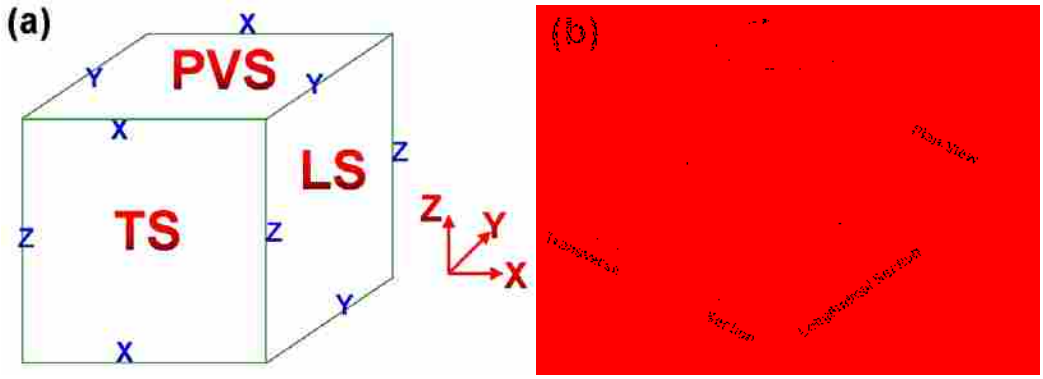

Figure 3-2 Three orthogonal planes (a) Cartesian coordinate (b) Welding coordinate

The samples were taken from the different thermal zones of FSW Inconel 718. For a certain measurement point, three samples were cut in the three orthogonal planes across this measurement point. The three samples were carefully polished and scanned by OIM. The average grain sizes in three orthogonal planes were then obtained.

In contrast to its parent metal, the stir zone of Inconel 718 has a recrystallized, fine grain structure on the order of 1-4 μm, shown in Fig 3-3. The following figures (Fig 3-3) from OIM scans demonstrate the grain size and morphology along the center line of the stir zone at different depths. Plan view samples were cut along the center line of the stir zone in different depths. Grains are small (2-20 μm) at the top surface (at the depths 0.05 mm) and relatively large (3-8 μm) at the depth next to the top surface (0.825 mm). Grains become smaller as the depth increases. The smallest grains (1-2 μm) were found at the bottom in the stir zone. The twin grain structure may introduce artificial boundaries

inside grains. To avoid wrong grain evaluation, a necessary treatment has been made to remove these artifacts (Σ 3 and Σ 9 grain boundaries) prior to the size evaluation process.

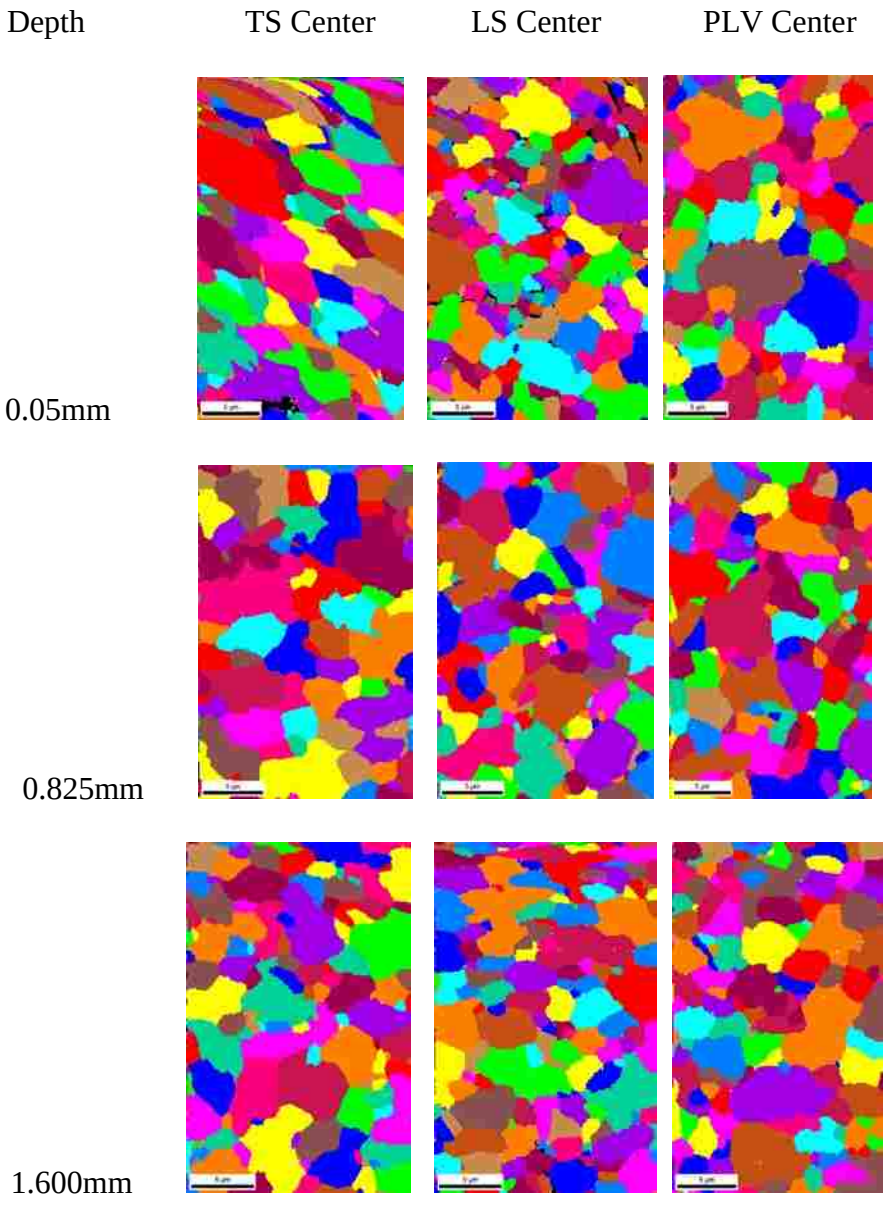

2.375mm

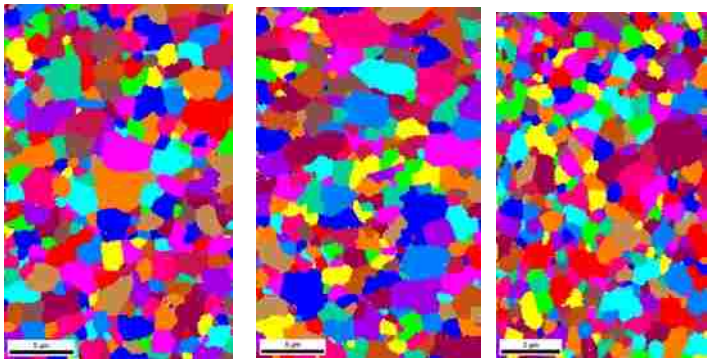

3.150mm

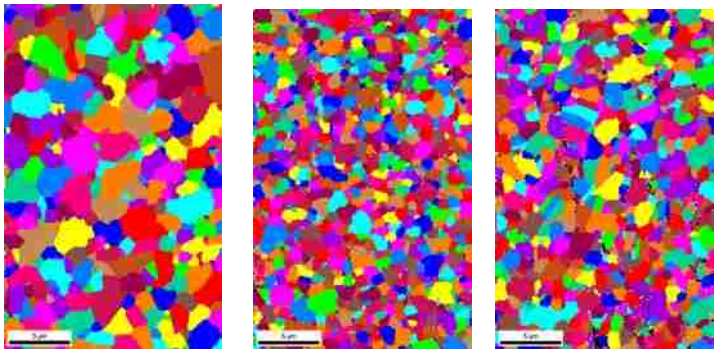

Figure 3-3 The grain morphology and grain size in the stir zone

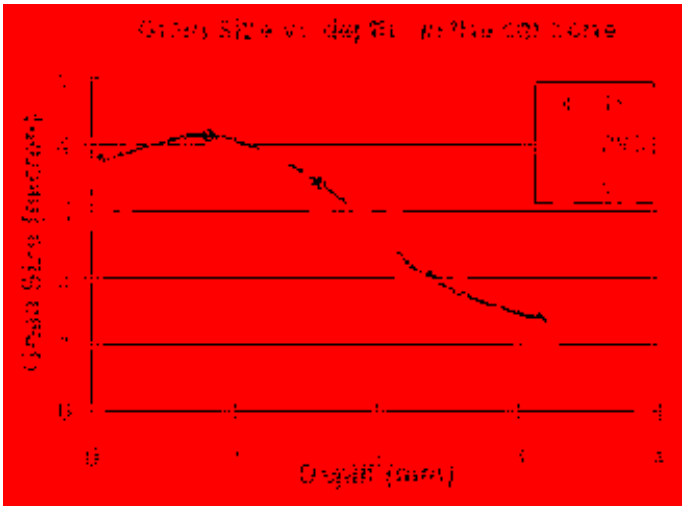

Figure 3-4 Grain size vs depths in the stir zone

The grain size was plotted as a function of depth shown in Fig 3-4. A tendency is shown that the grain size decreases as the depth increases starting at the second depth. The grain sizes of the first depth are not uniform in the top surface. In order to have a better view of the grains in the stir zone, further morphological analysis is necessary.

Table 3-1 The Grain Size (μm) at the center line, in 3 orthogonal planes

Depth	TS	LS	PVS	AVE.
0.05	3.74	2.92	3.53	3.40
0.83	4.14	3.89	3.56	3.86
1.6	3.43	3.07	3.70	3.40
2.38	1.99	1.71	1.7264	1.81
3.15	1.36	0.97	1.16	1.16
3.93	15.17	15.26	18.24	16.22

The average grain sizes of three orthogonal planes at the different depths are displayed in Table 3-1. The grain sizes listed in the table were obtained directly from the OIM analysis. The grain size calculation is based on an assumption that the grains are spheres. The diameters of the spheres are the grain sizes of the grains. The actual grains are more likely to be ellipsoidal. The grain sizes need to be recalculated based on the ellipsoidal assumption.

Assuming that the grains are ellipses rather than spheres, the 3 orthogonal axes of the grain need to be calculated. The grain sizes obtained from OIM analysis (Table 3-1) are the average diameters of the grains which are assumed to be spheres. The original grain sizes were used to calculate the three orthogonal axes of the ellipse shaped grains.

In order to simplify this model, the area of the circle (sphere in three orthogonal planes) was assumed to be equal to the area of the ellipse.

A grain in the plan-view section was taken as an example to illustrate the calculation. For a given ellipse $(x/L_x)^2 + (y/L_y)^2 = 1$, the area is $A_{ellipes} = \pi \cdot L_x \cdot L_y$. The area of a circle is calculated using $A_{circle} = \pi \cdot (D/2)^2$, where D is the diameter of this circle. Three equations were generated to solve three unknowns L_x, L_y, and L_z.

$$\begin{aligned} (D_{plv}/2)^2 &= L_x \cdot L_y \\ (D_{ts}/2)^2 &= L_x \cdot L_z \\ (D_{ls}/2)^2 &= L_y \cdot L_z \end{aligned} \quad \textbf{(3-1)}$$

The calculated ellipse axis lengths are shown in Table 3-2.

Table 3-2 The grain axis length (μm)

Depth(mm)	L(x)	L(y)	L(z)
0.05	2.26	1.38	1.55
0.83	1.90	1.67	2.26
1.6	2.07	1.66	1.42
2.38	1.00	0.74	0.98
3.15	0.81	0.41	0.57

In general, the grains in the stir zone are somewhat rod-like grains. The grains at the top surface and the second depth where the shoulder is located seem to be more elongated than the grains in other depths.

The axis lengths are plotted with the depths as shown in Fig 3-5. The same tendency that the grain size decreases as the depth increases starting at the second depth was found, compared with Fig 3-4. Fig 3-5 shows more details of the differences among the three ellipse axes. In the first two depths (the top surface and the second depth), the three axes are not uniform, which means that the grains in these depths are more elongated. The grains become more uniform as the depths increase. The two axis lengths of the grains at the bottom of the weld are very close, except one axis length. It means that the grains of the stir zone are rod-like rather than equiaxial grains. The grains at the top two levels are more elongated than the grains at the rest of depths.

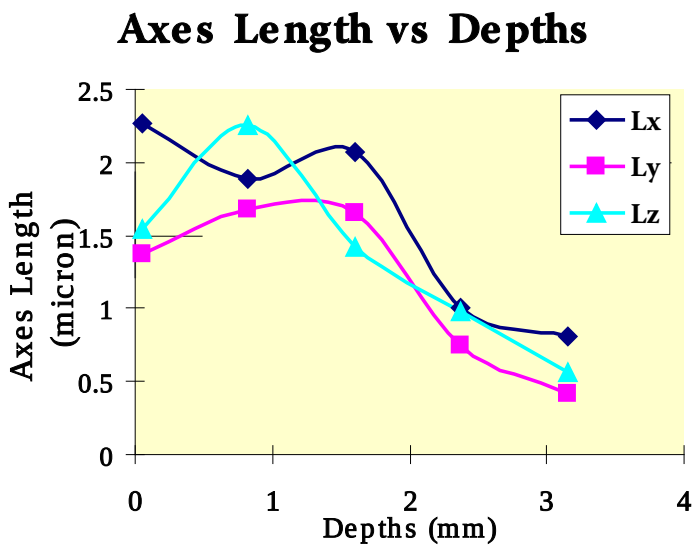

Figure 3-5 Axis lengths vs depths

3.3.2 Demonstration of the Grain Size and Hardness Plots

The grain size profile of FSW Inconel 718 in TS is demonstrated in the Fig 3-6. The grains are very fine in the stir zone and relatively large in HAZ (10-12 μm), and the largest sized grains are in the HAZ1.

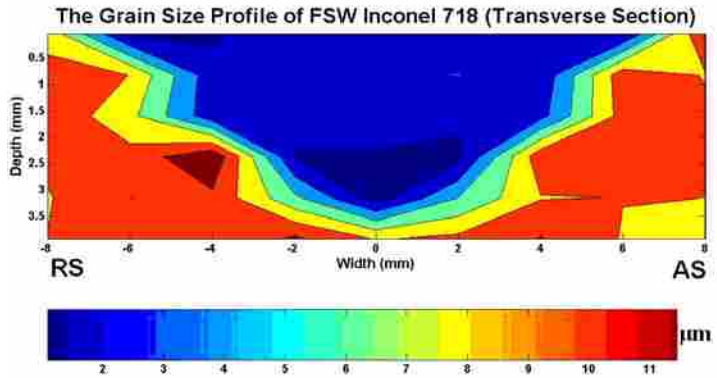

Figure 3-6 Grain size profile

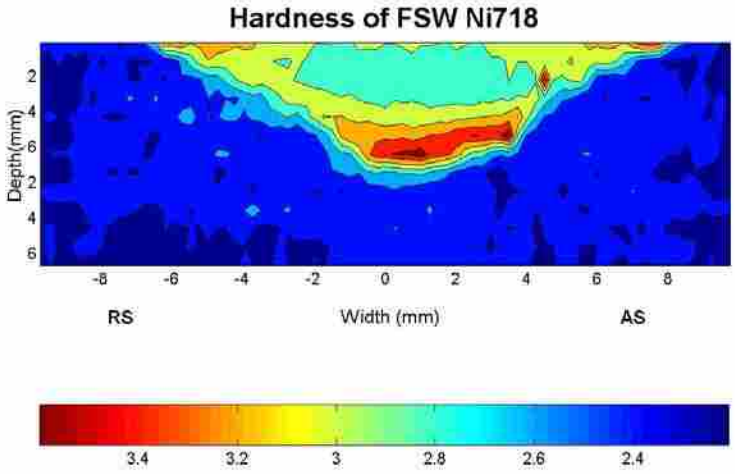

Figure 3-7 Hardness profile of FSW Inconel 718

The hardness profile of FSW Inconel 718 is illustrated in Fig 3-7. In general, the hardness in the stir zone is higher than in the HAZ, but varies in the stir zone. The maximum hardness was found at the bottom of the stir zone with relatively low hardness in the area next to the top surface.

3.4 Microstructure Discussion

In this section, the grain variation in the stir zone is correlated with the temperature. The microstructure evolution in the stir zone is explored based on the estimated strain rate and thermal cycles. The relationships among the microstructure, mechanical properties, and the thermal cycles are also presented.

3.4.1 Grain Variation in the Stir Zone

Previously, researchers [37] thought that the grains in the stir zone were equiaxed. Using the stereological method to characterize the microstructure allows to discover the variation of grain size in the stir zone. The characterized microstructure results show that the grain size has decreased at the bottom section of the stir zone relative to the top surface.

During FSW, the highest temperature, maximum strain, and longest time at elevated temperature were reached in the workpiece where the tool and shoulder intersected with the workpiece. The largest grains were found at the depth 0.825mm beneath the top surface, which corresponds to this area of interaction.

Recrystallization first occurs, followed by the grain growth due to the elevated temperature in this area. The larger grains were found at this depth near the tool shoulder.

The temperature was high where the tool shoulder rotated and interacted with the workpiece. As the tool passed to the next segment of the workpiece, the vacated area cooled quickly because of heat being transferred to the surrounding material, backing plate, and the air above the workpiece. Heat dissipation, in this manner, did not provide sufficient thermal energy for grains to grow. Mechanical deformation and frictional heating effects contributed to smaller grains at the top surface.

The smallest grains were found at the bottom of the pin. The temperature in this area was relatively low but sufficient for recrystallization. Following recrystallization, the temperature decreased and grains could no longer grow, resulting in a very fine grain size.

3.4.2 OIM Scans in the Stir Zone and TMAZ

The microstructures in the stir zone and TMAZ were characterized by OIM. The microstructures in the TMAZ and stir zone are illustrated in Fig.3-8 a) and b) respectively.

In the stir zone, the recrystallized grains were found to be fine and uniform. Twin boundaries were not found in the stir zone. The recrystallized grains and lack of twin boundaries indicated that recrystallization occurred during FSW. In the TMAZ, no recrystallized grains were found. However, there were twin boundaries in this area, indicating that no recrystallization occurred, but recovery instead.

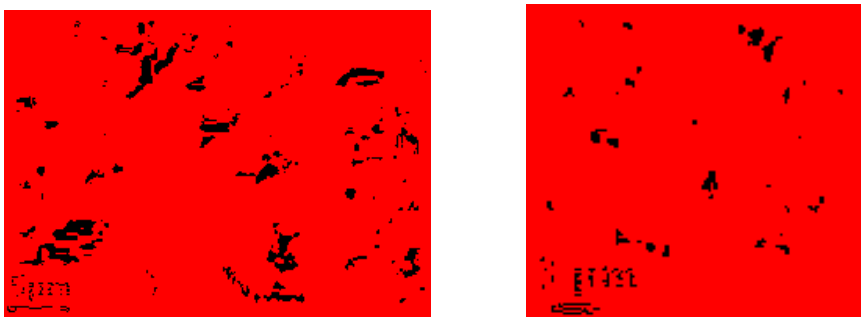

Figure 3-8 Microstructure in a) the TMAZ and b) Microstructure in the stir zone

3.4.3 The Relationship Between the Grain Size and the Hardness

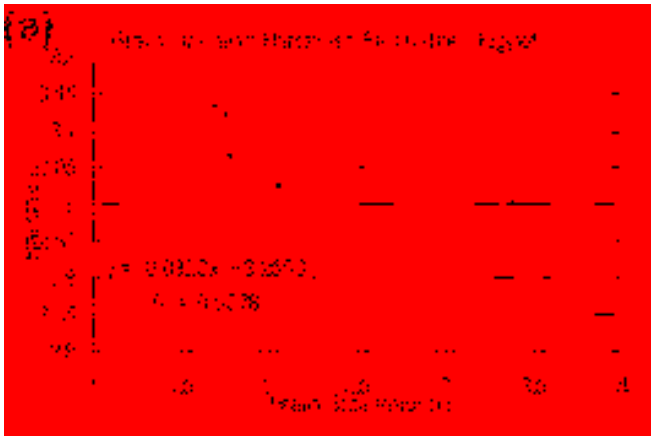

Figure 3-9 Grain Size vs hardness

Further analysis was made to explore the reasons behind the hardness variation in the stir zone. The hardness is a function of the microstructure characteristics, including the grain size and precipitates. As discussed in the previous sections, no precipitates were found in the stir zone. Therefore, the grain size may be the major factor governing the mechanical behaviors.

In order to discover the relationship between the hardness and grain size, a plot of hardness and grain size are illustrated in Fig 3-9 (a). A linear relationship was found between the grain size and hardness. The plot shows a tendency to decrease in hardness as the grain size increases.

Fig 3-9 (b) demonstrates the hardness plot and the linear fitting curve of the grain size. The two curves are shown to match up very well.

3.5 Thermal Cycle Description

3.5.1. Thermocouple Experiments

FSW was performed on a plate with embedded thermocouples in the region outside the stir zone. The purpose of this experiment was to obtain the thermal cycles in the heat affected zone (HAZ) of the FSW Inconel 718.

3.5.1.1 The Workpiece

The workpiece is an 8” X 4’ X 1/4” (0.203 m X 1.22 m X 6.35 mm) Inconel 718 plate with its edges milled and its surface ground.

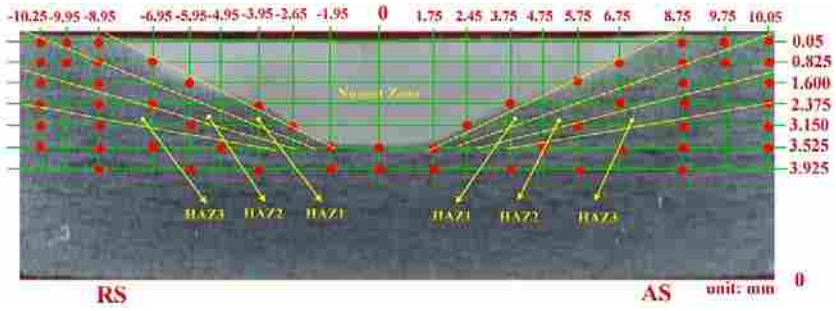

Figure 3-10 Thermocouple positions in transverse view.

A total of 56 holes were drilled for placing thermocouples in the plate. The holes were distributed along the boundary of the weld and the thermal cycle zones on both the Retreating Side (RS) and the Advancing Side (AS). This is different from Owen's work in that the thermocouples were embedded at 8 different depths rather than a single depth.

In order to illustrate the distribution of the thermocouple positions, both the transverse section (Figure 3-10) and plan-view section (Figure 3-11) were provided. The positions of the thermocouples are shown in Appendix D.

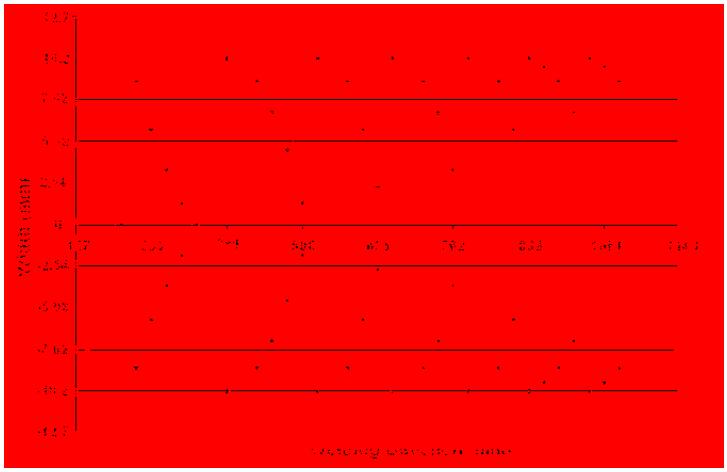

Figure 3-11 The thermocouple position in plan-view

The stir zone, HAZ1, HAZ2, and HAZ3 are defined as shown in Fig 3-10. The stir zone is the weld center. HAZ1 is about 1 mm away from the boundary of the stir zone. HAZ 2 and HAZ 3 are about 2mm and 3mm away from the boundary of the stir zone.

3.5.1.2 Fixturing

In addition to the workpiece, two plates were used to conduct the thermal experiment. The first plate was positioned directly below the workpiece and was used to accurately guide the thermocouples to the placement holes. This plate is defined as the backing plate. It is an 8”X 4 ’X 3/8” steel plate. 56 through holes were drilled at the same location as the holes in the workpiece. In addition, 56 shallow grooves were made to place the wire portion of the thermocouples as shown in Fig 3-12 (a). The thermocouple assembly, workpiece and the backing plate is illustrated in Fig 3-12 (b).

The second plate is an aluminum plate with dimensions that are the same as the workpiece. This plate is called the support plate. The support plate was placed at the bottom next to the steel backing plate.

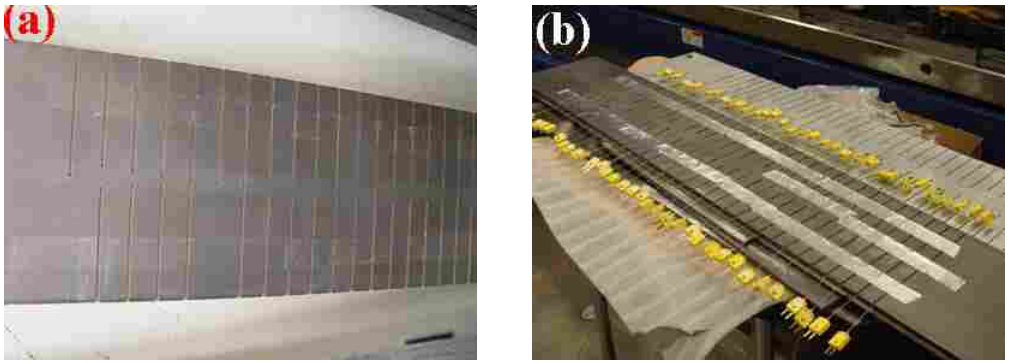

Figure 3-12 (a) The backing plate (b) The backing plate with the thermocouples

The assembly of the three plates and thermocouples are illustrated in Fig 3-13 (a) and (b). The top plate is the workpiece; the second one is the first base plate, followed by the second base plate at the bottom level.

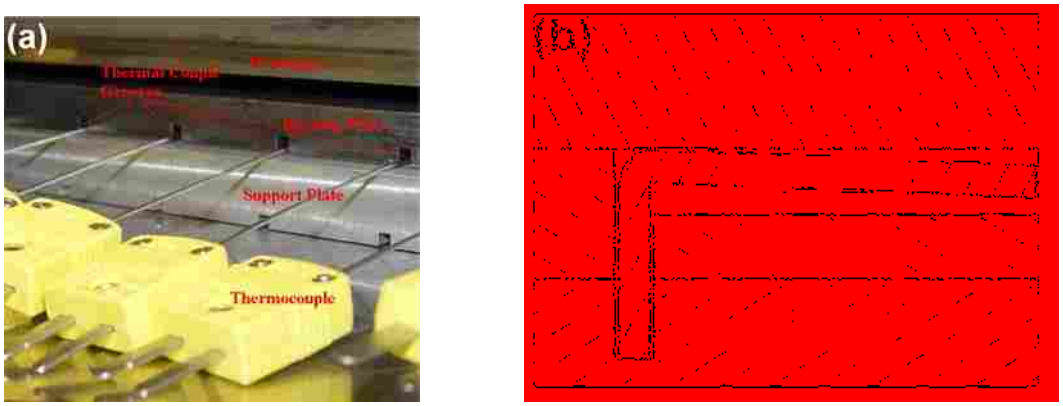

Figure 3-13 (a) Assembly of three plates with thermocouples (b) Section view of the assembly

3.5.1.3 FSW Process:

Figure 3-14 The FSW process

A polycrystalline cubic boron nitride (PCBN) tool was used, traveling at 152 mm/min and 200 RPM during the joining process. Fig 3-14 shows the FSW process. The tool dimension is attached in Appendix E and the machine data of the FSW process is shown in Appendix F.

3.5.1.4 Measurement of the Thermal Cycles in HAZ Using Thermocouple Test

A thermocouple experiment was carried out to determine the thermal history of a total of 56 positions outside the stir zone. The results of the measurement are shown in Fig 3-15.

There are couples of curves that go outside the figure due to two non-working thermocouples during the FSW process. Data was missed at these two positions. There are also two curves in the negative direction. The electric poles (positive and negative) were probably inverted, thus, leading to the negative results.

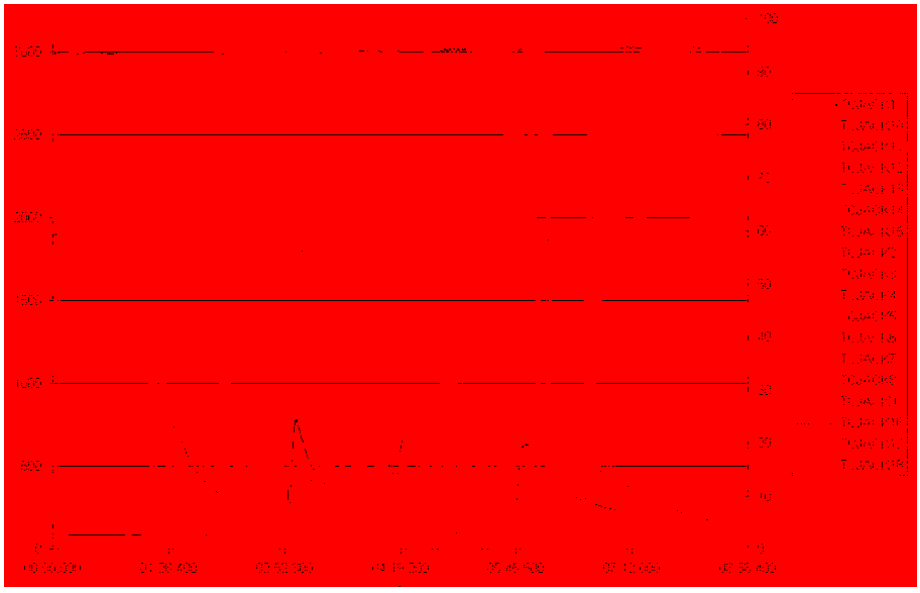

Figure 3-15 The results of the thermocouple experiment

In order to visualize the peak temperatures coupled with their locations, the peak temperatures vs locations are plotted in Fig 3-16. (Note the temperature shown in the stir zone can't be measured directly.) The remaining temperatures are measured values.

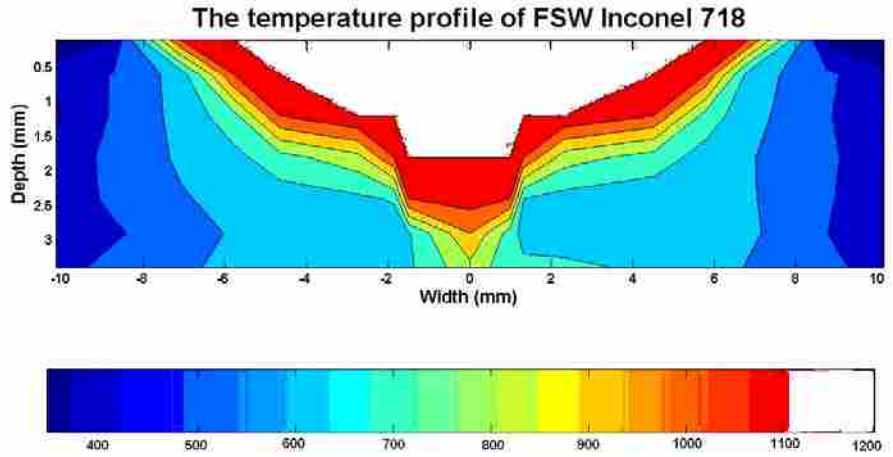

Figure 3-16 Peak temperature profile across the weld

Although the thermal cycles in the HAZ have been obtained, the temperature in the stir zone is still unknown. It is necessary to estimate the thermal history in the stir zone since the properties in the stir zone and how the thermal cycles govern the properties need to be known. The measured thermal cycles in the HAZ were used to estimate the thermal history in the stir zone.

3.5.2. Estimation of the Peak Temperature in the Stir Zone

It is difficult to measure the thermal history in the stir zone directly. Knowing the thermal history in the stir zone is important for a better understanding of the microstructure evolution and mechanical properties, which will be discussed later.

In order to determine the thermal history, the peak temperature in the stir zone must be estimated. Finite Element Analysis (FEA) was used to simulate the peak

temperature based on the measured thermal cycles in the HAZ. The estimated peak temperature in the stir zone will be used in the cooling model to estimate the thermal cycles in this zone.

This FEA model only focuses on the workpiece and the heat input flows to the workpiece. Several parameters need to be determined to perform the FEA model such as heat input. The governing equations to calculate the heat input of FSW are as follows:

$$P = 2 \cdot \pi \cdot RPM \cdot \tau / 60 \quad \textbf{(3-2)}$$

Where P is power inputted in watts, RPM is revolutions per minute, and τ is torque in Newton meters of the pin.

$$HI = \eta \cdot (P / TR) \quad \textbf{(3-3)}$$

Where HI is heat input in Joule per centimeter (J/cm), η is the process efficiency of the equipment, P is power in watts, and TR is the travel rate of the pin in centimeters per second (cm/s).

The simultaneous processes of heat conduction, convection, and radiation cause the workpiece temperature to change. Therefore, conduction, convection and radiation were applied in the FEA modeling.

A steady FEA model was created using ANSYS. The heat input from the tool was calculated using the above equation (Eq.(3-3)). The total heat input is 3.006E8 J/m. The heat input (load) was applied to the tangent surfaces to the tool in the workpiece. There

were six boundary conditions where heat transferred from the workpiece to the air through 6 surfaces in the forms of conduction, convection and radiation. Five surfaces except the bottom one underwent the conduction, convection, and radiation. Only conduction and convection were applied to the bottom surface. The thermal conductivity of the workpiece is 11.4 W/(m-ºK) (referring to this property of Inconel 718). The convection coefficient used in this model is 11 W/(m^2-ºK). The emissivity of the workpiece is 0.37 (referring an emissivity table of the common metals [10]).

The resultant temperature distribution is illustrated in Fig 3-17. The highest temperature (1007-1071 ºC) is found in the stir zone. The peak temperature in the stir zone is about 1040 ºC, which is the average value of 1007 ºC and 1071 ºC. The estimated peak temperature in the stir zone will be utilized to generate the temperature-time curve later.

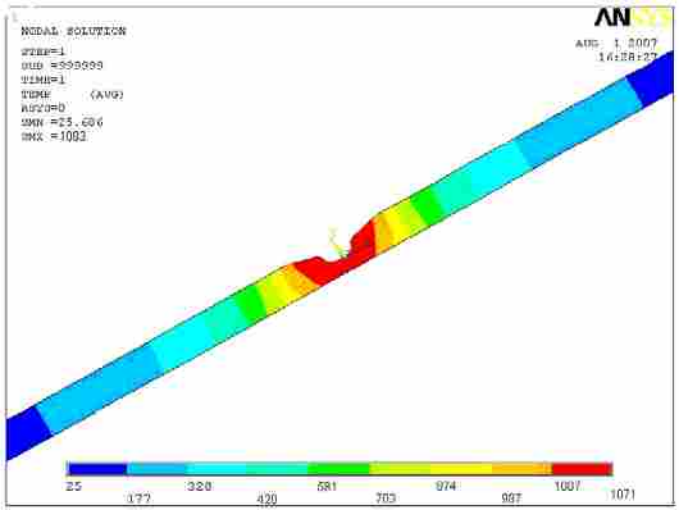

Figure 3-17 FEA results of the peak temperature in the stir zone

The simulated temperature in HAZ is in the range of 420 ~ 1007 ºC, which matches the measured temperature in HAZ (400 ~ 1100 ºC).

3.5.3 Estimation of the Cooling Rate in the Stir Zone

A cooling model was created to determine the thermal cycles in the stir zone. The experimental temperature-time plot in the HAZ and estimated peak temperature in the stir zone by FEA are needed to complete the cooling model.

The plate selected in this study is only 0.25 inch and the thermal conductivity of Inconel 718 is very low. The anvil was placed under the work piece and the thermal conductivity of the anvil is expected to be much higher than the work piece. The heat transferred to the anvil is much larger than the heat transferred internally to the work piece. Therefore, Newton's law of cooling may be applicable in this case. Using this law to analyze the heat transfer process in the stir zone, the analysis of the complicated dynamic thermal process during FSW can be simplified. The governing equation is as follows:

$$\frac{T(t)-T_{\infty}}{T_i-T_{\infty}}=\exp\left[-\left(\frac{hA_s}{\rho Vc}\right)t\right] \qquad \textbf{(3-4)}$$

Where t is time; ρ is the density; c is the specific heat capacity; h is the heat transfer coefficient; A_s is the surface area; and V is the volume.

For convenience, the above equation can be reduced to a simpler form by defining $b=\frac{hA_s}{\rho Vc}$ and solving for T(t). Equation (3-4) becomes $T(t)=(T_i-T_{\infty})e^{bt}+T_{\infty}$, which is in form of

$$T(t)=Ae^{bt}+C \qquad \textbf{(3-5)}$$

Where $A = T_i - T_\infty$ and $C = T_\infty$ are the constants.

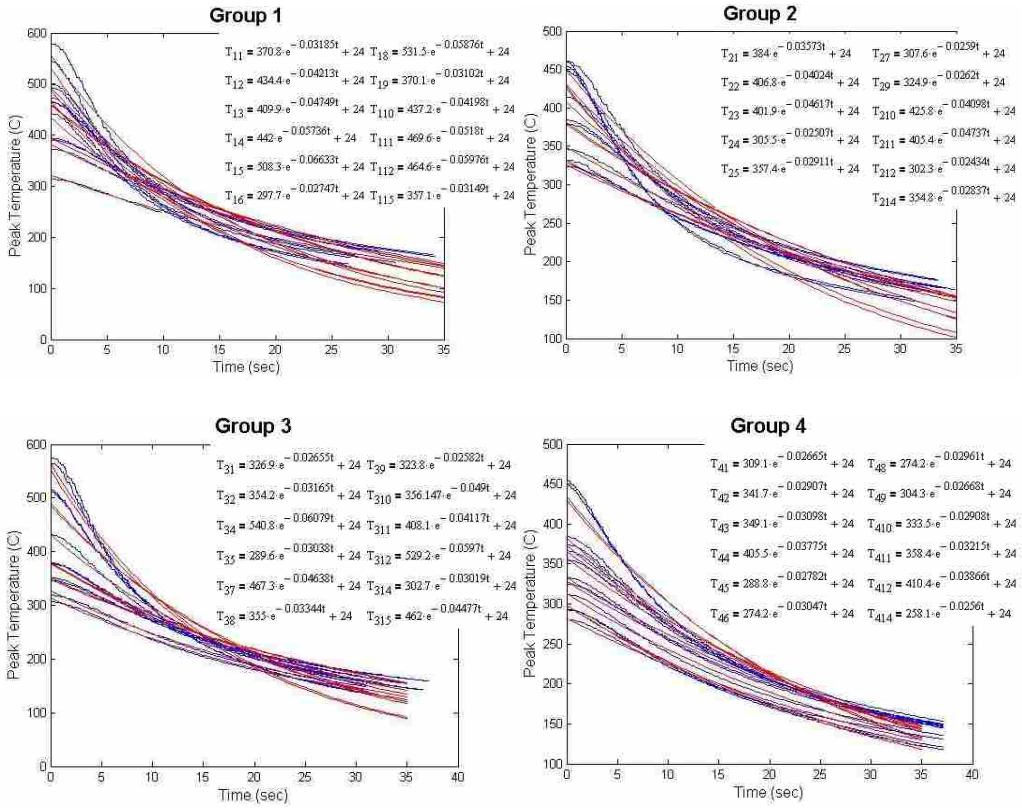

Figure 3-18 The Temperature-time plot and their exponential fitting curves a) Group1 b) Group2 c) Group3 d) Group4

In order to estimate the temperature-time curve in the stir zone based on Newton's law of cooling (Eq. (3-5)), the coefficients *A*, ***L*** and C need to be determined. The coefficient *C* is the ambient temperature (24ºC) for all the zones. The coefficient *A* is defined as the difference between the peak temperature and the ambient temperature which varies with different thermal zones. The exponential term, ***L***varies with the heat transfer coefficient *h* which depends on different thermal zones. The coefficients *A* and ***L***were determined using the curve fitting package in Matlab (noting that the coefficients

varied between thermal zones.) Matlab software provides the customer-defined curve package which allows us to set the coefficient C as a fixed constant, C=24 ºC. Then, the optimization algorithms were used to conduct optimization. Matlab automatically determined the coefficients A and *b* for the exponential fitting curves which best fit the original data plots.

Although there are 56 measurement points, some thermocouples did not work during FSW process. A total of 47 measurement results were used to create the cooling model. The experimental plots and their corresponding curve-fittings for the 47 measurement locations are demonstrated in Fig 3-18. The blue curves represent the experimental results and the red represents the fitting curves. The results are plotted in four figures, group1, group2, group3, and group4. The results were grouped according to the depths of the measurement points.

In the detailed curve fitting results, the coefficients A and b are shown in Fig 3-19. The fitted curves (shown in Fig 3-18) in the HAZ provide the trends of the coefficients *A* and $\vec{L}$. Consequently, the coefficients *A* and $\vec{L}$ were obtained and shown in Eq.(3-3), which represent the temperature-time curve in the stir zone. Upon determination of three coefficients (*A*, $\vec{L}$ and *C*), these values can be incorporated into Eq.(3-4).

As shown in Fig 3-18, the fitted curves of the 43 measurement points have been obtained. The coefficients A and b for each measurement points have been determined. In order to discover the trends of coefficients A and b, plots of the peak temperature vs coefficients A and b are plotted in Fig 3-19 (a) and (b) respectively. The curve-fittings for each were applied with results being:

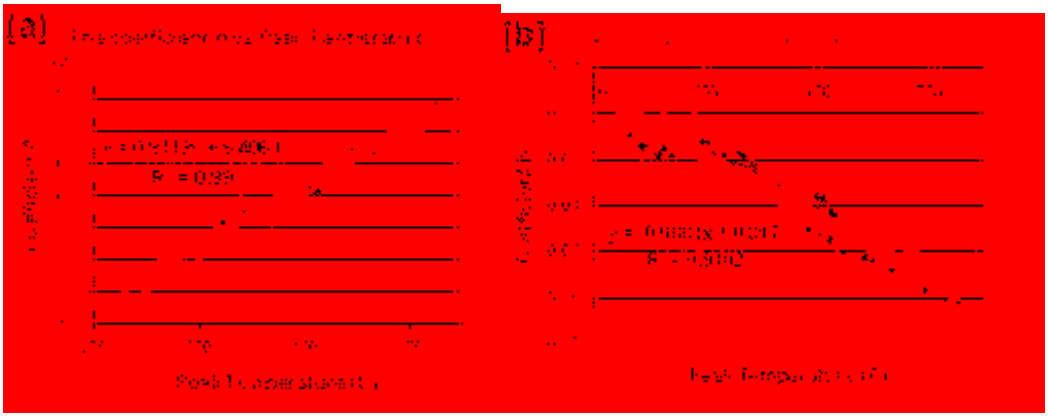

Figure 3-19 (a) Peak temp vs Coeff. A; (b) Peak temp vs Coeff. b

$$A = 0.9143 \cdot T_i + 6.4061 \quad \text{and} \quad b(T_i) = -0.0001 \cdot T_i + 0.017 \qquad \textbf{(3-6)}$$

where T_i is the peak temperature.

Obtaining the fitting equation of the coefficients A and b allows us to estimate the cooling curves of any points if the peak temperatures at the points are known.

The peak temperatures in the stir zone (1039 ºC) and TMAZ (970 ºC) have been estimated using FEM. They ($T_{i\_nugget} = 1039^0 C$ and $T_{i\_TMAZ} = 970^0 C$) were substituted into Eq. (3-6) to determine the coefficients A and b of the estimated cooling curves in the stir zone and TMAZ. After determining of the coefficients A and b, the cooling curve for the stir zone and TMAZ can be determined.

The temperature-time curve of the stir zone and TMAZ are demonstrated in Fig 3-20.

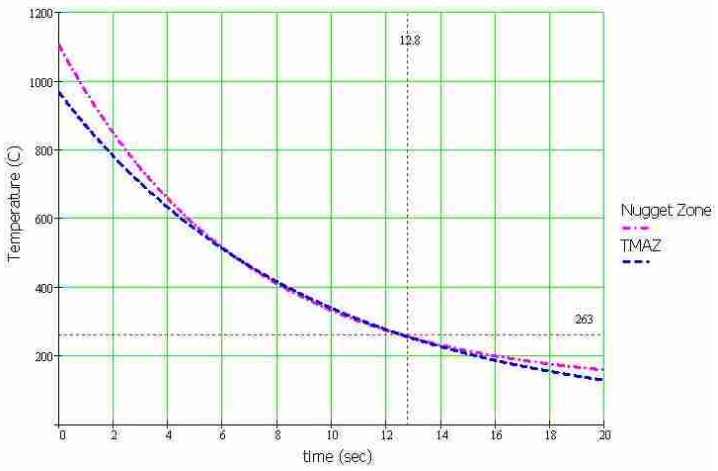

Figure 3-20 The exponential constant varies with temperature.

The average cooling rates in the different thermal zones were calculated according to the following equation:

$$Average\ Cooling\ Rate = \frac{T_h - T_l}{t_h - t_l} \quad \textbf{(3-7)}$$

Where T_h and T_l are the high and low temperatures and t_h and t_l are the times at the high and low temperatures.

One may notice that the temperatures-time curves shown in Fig 3-20 drop from the peak values to approximately 600 ºC in 12~13 sec. For convenience in calculation, the temperature 600 ºC was set as T_l in order to determine the cooling rates.

The dash dot curve displayed in Fig 3-20 is the estimated temperature-time curve for the stir zone. Its peak temperature is 1040 ºC, the time taken from 1040 ºC to 600 ºC is approximately 12.8 sec, or $t_h - t_l = 12.8\ sec$. The average cooling rate in the stir zone is calculated to be 58.18ºC/sec. The dash curve stands for the temperature behavior over

time at the boundary of the stir zone (TMAZ). In a similar manner, the average cooling rate in this area is estimated to be 51.97ºC/sec. The cooling rates in the HAZ were calculated based on the measurement results from the thermocouple experiment.

The calculated cooling rates across FSW Inconel 718 are plotted with the distance between the stir zone and each measurement point shown in Fig 3-21.

The cooling rates and the peak temperatures are relatively high if the measurement positions are close to the stir zone. The cooling rate and peak temperature reach the maximum values in the stir zone. The cooling rates in the different thermal zones allow us to predict the precipitates changes during the process.

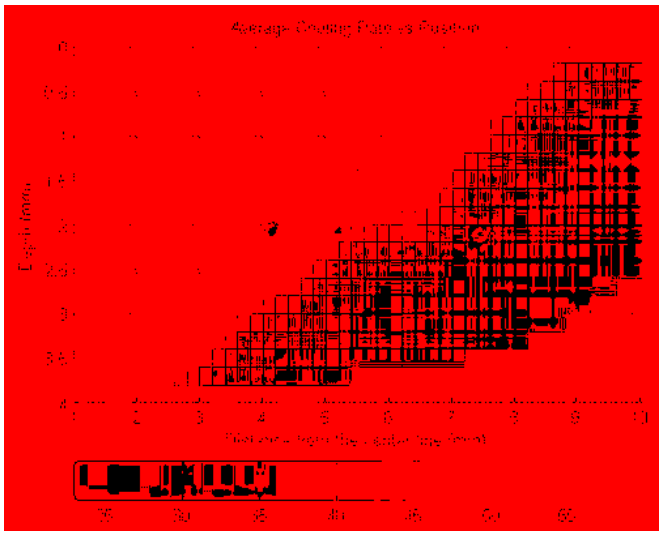

Figure 3-21 Cooling rate vs position

3.6 Thermal History Discussion

The purpose of conducting the thermocouple experiment and creating the cooling model is to predict the precipitates and microstructure evolution in the different

thermal zones. The calculated cooling rates across FSW Inconel 718 and the TTT diagram of wrought Inconel 718 helped us predict the precipitates in different thermal zone.

3.6.1 Predict the Precipitates across FSW Inconel 718

A published TTT diagram (Fig 3-22) for wrought Inconel 718 [18] was introduced to predict the precipitates changes in different thermal zones. The γ" solvus is approximately 910 ºC (1670 ºF) and the δ phase has a solvus temperature of 1010 ºC (1850 ºF) [18]. The δ phase precipitates in an approximate temperature range of 927ºC to 1010ºC, γ" forms in a range of 704ºC to 927ºC, and γ' precipitates at the temperature from 593ºC to 704ºC [18].

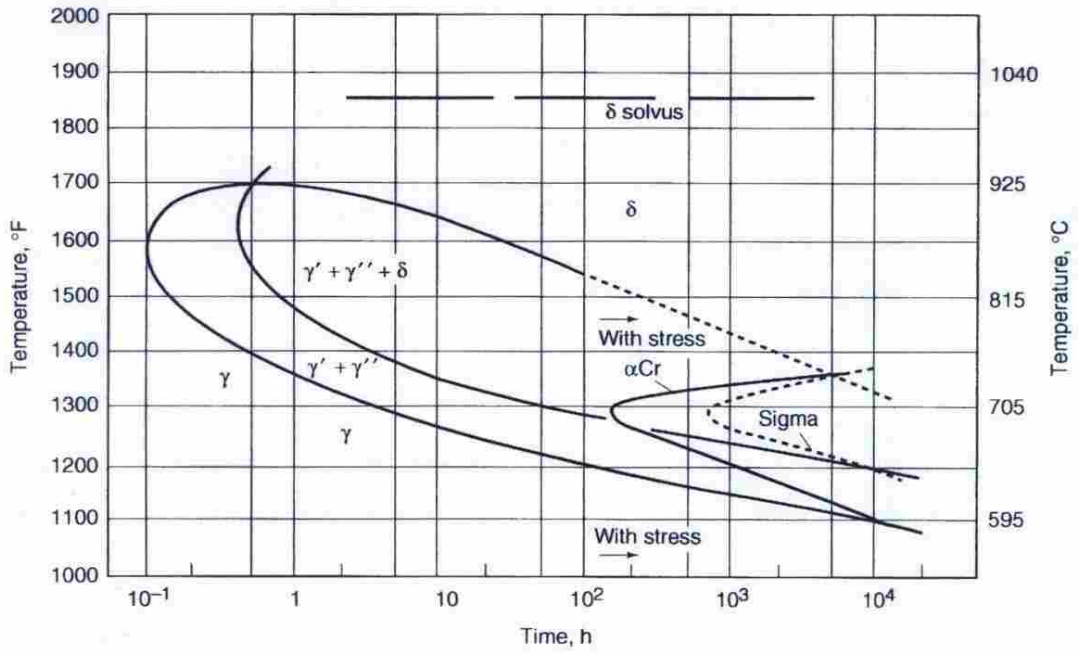

Figure 3-22 TTT diagram of Inconel 718

The calculated average cooling rates across FSW Inconel 718 were applied to the TTT diagram as shown in Fig 3-22 to demonstrate the change of precipitates during the process.

In the stir zone, the estimated peak temperature is 1040˚C and the calculated cooling rate is 58.18 ºC/sec. The cooling curve is almost a straight line perpendicular to the time axis and close to the left temperature axis shown in Fig 3-22. The δ phase solvus is approximately 1010˚C, which is lower than the peak temperature in the stir zone. Therefore, it was predicted that there were no precipitates in the stir zone. The temperature reached 1040 ºC and all the precipitates had been dissolved during the process. Once the tool left, the stir zone began cooling down. Since the cooling rate is very high (58.18 ºC/sec), it takes only 6-7 seconds to drop from 1040 ºC to 538 ºC. In this case, a solution condition can be obtained without any precipitates. The cooling curve doesn't intersect the nose of TTT diagram.

At the boundary of the stir zone, the peak temperature was estimated to be 970 ºC, which is very close to the solvus of the δ phase. The cooling rate is approximately 51.97ºC/sec which is also very close to the left temperature axis shown in Fig 3-22. Few and small precipitates are expected to be found in this zone because the peak temperature in this area is about the solvus of the δ phase. There is high percentage dissolution at this phase. The cooling rate of TMAZ is lower than the value in the stir zone but still very high. Its cooling curve doesn't touch the nose of TTT diagram. Therefore, a few phases may be formed during the cooling down process.

In the HAZ1, the measured peak temperature in the area was approximately 580 ºC and the cooling rate was calculated to be 36.2 ºC/sec. The solvus of the γ" phase is

approximately 910ºC [18]. Therefore, the peak temperature in this area didn't reach the γ" phase solvus. It was presumed that the large and small δ, γ", and γ' phases were in this zone. At the temperature 580 ºC, the δ and γ" phases were not dissolved, but instead the high temperature made the precipitates grow.

In the HAZ2, the peak temperature and cooling rate in the HAZ2 are lower than the values in HAZ1. It was predicted that there are fewer precipitates in the HAZ2 than in HAZ1.

3.6.2 Validation of the Prediction of the Precipitates

In order to validate the prediction of the precipitates across FSW Inconel 718, the precipitates in the stir zone, HAZ1, and HAZ2 were measured using Scanning Electron Microscopy (SEM). The following paragraphs detail the precipitate results in the different regions.

No precipitates were detected in the stir zone which indicates that the temperature must have reached the δ phase solvus (1010˚C). The δ precipitates and other precipitates existing in the base metal dissolved completely during the joining process. This result agrees with the prediction made in the previous section (3.6.1).

In the region near the boundary of the stir zone, only a few small precipitates were found as shown in Fig 3-23. The precipitate is probably γ" phase according to the analysis of the shape of the precipitates and results of the EDAX spot analysis. This result further proved the prediction made for this zone.

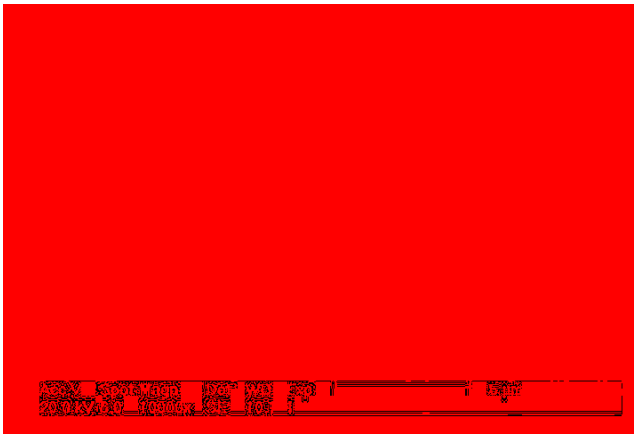

Figure 3-23 SEM observation at the boundary of the stir zone

The HAZ1 is right next to the stir zone as shown in Fig 3-10. A large amount of small (10-50 nm) and coarser precipitates (0.5-1 μm) were found in the HAZ1 on both the retreating side (RS) and the advancing side (AS) as seen in Fig 3-24.

Figure 3-24 SEM observation of HAZ1

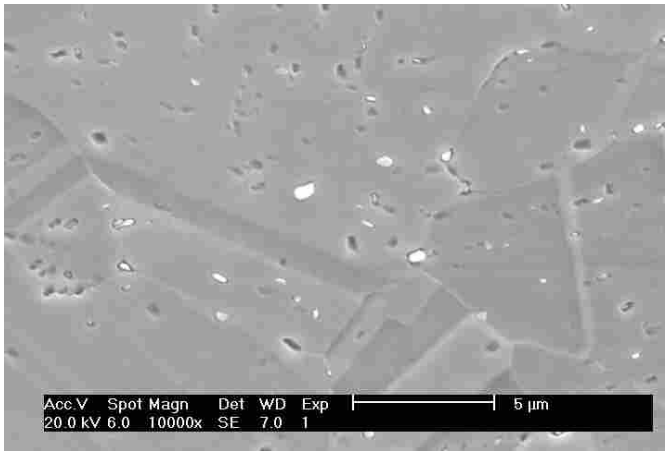

Figure 3-25 SEM analyses in HAZ2

The EDAX spot analysis shows that the precipitates contain 8-12% Nb and 55-65% Ni in this region. The δ phase and γ" phase can be distinguished by the observation of the precipitate morphology. The 1, 10 and 9 precipitates illustrated in Fig 3-24 are presumably γ" phase because of the obvious disk shape. The 3, 4, and 5 precipitates appear to be spherical or cuboidal shape and are probably δ phase. According to the shape of the small precipitates which are either cuboidal or spherical, the precipitates probably can be deduced to be δ phase.

In the HAZ2 (defined in Fig 3-10), the quantity of the precipitates in this zone decreases, compared with the precipitate quantity in the HAZ1. The size of the precipitates doesn't change. The small (10-50 nm) and coarser precipitates (1 μm) are found in this region. Fig 3-25 demonstrates the distribution and morphologies of these precipitates.

The results of EDAX chemical analysis shows that the precipitates in this region contain about Ti, 8-10% Nb, and 55-60% Nickel. The disk-like and spherical precipitates can be seen in Fig 3-25. According to the chemistry analysis results by EDAX and the

morphology of the precipitates, we can conclude that these precipitates are γ″ and δ phases.

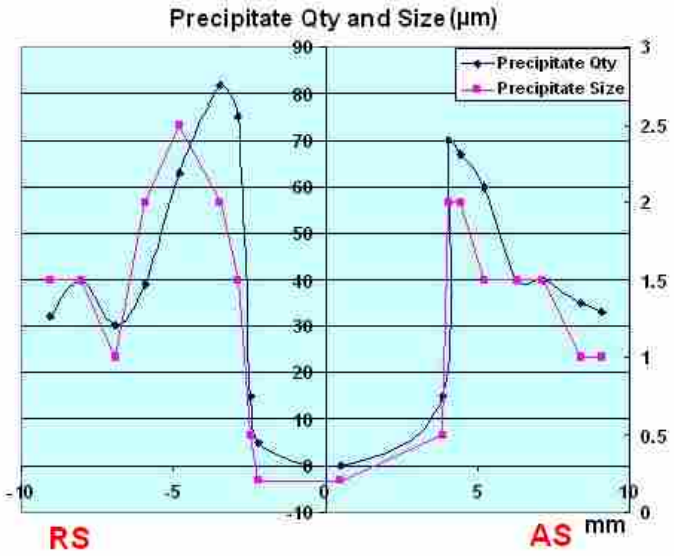

Figure 3-26 The size and quantity of the precipitates across the FSW zone

To summarize the size and quantity of the precipitates in the different zones, the curves of quantity and size are plotted at different positions in Fig 3-26. The precipitates with the maximum quantity and largest size are found in the HAZ1 where the temperature is relatively high during FSW. The size and quantity of the precipitates in the HAZ2 are smaller and lower compared with the ones in the HAZ1.

3.6.3 Predict Microstructure Evolution at the Boundary of the Stir Zone

The strain rate (12.6 s^{-1}) estimated using 3D deformation model, shown in Chapter 2, and the peak temperature (1000 ºC) at the boundary of the stir zone can be used to develop a better understanding of the microstructure evolution in this area. Yuan

[35] and his colleagues conducted the systematic experiments that focused on the hot deformation behavior (hot compression) of Inconel 718. The relationships between the percentage of dynamic recrystallized grains and the deformation temperature at different strain rate were found. The distributive map of dynamic microstructure at a strain of 0.76 was then created as seen in Fig 3-27 a) and b).

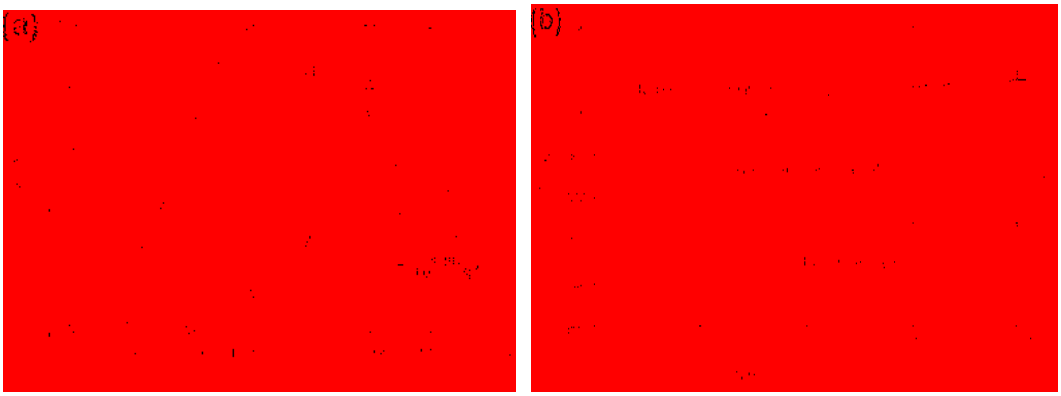

Figure 3-27 a) Relationship between the percentage of dynamic recrystallized grains (X_v) and deformation temperature at different strain rates for solution treated Inconel 718. b) Distribution map of dynamic microstructure at a strain of 0.76 for solution treated Inconel 718.

The estimated strain rate (12.6 s^{-1}) and assumed temperature (1000 ºC) at the boundary of the stir zone were compared with Yuan's results in order to explore the microstructure evolution in the stir zone. The estimated strain rate, approximately $10^{1.101}s^{-1}$ exceeds the value $10^{0}s^{-1}$. A trend is seen in Fig 3-27 (a) where the gap between the adjacent curves become smaller as the strain rate increases and the two curves of $10^{-1}s^{-1}$ and $10^{0}s^{-1}$ are very close. The gap between the curve $10^{1.101}s^{-1}$ and the curve $10^{0}s^{-1}$ are presumably smaller than the gap between the curve$10^{-1}s^{-1}$ and the curve $10^{0}s^{-1}$. A green line which represents the approximate curve for the strain rate $10^{1}s^{-1}$ was drawn in Fig 3-

27 a). This line can be used to analyze the relationship between the deformed temperature and the percentage of the recrystallization for the estimated strain rate ($10^{1.101}s^{-1}$). As displayed in Fig 27 (a), the percentage of dynamic recrystallized grains (Xv) is zero at the temperature 1000 ºC, which means no recrystallization occurs in the TMAZ.

In Fig 3-27 (b), the dynamic recovery occurs at the temperature 1000ºC and $\log(\dot{\varepsilon}/s^{-1}) = 1.101$ which is in the extension portion of $\log(\dot{\varepsilon}/s^{-1}) = 0$. This analysis of the microstructure evolution was based on the estimated strain rate and peak temperature at the boundary of the stir zone, and needs to be validated by experiments.

3.6.4 Validate the Prediction of Microstructure Evolution in TMAZ

The predication of the microstructure which has been made in the previous section needs to be validated.

The microstructure in the stir zone and TMAZ has been discussed in the section 3.4.2 (OIM scans in the stir zone and TMAZ).

The conclusion has been made that the recrystallization occurs in the stir zone, and the recovery occurs in the TMAZ.

Using 3D thermocouple experimental/numerical model methods, it has been proven that the estimated strain rate by 3D deformation model and the thermal cycles in the different zones match the related hot working results very well.

3.7 Conclusion:

It was discovered in this research that the grain sizes of Inconel 718 in the stir zone varied with depth. The maximum grains were found adjacent the top surface and

very fine grains were found at the top surface and bottom sections. The different temperatures at these various depths during FSW process led to variations in grain size.

The hardness results show that the hardness is high in the stir zone, with the highest value being located at the bottom of the stir zone. No precipitates were detected in the stir zone resulting in the grain size contributing directly to the variation of hardness in the stir zone. A linear relationship between the hardness and the grain size was discovered to decrease as the grain size increased.

The 3D thermocouple experimental/numerical combination method was developed to estimate the thermal history in the stir zone. This consequently determined the thermal cycles across the FSW Inconel 718. The peak temperature in the stir zone was estimated to be 1039 ºC using FEA. The cooling rates in each thermal zone were calculated based on the experimental and numerical results. The average cooling rate in the stir zone was found to reach 58.18 ºC/s. The estimated thermal cycles and cooling rate allow us to predict the microstructure at the boundary of the stir zone.

Although the thermocouples have been used for measuring the temperature for FSW material for several years, there has not been any systematic 3D approach to estimate the thermal cycle in the stir zone using measured temperatures and numerical methods in other zones. The 3D thermocouple experimental/numerical combination method provides an efficient approach to determine the thermal cycles across the FSW material. The results yielded by this model match the related experimental results very well. This 3D thermocouple experimental/numerical approach can be used to determine the thermal history of other FSW materials and other processes.

The TTT diagram of wrought Inconel 718 was introduced to predict the precipitates of FSW Inconel 718. The SEM experiment was carried out to validate this predication. The experiment showed that the predicted results matched the experimental results very well. There were no precipitates in the stir zone, a large amount of the δ and γ" phases were found in the HAZ1, and relatively fewer δ and γ" phases were in the HAZ2.

The estimated temperature in TMAZ (1000 ºC) combined with the estimated strain rate (12.6 s^{-1}), calculated in the 3D deformation paper, allowed us to predict the microstructure evolution in the TMAZ. A deformation map created by Yuan was then employed. The prediction of dynamic recovery without recrystallization in the TMAZ has been validated by the related deformation map. It has been proven that both 3D deformation model and 3D thermocouple experimental/numerical model are effective

4 Recommendation for Future Work

Since an assumption that the original grain size is in the same scaling as the deformed grain size was made, there is a limitation in the 3D deformation model discussed in Chapter 2.

The compress and biaxial tests must to be performed in order to validate the 3D deformation model.

The 3D deformation model could be applied to estimate FSW materials with the different process parameter sets.

The thermocouple experimental/numerical methodology could be used to create a thermal history map for other FSW materials.

5 References

[1] P.L. Threadgill, Bulletin, Friction stir welding – the state of the art, vol. 678, TWI, 1999

[2] E.D. Nicholas, W. M. Thomas, Int, J. Material. Prod. Technology 1998 (13) P45

[3] R.S. Mishra, M.W. Mahoney, Material. Sciences Forum 2001, P357-359

[4] R. H.Wagoner, Fundamentals of Metal Forming, John Wiley & Sons, Inc. 1997, P239

[5] K.V. Jata, Scripta mater. 2000 (43) P743-749

[6] Y. S. Sato, Metallurgical and Materials Transitions A, 2001, 32A 3023

[7] Y. S. Sato, Metallurgical and Materials Transitions A, 2001, 32A 3034

[8] ASM Volume 2, Nickel Alloys

[9] J.L.Burger. Superalloy 718-Metallurgy and Applications, Edited by E.A.Loria,1989. P 207-216

[10] H.L.Eiselstein, Metallurgy of a Columbium-Hardened Nickel-Chromium-Iron Alloy, ASTM STP 369, 1965, P 65-79

[11] M. Sundararaman, Metallurgical and Materials Transitions. 1998 (19A), 453-465

[12] A. Thomas, Mater Proc Tech, 2006, 177, 469-472

[13] R. Ayer, Scripta Mater 2005(53), 1383-1387

[14] C. J. Boehlert, Metallurgical and Materials Transitions, 2006 (37A), 1, page 27

[15] A. Kermanpur, Material Science, 2004(39), 7175-7182

[16] A. J. Brand, Material. Science Technology. 1996 (12) 963-969

[17] A.Lingenfelter, Superalloy 718-Metallurgy and applications Edited by E.A.Loria, 1989. P 673-683

[18]J. F.Radavich, The Physical Metallurgy of Cast and Wrought Alloy 718, Superalloy 718-Metallurgy and Applications, Edited by E.A.Loria,1989. P 229-240

[19] C. B. Owen, Two Dimensional Friction Stir Welding Model with Experimental Validation, M.S thesis, BYU, April 2006

[20] J. L.Covington, Tool Heating during Friction Stir Welding, M.S thesis, BYU, Dec. 2005

[21] M. J. Donachie and etc., Supperalloys, A Technical Guide, ASM International, March, 2002

[22]G.D.Janaki Ram, J. Material Processing Technology 2005 (167) P73-82

[23] M.QIAN, Welding Research. 150-S June 2003

[24] W.C.Liu, Metallurgical and Materials Transaction A. Volume 30A, Jan.1999-31

[25] A.Thomas, Journal of Material Processing Technology. 2006 (177) P49-472

[26]S. Mannan, Long Term Thermal Stability of Inconel Alloys 718,706,909, and Waspaloy at 593ºC and 704ºC.

[27]A. O. Basile, A Current T-T-T Diagram for Wrought Alloy 718, Superalloys 718,625 and Various Derivatives, Edited by Edward A.Loria, 1991

[28]Y. J. Chao, Journal of Manufacturing Science and Engineering. 2003, Vol 125. P 135-145

[29]S. Kalluri, The Minerals, Metal & Materials Society,1994

[30]O. Altin. Petroleum Chemistry Division Preprints 2002, 47 (3), P208

[31] C.V. Howard and M.G. Reed., Unbiased Stereology, 2005, BIOS Scientific Publishers

[32]F. Ye, and etc., Journal of Material Science 2006 (41) P5376-5379

[33] G. H. Geiger, Transport Phenomena, Addison-Wesley Publishing, 1973, ISBN 0-201-2352-0

[34] F. P. Incropera and David P.DeWitt, Introduction to Heat Transfer, John Wiley &Sons, ISBN 0-471-30458-1, 3rd ed. 1996

[35] H.Yuan, and etc., Materials Science & Engineering, A 2005 (408) P281-289.

[36] Y.Wang, and etc., Materials Science & Engineering A, 2007 (518) P356-378

[37] J. Su, Materials Science and Engineering A 2005 (405) P277-286

Appendix A. Numerical Solution of the Displacement Coefficients

The numerical solution of the displacement coefficients is shown in the following pages. Three cases were taken to demonstrate this process.

Case1

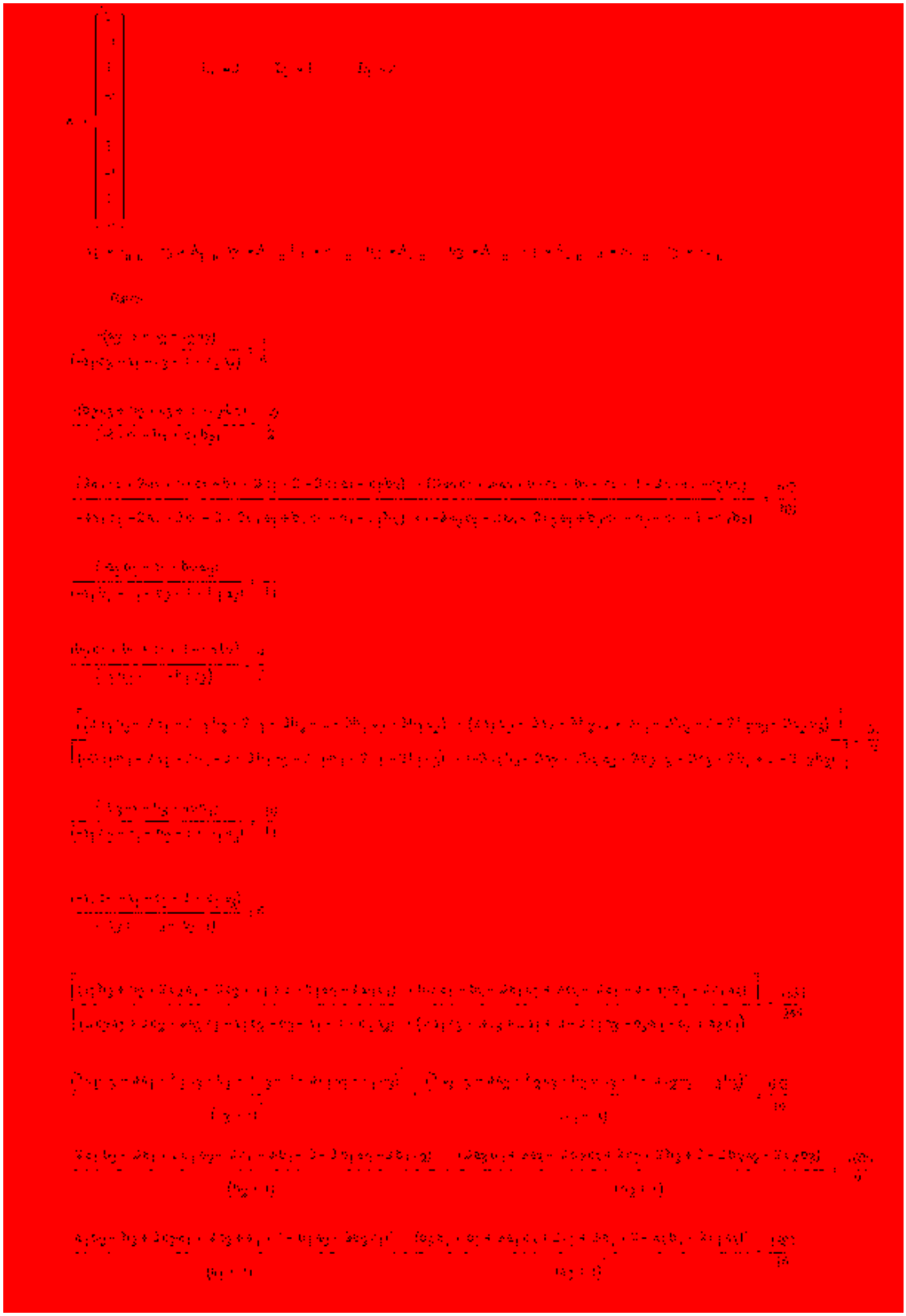

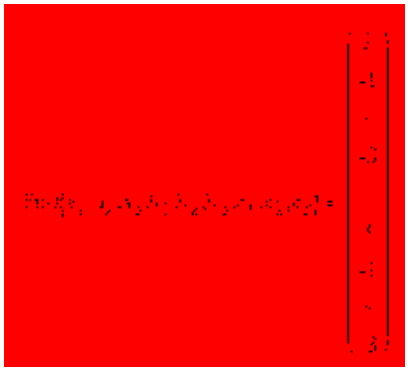

Change the initial values:

$$A := \begin{pmatrix} 2 \\ 1 \\ 3 \\ 1 \\ 2 \\ 3 \\ 2 \\ 1 \\ 3 \end{pmatrix} \qquad L_1 := 2 \qquad L_2 := 1 \qquad L_3 := 2$$

$$a_1 := A_{0,0} \quad a_2 := A_{1,0} \quad a_3 := A_{2,0} \quad b_1 := A_{3,0} \quad b_2 := A_{4,0} \quad b_3 := A_{5,0} \quad c_1 := A_{6,0} \quad c_2 := A_{7,0} \quad c_3 := A_{8,0}$$

Given

$$\frac{-\left(a_2 \cdot c_3 + a_2 - c_2 \cdot a_3\right)}{\left(-a_1 \cdot c_3 - a_1 - c_3 - 1 + c_1 \cdot a_3\right)} = \frac{1}{6}$$

$$\frac{-\left(b_2 \cdot c_3 + b_2 + c_3 + 1 - c_2 \cdot b_3\right)}{\left(-b_1 \cdot c_3 - b_1 + c_1 \cdot b_3\right)} = \frac{-9}{2}$$

$$\frac{\left(2 \cdot a_1 \cdot c_3 + 2 \cdot a_1 + b_1 \cdot c_3 + b_1 + 2 \cdot c_3 + 2 - 2 \cdot c_1 \cdot a_3 - c_1 \cdot b_3\right)^2 + \left(2 \cdot a_2 \cdot c_3 + 2 \cdot a_2 + b_2 \cdot c_3 + b_2 + c_3 + 1 - 2 \cdot c_2 \cdot a_3 - c_2 \cdot b_3\right)^2}{\left(-2 \cdot a_1 \cdot c_3 - 2 \cdot a_1 - 2 \cdot c_3 - 2 + 2 \cdot c_1 \cdot a_3 + b_1 \cdot c_3 + b_1 - c_1 \cdot b_3\right)^2 + \left(-2 \cdot a_2 \cdot c_3 - 2 \cdot a_2 + 2 \cdot c_2 \cdot a_3 + b_2 \cdot c_3 + b_2 + c_3 + 1 - c_2 \cdot b_3\right)^2} = \frac{653}{701}$$

$$\frac{\left(-a_3 \cdot b_2 - a_3 + b_3 \cdot a_2\right)}{\left(-a_1 \cdot b_2 - a_1 - b_2 - 1 + b_1 \cdot a_2\right)} = \frac{3}{11}$$

$$\frac{\left(b_2 \cdot c_3 + b_2 + c_3 + 1 - c_2 \cdot b_3\right)}{\left(c_1 \cdot b_2 + c_1 - b_1 \cdot c_2\right)} = \frac{9}{5}$$

$$\frac{\left[\left(2\cdot a_1\cdot b_2+2\cdot a_1+2\cdot c_1\cdot b_2+2\cdot c_1+2\cdot b_2+2-2\cdot b_1\cdot a_2-2\cdot b_1\cdot c_2\right)^2+\left(2\cdot a_3\cdot b_2+2\cdot a_3+2\cdot b_2\cdot c_3+2\cdot c_3+2\cdot b_2+2-2\cdot b_3\cdot a_2-2\cdot c_2\cdot b_3\right)^2\right]}{\left[\left(-2\cdot a_1\cdot b_2-2\cdot a_1-2\cdot b_2-2+2\cdot b_1\cdot a_2+2\cdot c_1\cdot b_2+2\cdot c_1-2\cdot b_1\cdot c_2\right)^2+\left(-2\cdot a_3\cdot b_2-2\cdot a_3+2\cdot b_3\cdot a_2+2\cdot b_2\cdot c_3+2\cdot c_3+2\cdot b_2+2-2\cdot c_2\cdot b_3\right)^2\right]}=\frac{50}{9}$$

$$\frac{\left(-b_3\cdot a_1-b_3+a_3\cdot b_1\right)}{\left(-a_1\cdot b_2-a_1-b_2-1+b_1\cdot a_2\right)}=\frac{10}{11}$$

$$\frac{\left(-a_1\cdot c_3-a_1-c_3-1+c_1\cdot a_3\right)}{\left(-c_2\cdot a_1-c_2+a_2\cdot c_1\right)}=6$$

$$\frac{\left[\left(a_1\cdot b_2+b_2+2\cdot c_2\cdot a_1+2\cdot c_2+a_1+1-b_1\cdot a_2-2\cdot a_2\cdot c_1\right)^2+\left(b_3\cdot a_1+b_3+2\cdot a_1\cdot c_3+2\cdot c_3+2\cdot a_1+2-a_3\cdot b_1-2\cdot c_1\cdot a_3\right)^2\right]}{\left[\left(2\cdot c_2\cdot a_1+2\cdot c_2-2\cdot a_2\cdot c_1-a_1\cdot b_2-b_2-a_1-1+b_1\cdot a_2\right)^2+\left(2\cdot a_1\cdot c_3+2\cdot c_3+2\cdot a_1+2-2\cdot c_1\cdot a_3-b_3\cdot a_1-b_3+a_3\cdot b_1\right)^2\right]}=\frac{1381}{245}$$

$$\frac{\left(2\cdot a_1\cdot c_3+2\cdot a_1+b_1\cdot c_3+b_1+2\cdot c_3+2-2\cdot c_1\cdot a_3-c_1\cdot b_3\right)^2}{\left(c_3+1\right)^2}+\frac{\left(2\cdot a_2\cdot c_3+2\cdot a_2+b_2\cdot c_3+b_2+c_3+1-2\cdot c_2\cdot a_3-c_2\cdot b_3\right)^2}{\left(c_3+1\right)^2}=\frac{653}{16}$$

$$\frac{\left(2\cdot a_1\cdot b_2+2\cdot a_1+2\cdot c_1\cdot b_2+2\cdot c_1+2\cdot b_2+2-2\cdot b_1\cdot a_2-2\cdot b_1\cdot c_2\right)^2}{\left(b_2+1\right)^2}+\frac{\left(2\cdot a_3\cdot b_2+2\cdot a_3+2\cdot b_2\cdot c_3+2\cdot c_3+2\cdot b_2+2-2\cdot b_3\cdot a_2-2\cdot c_2\cdot b_3\right)^2}{\left(b_2+1\right)^2}=\frac{1600}{9}$$

$$\frac{\left(a_1\cdot b_2+b_2+2\cdot c_2\cdot a_1+2\cdot c_2+a_1+1-b_1\cdot a_2-2\cdot a_2\cdot c_1\right)^2}{\left(a_1+1\right)^2}+\frac{\left(b_3\cdot a_1+b_3+2\cdot a_1\cdot c_3+2\cdot c_3+2\cdot a_1+2-a_3\cdot b_1-2\cdot c_1\cdot a_3\right)^2}{\left(a_1+1\right)^2}=\frac{1381}{16}$$

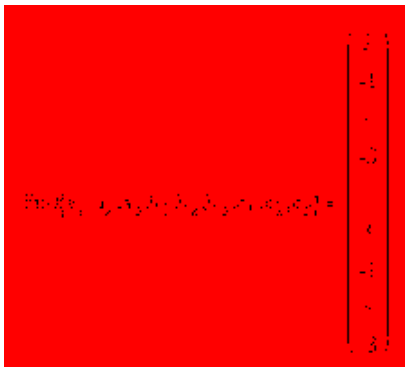

Change Initial value

$$A:=\begin{pmatrix}2\\1\\3\\4\\2\\3\\2\\1\\3\end{pmatrix}\qquad L_1:=2\qquad L_2:=1\qquad L_3:=2$$

$a_1:=A_{0,0}\quad a_2:=A_{1,0}\quad a_3:=A_{2,0}\quad b_1:=A_{3,0}\quad b_2:=A_{4,0}\quad b_3:=A_{5,0}\quad c_1:=A_{6,0}\quad c_2:=A_{7,0}\quad c_3:=A_{8,0}$

Given

$$\frac{-\left(a_2 \cdot c_3 + a_2 - c_2 \cdot a_3\right)}{\left(-a_1 \cdot c_3 - a_1 - c_3 - 1 + c_1 \cdot a_3\right)} = \frac{1}{6}$$

$$\frac{-\left(b_2 \cdot c_3 + b_2 + c_3 + 1 - c_2 \cdot b_3\right)}{\left(-b_1 \cdot c_3 - b_1 + c_1 \cdot b_3\right)} = \frac{-9}{2}$$

$$\frac{\left(2 \cdot a_1 \cdot c_3 + 2 \cdot a_1 + b_1 \cdot c_3 + b_1 + 2 \cdot c_3 + 2 - 2 \cdot c_1 \cdot a_3 - c_1 \cdot b_3\right)^2 + \left(2 \cdot a_2 \cdot c_3 + 2 \cdot a_2 + b_2 \cdot c_3 + b_2 + c_3 + 1 - 2 \cdot c_2 \cdot a_3 - c_2 \cdot b_3\right)^2}{\left(-2 \cdot a_1 \cdot c_3 - 2 \cdot a_1 - 2 \cdot c_3 - 2 + 2 \cdot c_1 \cdot a_3 + b_1 \cdot c_3 + b_1 - c_1 \cdot b_3\right)^2 + \left(-2 \cdot a_2 \cdot c_3 - 2 \cdot a_2 + 2 \cdot c_2 \cdot a_3 + b_2 \cdot c_3 + b_2 + c_3 + 1 - c_2 \cdot b_3\right)^2} = \frac{653}{701}$$

$$\frac{\left(-a_3 \cdot b_2 - a_3 + b_3 \cdot a_2\right)}{\left(-a_1 \cdot b_2 - a_1 - b_2 - 1 + b_1 \cdot a_2\right)} = \frac{3}{11}$$

$$\frac{\left(b_2 \cdot c_3 + b_2 + c_3 + 1 - c_2 \cdot b_3\right)}{\left(c_1 \cdot b_2 + c_1 - b_1 \cdot c_2\right)} = \frac{9}{5}$$

$$\frac{\left[\left(2 \cdot a_1 \cdot b_2 + 2 \cdot a_1 + 2 \cdot c_1 \cdot b_2 + 2 \cdot c_1 + 2 \cdot b_2 + 2 - 2 \cdot b_1 \cdot a_2 - 2 \cdot b_1 \cdot c_2\right)^2 + \left(2 \cdot a_3 \cdot b_2 + 2 \cdot a_3 + 2 \cdot b_2 \cdot c_3 + 2 \cdot c_3 + 2 \cdot b_2 + 2 - 2 \cdot b_3 \cdot a_2 - 2 \cdot c_2 \cdot b_3\right)^2\right]}{\left[\left(-2 \cdot a_1 \cdot b_2 - 2 \cdot a_1 - 2 \cdot b_2 - 2 + 2 \cdot b_1 \cdot a_2 + 2 \cdot c_1 \cdot b_2 + 2 \cdot c_1 - 2 \cdot b_1 \cdot c_2\right)^2 + \left(-2 \cdot a_3 \cdot b_2 - 2 \cdot a_3 + 2 \cdot b_3 \cdot a_2 + 2 \cdot b_2 \cdot c_3 + 2 \cdot c_3 + 2 \cdot b_2 + 2 - 2 \cdot c_2 \cdot b_3\right)^2\right]} = \frac{50}{9}$$

$$\frac{\left(-b_3 \cdot a_1 - b_3 + a_3 \cdot b_1\right)}{\left(-a_1 \cdot b_2 - a_1 - b_2 - 1 + b_1 \cdot a_2\right)} = \frac{10}{11}$$

$$\frac{\left(-a_1 \cdot c_3 - a_1 - c_3 - 1 + c_1 \cdot a_3\right)}{\left(-c_2 \cdot a_1 - c_2 + a_2 \cdot c_1\right)} = 6$$

$$\frac{\left[\left(a_1 \cdot b_2 + b_2 + 2 \cdot c_2 \cdot a_1 + 2 \cdot c_2 + a_1 + 1 - b_1 \cdot a_2 - 2 \cdot a_2 \cdot c_1\right)^2 + \left(b_3 \cdot a_1 + b_3 + 2 \cdot a_1 \cdot c_3 + 2 \cdot c_3 + 2 \cdot a_1 + 2 - a_3 \cdot b_1 - 2 \cdot c_1 \cdot a_3\right)^2\right]}{\left[\left(2 \cdot c_2 \cdot a_1 + 2 \cdot c_2 - 2 \cdot a_2 \cdot c_1 - a_1 \cdot b_2 - b_2 - a_1 - 1 + b_1 \cdot a_2\right)^2 + \left(2 \cdot a_1 \cdot c_3 + 2 \cdot c_3 + 2 \cdot a_1 + 2 - 2 \cdot c_1 \cdot a_3 - b_3 \cdot a_1 - b_3 + a_3 \cdot b_1\right)^2\right]} = \frac{1381}{245}$$

$$\frac{\left(2 \cdot a_1 \cdot c_3 + 2 \cdot a_1 + b_1 \cdot c_3 + b_1 + 2 \cdot c_3 + 2 - 2 \cdot c_1 \cdot a_3 - c_1 \cdot b_3\right)^2}{\left(c_3 + 1\right)^2} + \frac{\left(2 \cdot a_2 \cdot c_3 + 2 \cdot a_2 + b_2 \cdot c_3 + b_2 + c_3 + 1 - 2 \cdot c_2 \cdot a_3 - c_2 \cdot b_3\right)^2}{\left(c_3 + 1\right)^2} = \frac{653}{16}$$

$$\frac{\left(2 \cdot a_1 \cdot b_2 + 2 \cdot a_1 + 2 \cdot c_1 \cdot b_2 + 2 \cdot c_1 + 2 \cdot b_2 + 2 - 2 \cdot b_1 \cdot a_2 - 2 \cdot b_1 \cdot c_2\right)^2}{\left(b_2 + 1\right)^2} + \frac{\left(2 \cdot a_3 \cdot b_2 + 2 \cdot a_3 + 2 \cdot b_2 \cdot c_3 + 2 \cdot c_3 + 2 \cdot b_2 + 2 - 2 \cdot b_3 \cdot a_2 - 2 \cdot c_2 \cdot b_3\right)^2}{\left(b_2 + 1\right)^2} = \frac{1600}{9}$$

$$\frac{\left(a_1 \cdot b_2 + b_2 + 2 \cdot c_2 \cdot a_1 + 2 \cdot c_2 + a_1 + 1 - b_1 \cdot a_2 - 2 \cdot a_2 \cdot c_1\right)^2}{\left(a_1 + 1\right)^2} + \frac{\left(b_3 \cdot a_1 + b_3 + 2 \cdot a_1 \cdot c_3 + 2 \cdot c_3 + 2 \cdot a_1 + 2 - a_3 \cdot b_1 - 2 \cdot c_1 \cdot a_3\right)^2}{\left(a_1 + 1\right)^2} = \frac{1381}{16}$$

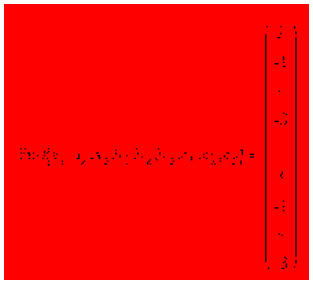

Case 2:

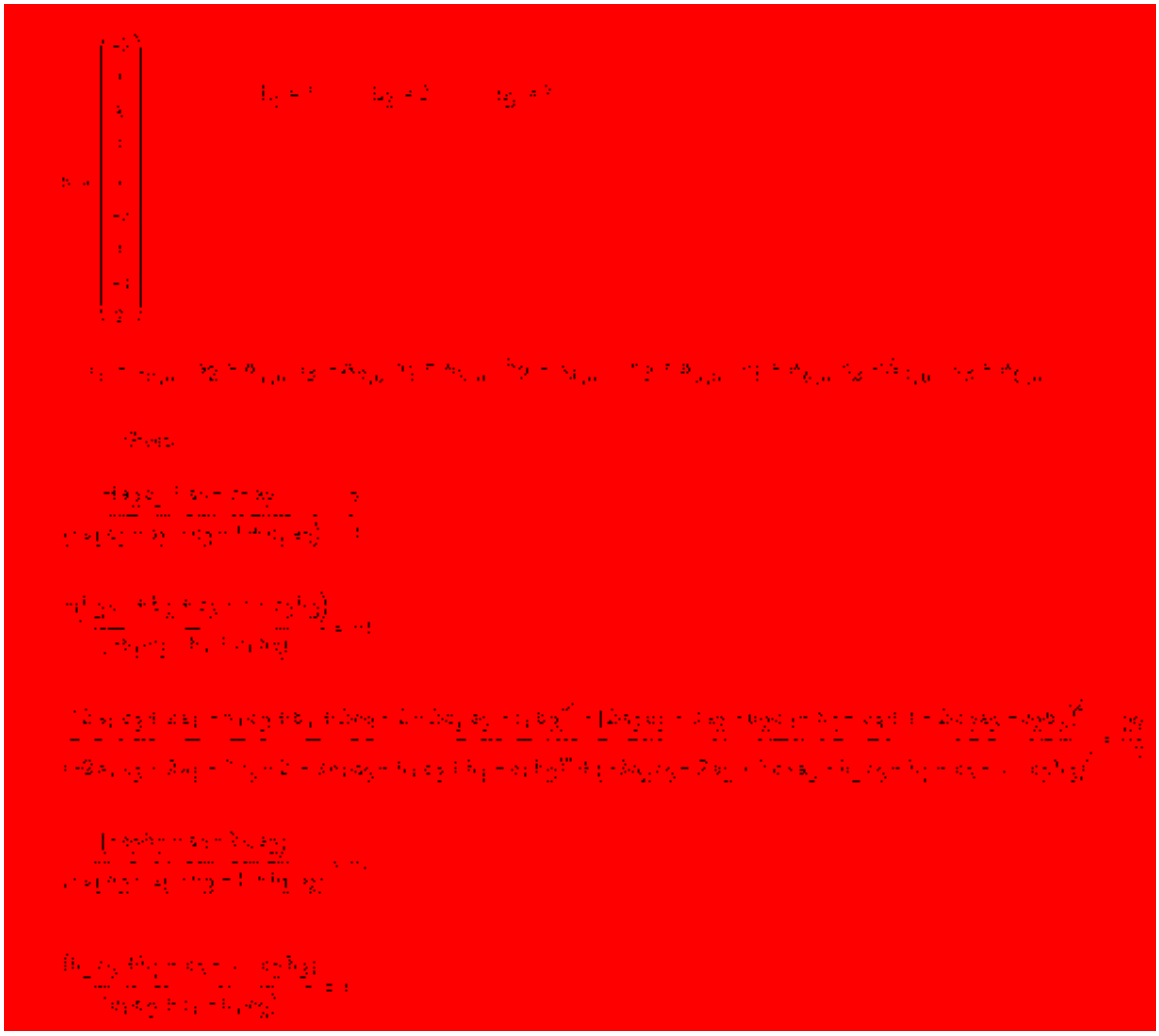

$$\frac{\left[\left(2\cdot a_1\cdot b_2+2\cdot a_1+2\cdot c_1\cdot b_2+2\cdot c_1+2\cdot b_2+2-2\cdot b_1\cdot a_2-2\cdot b_1\cdot c_2\right)^2+\left(2\cdot a_3\cdot b_2+2\cdot a_3+2\cdot b_2\cdot c_3+2\cdot c_3+2\cdot b_2+2-2\cdot b_3\cdot a_2-2\cdot c_2\cdot b_3\right)^2\right]}{\left[\left(-2\cdot a_1\cdot b_2-2\cdot a_1-2\cdot b_2-2+2\cdot b_1\cdot a_2+2\cdot c_1\cdot b_2+2\cdot c_1-2\cdot b_1\cdot c_2\right)^2+\left(-2\cdot a_3\cdot b_2-2\cdot a_3+2\cdot b_3\cdot a_2+2\cdot b_2\cdot c_3+2\cdot c_3+2\cdot b_2+2-2\cdot c_2\cdot b_3\right)^2\right]}=\frac{5}{17}$$

$$\frac{\left(-b_3\cdot a_1-b_3+a_3\cdot b_1\right)}{\left(-a_1\cdot b_2-a_1-b_2-1+b_1\cdot a_2\right)}=4$$

$$\frac{\left(-a_1\cdot c_3-a_1-c_3-1+c_1\cdot a_3\right)}{\left(-c_2\cdot a_1-c_2+a_2\cdot c_1\right)}=\frac{-1}{2}$$

$$\frac{\left[\left(a_1\cdot b_2+b_2+2\cdot c_2\cdot a_1+2\cdot c_2+a_1+1-b_1\cdot a_2-2\cdot a_2\cdot c_1\right)^2+\left(b_3\cdot a_1+b_3+2\cdot a_1\cdot c_3+2\cdot c_3+2\cdot a_1+2-a_3\cdot b_1-2\cdot c_1\cdot a_3\right)^2\right]}{\left[\left(2\cdot c_2\cdot a_1+2\cdot c_2-2\cdot a_2\cdot c_1-a_1\cdot b_2-b_2-a_1-1+b_1\cdot a_2\right)^2+\left(2\cdot a_1\cdot c_3+2\cdot c_3+2\cdot a_1+2-2\cdot c_1\cdot a_3-b_3\cdot a_1-b_3+a_3\cdot b_1\right)^2\right]}=\frac{113}{81}$$

$$\frac{\left(2\cdot a_1\cdot c_3+2\cdot a_1+b_1\cdot c_3+b_1+2\cdot c_3+2-2\cdot c_1\cdot a_3-c_1\cdot b_3\right)^2}{\left(c_3+1\right)^2}+\frac{\left(2\cdot a_2\cdot c_3+2\cdot a_2+b_2\cdot c_3+b_2+c_3+1-2\cdot c_2\cdot a_3-c_2\cdot b_3\right)^2}{\left(c_3+1\right)^2}=\frac{290}{9}$$

$$\frac{\left(2\cdot a_1\cdot b_2+2\cdot a_1+2\cdot c_1\cdot b_2+2\cdot c_1+2\cdot b_2+2-2\cdot b_1\cdot a_2-2\cdot b_1\cdot c_2\right)^2}{\left(b_2+1\right)^2}+\frac{\left(2\cdot a_3\cdot b_2+2\cdot a_3+2\cdot b_2\cdot c_3+2\cdot c_3+2\cdot b_2+2-2\cdot b_3\cdot a_2-2\cdot c_2\cdot b_3\right)^2}{\left(b_2+1\right)^2}=20$$

$$\frac{\left(a_1\cdot b_2+b_2+2\cdot c_2\cdot a_1+2\cdot c_2+a_1+1-b_1\cdot a_2-2\cdot a_2\cdot c_1\right)^2}{\left(a_1+1\right)^2}+\frac{\left(b_3\cdot a_1+b_3+2\cdot a_1\cdot c_3+2\cdot c_3+2\cdot a_1+2-a_3\cdot b_1-2\cdot c_1\cdot a_3\right)^2}{\left(a_1+1\right)^2}=\frac{113}{4}$$

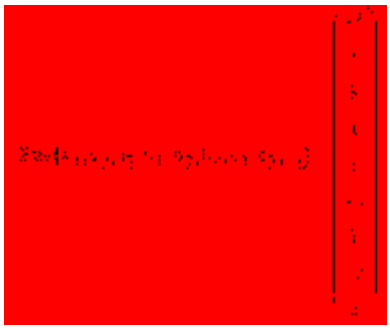

Change the initial value

$$A:=\begin{pmatrix}2\\3\\4\\1\\1\\3\\2\\1\\2\end{pmatrix}\qquad L_1:=1\qquad L_2:=2\qquad L_3:=2$$

$$a_1:=A_{0,0}\quad a_2:=A_{1,0}\quad a_3:=A_{2,0}\quad b_1:=A_{3,0}\quad b_2:=A_{4,0}\quad b_3:=A_{5,0}\quad c_1:=A_{6,0}\quad c_2:=A_{7,0}\quad c_3:=A_{8,0}$$

Given

$$\frac{-\left(a_2 \cdot c_3 + a_2 - c_2 \cdot a_3\right)}{\left(-a_1 \cdot c_3 - a_1 - c_3 - 1 + c_1 \cdot a_3\right)} = \frac{7}{2}$$

$$\frac{-\left(b_2 \cdot c_3 + b_2 + c_3 + 1 - c_2 \cdot b_3\right)}{\left(-b_1 \cdot c_3 - b_1 + c_1 \cdot b_3\right)} = -1$$

$$\frac{\left(2 \cdot a_1 \cdot c_3 + 2 \cdot a_1 + b_1 \cdot c_3 + b_1 + 2 \cdot c_3 + 2 - 2 \cdot c_1 \cdot a_3 - c_1 \cdot b_3\right)^2 + \left(2 \cdot a_2 \cdot c_3 + 2 \cdot a_2 + b_2 \cdot c_3 + b_2 + c_3 + 1 - 2 \cdot c_2 \cdot a_3 - c_2 \cdot b_3\right)^2}{\left(-2 \cdot a_1 \cdot c_3 - 2 \cdot a_1 - 2 \cdot c_3 - 2 + 2 \cdot c_1 \cdot a_3 + b_1 \cdot c_3 + b_1 - c_1 \cdot b_3\right)^2 + \left(-2 \cdot a_2 \cdot c_3 - 2 \cdot a_2 + 2 \cdot c_2 \cdot a_3 + b_2 \cdot c_3 + b_2 + c_3 + 1 - c_2 \cdot b_3\right)^2} = \frac{29}{17}$$

$$\frac{\left(-a_3 \cdot b_2 - a_3 + b_3 \cdot a_2\right)}{\left(-a_1 \cdot b_2 - a_1 - b_2 - 1 + b_1 \cdot a_2\right)} = -5$$

$$\frac{\left(b_2 \cdot c_3 + b_2 + c_3 + 1 - c_2 \cdot b_3\right)}{\left(c_1 \cdot b_2 + c_1 - b_1 \cdot c_2\right)} = 1$$

$$\frac{\left[\left(2 \cdot a_1 \cdot b_2 + 2 \cdot a_1 + 2 \cdot c_1 \cdot b_2 + 2 \cdot c_1 + 2 \cdot b_2 + 2 - 2 \cdot b_1 \cdot a_2 - 2 \cdot b_1 \cdot c_2\right)^2 + \left(2 \cdot a_3 \cdot b_2 + 2 \cdot a_3 + 2 \cdot b_2 \cdot c_3 + 2 \cdot c_3 + 2 \cdot b_2 + 2 - 2 \cdot b_3 \cdot a_2 - 2 \cdot c_2 \cdot b_3\right)^2\right]}{\left[\left(-2 \cdot a_1 \cdot b_2 - 2 \cdot a_1 - 2 \cdot b_2 - 2 + 2 \cdot b_1 \cdot a_2 + 2 \cdot c_1 \cdot b_2 + 2 \cdot c_1 - 2 \cdot b_1 \cdot c_2\right)^2 + \left(-2 \cdot a_3 \cdot b_2 - 2 \cdot a_3 + 2 \cdot b_3 \cdot a_2 + 2 \cdot b_2 \cdot c_3 + 2 \cdot c_3 + 2 \cdot b_2 + 2 - 2 \cdot c_2 \cdot b_3\right)^2\right]} = \frac{5}{17}$$

$$\frac{\left(-b_3 \cdot a_1 - b_3 + a_3 \cdot b_1\right)}{\left(-a_1 \cdot b_2 - a_1 - b_2 - 1 + b_1 \cdot a_2\right)} = 4$$

$$\frac{\left(-a_1 \cdot c_3 - a_1 - c_3 - 1 + c_1 \cdot a_3\right)}{\left(-c_2 \cdot a_1 - c_2 + a_2 \cdot c_1\right)} = \frac{-1}{2}$$

$$\frac{\left[\left(a_1 \cdot b_2 + b_2 + 2 \cdot c_2 \cdot a_1 + 2 \cdot c_2 + a_1 + 1 - b_1 \cdot a_2 - 2 \cdot a_2 \cdot c_1\right)^2 + \left(b_3 \cdot a_1 + b_3 + 2 \cdot a_1 \cdot c_3 + 2 \cdot c_3 + 2 \cdot a_1 + 2 - a_3 \cdot b_1 - 2 \cdot c_1 \cdot a_3\right)^2\right]}{\left[\left(2 \cdot c_2 \cdot a_1 + 2 \cdot c_2 - 2 \cdot a_2 \cdot c_1 - a_1 \cdot b_2 - b_2 - a_1 - 1 + b_1 \cdot a_2\right)^2 + \left(2 \cdot a_1 \cdot c_3 + 2 \cdot c_3 + 2 \cdot a_1 + 2 - 2 \cdot c_1 \cdot a_3 - b_3 \cdot a_1 - b_3 + a_3 \cdot b_1\right)^2\right]} = \frac{113}{81}$$

$$\frac{\left(2 \cdot a_1 \cdot c_3 + 2 \cdot a_1 + b_1 \cdot c_3 + b_1 + 2 \cdot c_3 + 2 - 2 \cdot c_1 \cdot a_3 - c_1 \cdot b_3\right)^2}{\left(c_3 + 1\right)^2} + \frac{\left(2 \cdot a_2 \cdot c_3 + 2 \cdot a_2 + b_2 \cdot c_3 + b_2 + c_3 + 1 - 2 \cdot c_2 \cdot a_3 - c_2 \cdot b_3\right)^2}{\left(c_3 + 1\right)^2} = \frac{290}{9}$$

$$\frac{\left(2 \cdot a_1 \cdot b_2 + 2 \cdot a_1 + 2 \cdot c_1 \cdot b_2 + 2 \cdot c_1 + 2 \cdot b_2 + 2 - 2 \cdot b_1 \cdot a_2 - 2 \cdot b_1 \cdot c_2\right)^2}{\left(b_2 + 1\right)^2} + \frac{\left(2 \cdot a_3 \cdot b_2 + 2 \cdot a_3 + 2 \cdot b_2 \cdot c_3 + 2 \cdot c_3 + 2 \cdot b_2 + 2 - 2 \cdot b_3 \cdot a_2 - 2 \cdot c_2 \cdot b_3\right)^2}{\left(b_2 + 1\right)^2} = 20$$

$$\frac{\left(a_1 \cdot b_2 + b_2 + 2 \cdot c_2 \cdot a_1 + 2 \cdot c_2 + a_1 + 1 - b_1 \cdot a_2 - 2 \cdot a_2 \cdot c_1\right)^2}{\left(a_1 + 1\right)^2} + \frac{\left(b_3 \cdot a_1 + b_3 + 2 \cdot a_1 \cdot c_3 + 2 \cdot c_3 + 2 \cdot a_1 + 2 - a_3 \cdot b_1 - 2 \cdot c_1 \cdot a_3\right)^2}{\left(a_1 + 1\right)^2} = \frac{113}{4}$$

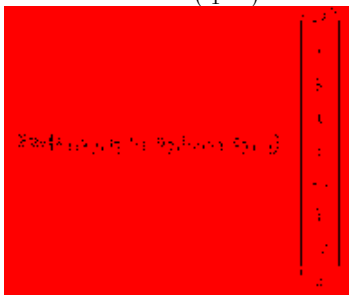

Change the initial value:

$$A := \begin{pmatrix} 2 \\ 3 \\ 4 \\ 1 \\ 1 \\ 4 \\ 2 \\ 1 \\ 2 \end{pmatrix} \qquad L_1 := 1 \qquad L_2 := 2 \qquad L_3 := 2$$

$$a_1 := A_{0,0} \quad a_2 := A_{1,0} \quad a_3 := A_{2,0} \quad b_1 := A_{3,0} \quad b_2 := A_{4,0} \quad b_3 := A_{5,0} \quad c_1 := A_{6,0} \quad c_2 := A_{7,0} \quad c_3 := A_{8,0}$$

Given

$$\frac{-\left(a_2 \cdot c_3 + a_2 - c_2 \cdot a_3\right)}{\left(-a_1 \cdot c_3 - a_1 - c_3 - 1 + c_1 \cdot a_3\right)} = \frac{7}{2}$$

$$\frac{-\left(b_2 \cdot c_3 + b_2 + c_3 + 1 - c_2 \cdot b_3\right)}{\left(-b_1 \cdot c_3 - b_1 + c_1 \cdot b_3\right)} = -1$$

$$\frac{\left(2 \cdot a_1 \cdot c_3 + 2 \cdot a_1 + b_1 \cdot c_3 + b_1 + 2 \cdot c_3 + 2 - 2 \cdot c_1 \cdot a_3 - c_1 \cdot b_3\right)^2 + \left(2 \cdot a_2 \cdot c_3 + 2 \cdot a_2 + b_2 \cdot c_3 + b_2 + c_3 + 1 - 2 \cdot c_2 \cdot a_3 - c_2 \cdot b_3\right)^2}{\left(-2 \cdot a_1 \cdot c_3 - 2 \cdot a_1 - 2 \cdot c_3 - 2 + 2 \cdot c_1 \cdot a_3 + b_1 \cdot c_3 + b_1 - c_1 \cdot b_3\right)^2 + \left(-2 \cdot a_2 \cdot c_3 - 2 \cdot a_2 + 2 \cdot c_2 \cdot a_3 + b_2 \cdot c_3 + b_2 + c_3 + 1 - c_2 \cdot b_3\right)^2} = \frac{29}{17}$$

$$\frac{\left(-a_3 \cdot b_2 - a_3 + b_3 \cdot a_2\right)}{\left(-a_1 \cdot b_2 - a_1 - b_2 - 1 + b_1 \cdot a_2\right)} = -5$$

$$\frac{\left(b_2 \cdot c_3 + b_2 + c_3 + 1 - c_2 \cdot b_3\right)}{\left(c_1 \cdot b_2 + c_1 - b_1 \cdot c_2\right)} = 1$$

$$\frac{\left[\left(2 \cdot a_1 \cdot b_2 + 2 \cdot a_1 + 2 \cdot c_1 \cdot b_2 + 2 \cdot c_1 + 2 \cdot b_2 + 2 - 2 \cdot b_1 \cdot a_2 - 2 \cdot b_1 \cdot c_2\right)^2 + \left(2 \cdot a_3 \cdot b_2 + 2 \cdot a_3 + 2 \cdot b_2 \cdot c_3 + 2 \cdot c_3 + 2 \cdot b_2 + 2 - 2 \cdot b_3 \cdot a_2 - 2 \cdot c_2 \cdot b_3\right)^2\right]}{\left[\left(-2 \cdot a_1 \cdot b_2 - 2 \cdot a_1 - 2 \cdot b_2 - 2 + 2 \cdot b_1 \cdot a_2 + 2 \cdot c_1 \cdot b_2 + 2 \cdot c_1 - 2 \cdot b_1 \cdot c_2\right)^2 + \left(-2 \cdot a_3 \cdot b_2 - 2 \cdot a_3 + 2 \cdot b_3 \cdot a_2 + 2 \cdot b_2 \cdot c_3 + 2 \cdot c_3 + 2 \cdot b_2 + 2 - 2 \cdot c_2 \cdot b_3\right)^2\right]} = \frac{5}{17}$$

$$\frac{\left(-b_3 \cdot a_1 - b_3 + a_3 \cdot b_1\right)}{\left(-a_1 \cdot b_2 - a_1 - b_2 - 1 + b_1 \cdot a_2\right)} = 4$$

$$\frac{\left(-a_1 \cdot c_3 - a_1 - c_3 - 1 + c_1 \cdot a_3\right)}{\left(-c_2 \cdot a_1 - c_2 + a_2 \cdot c_1\right)} = \frac{-1}{2}$$

$$\frac{\left[\left(a_1 \cdot b_2 + b_2 + 2 \cdot c_2 \cdot a_1 + 2 \cdot c_2 + a_1 + 1 - b_1 \cdot a_2 - 2 \cdot a_2 \cdot c_1\right)^2 + \left(b_3 \cdot a_1 + b_3 + 2 \cdot a_1 \cdot c_3 + 2 \cdot c_3 + 2 \cdot a_1 + 2 - a_3 \cdot b_1 - 2 \cdot c_1 \cdot a_3\right)^2\right]}{\left[\left(2 \cdot c_2 \cdot a_1 + 2 \cdot c_2 - 2 \cdot a_2 \cdot c_1 - a_1 \cdot b_2 - b_2 - a_1 - 1 + b_1 \cdot a_2\right)^2 + \left(2 \cdot a_1 \cdot c_3 + 2 \cdot c_3 + 2 \cdot a_1 + 2 - 2 \cdot c_1 \cdot a_3 - b_3 \cdot a_1 - b_3 + a_3 \cdot b_1\right)^2\right]} = \frac{113}{81}$$

$$\frac{\left(2 \cdot a_1 \cdot c_3 + 2 \cdot a_1 + b_1 \cdot c_3 + b_1 + 2 \cdot c_3 + 2 - 2 \cdot c_1 \cdot a_3 - c_1 \cdot b_3\right)^2}{\left(c_3 + 1\right)^2} + \frac{\left(2 \cdot a_2 \cdot c_3 + 2 \cdot a_2 + b_2 \cdot c_3 + b_2 + c_3 + 1 - 2 \cdot c_2 \cdot a_3 - c_2 \cdot b_3\right)^2}{\left(c_3 + 1\right)^2} = \frac{290}{9}$$

$$\frac{\left(2\cdot a_1\cdot b_2+2\cdot a_1+2\cdot c_1\cdot b_2+2\cdot c_1+2\cdot b_2+2-2\cdot b_1\cdot a_2-2\cdot b_1\cdot c_2\right)^2}{\left(b_2+1\right)^2}+\frac{\left(2\cdot a_3\cdot b_2+2\cdot a_3+2\cdot b_2\cdot c_3+2\cdot c_3+2\cdot b_2+2-2\cdot b_3\cdot a_2-2\cdot c_2\cdot b_3\right)^2}{\left(b_2+1\right)^2}=20$$

$$\frac{\left(a_1\cdot b_2+b_2+2\cdot c_2\cdot a_1+2\cdot c_2+a_1+1-b_1\cdot a_2-2\cdot a_2\cdot c_1\right)^2}{\left(a_1+1\right)^2}+\frac{\left(b_3\cdot a_1+b_3+2\cdot a_1\cdot c_3+2\cdot c_3+2\cdot a_1+2-a_3\cdot b_1-2\cdot c_1\cdot a_3\right)^2}{\left(a_1+1\right)^2}=\frac{113}{4}$$

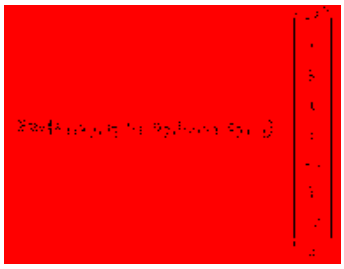

Case 3

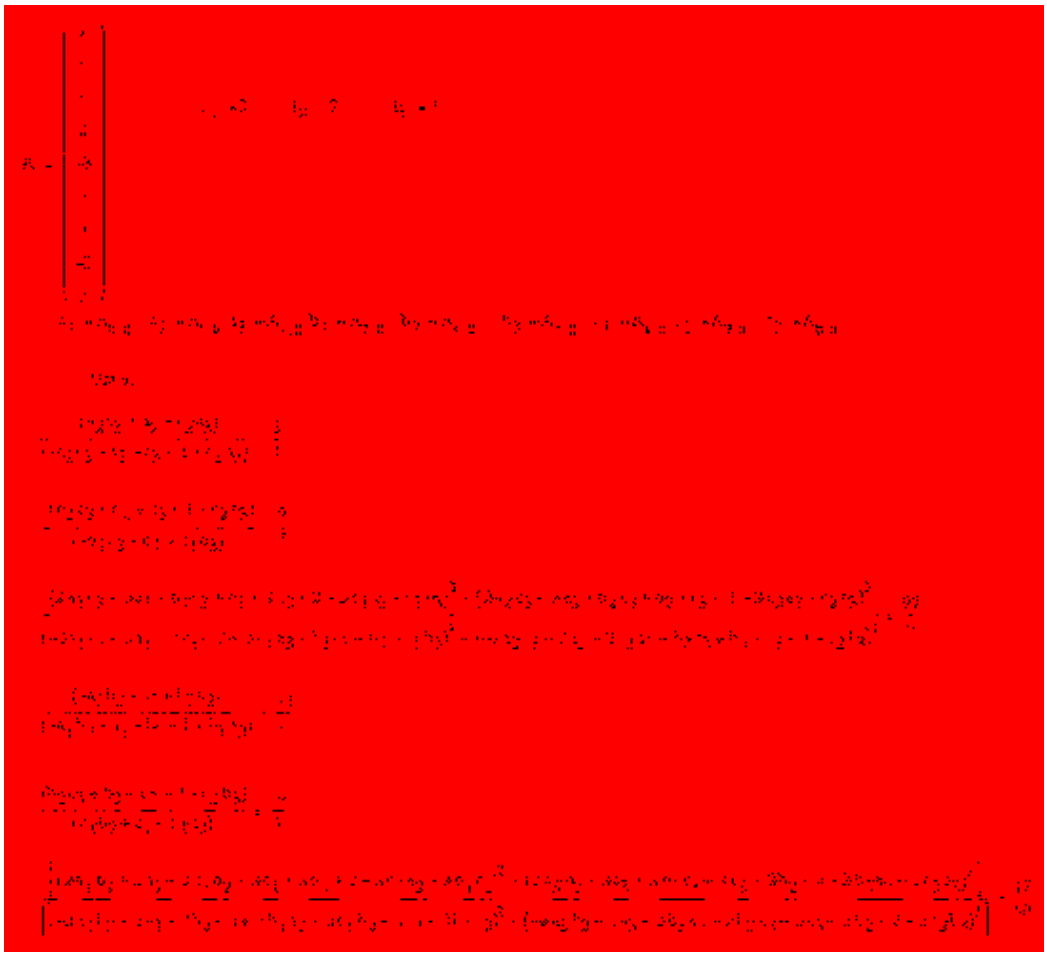

$$\frac{\left(-b_3 \cdot a_1 - b_3 + a_3 \cdot b_1\right)}{\left(-a_1 \cdot b_2 - a_1 - b_2 - 1 + b_1 \cdot a_2\right)} = \frac{1}{2}$$

$$\frac{\left(-a_1 \cdot c_3 - a_1 - c_3 - 1 + c_1 \cdot a_3\right)}{\left(-c_2 \cdot a_1 - c_2 + a_2 \cdot c_1\right)} = \frac{4}{3}$$

$$\frac{\left[\left(a_1 \cdot b_2 + b_2 + 2 \cdot c_2 \cdot a_1 + 2 \cdot c_2 + a_1 + 1 - b_1 \cdot a_2 - 2 \cdot a_2 \cdot c_1\right)^2 + \left(b_3 \cdot a_1 + b_3 + 2 \cdot a_1 \cdot c_3 + 2 \cdot c_3 + 2 \cdot a_1 + 2 - a_3 \cdot b_1 - 2 \cdot c_1 \cdot a_3\right)^2\right]}{\left[\left(2 \cdot c_2 \cdot a_1 + 2 \cdot c_2 - 2 \cdot a_2 \cdot c_1 - a_1 \cdot b_2 - b_2 - a_1 - 1 + b_1 \cdot a_2\right)^2 + \left(2 \cdot a_1 \cdot c_3 + 2 \cdot c_3 + 2 \cdot a_1 + 2 - 2 \cdot c_1 \cdot a_3 - b_3 \cdot a_1 - b_3 + a_3 \cdot b_1\right)^2\right]} = \frac{137}{41}$$

$$\frac{\left(2 \cdot a_1 \cdot c_3 + 2 \cdot a_1 + b_1 \cdot c_3 + b_1 + 2 \cdot c_3 + 2 - 2 \cdot c_1 \cdot a_3 - c_1 \cdot b_3\right)^2}{\left(c_3 + 1\right)^2} + \frac{\left(2 \cdot a_2 \cdot c_3 + 2 \cdot a_2 + b_2 \cdot c_3 + b_2 + c_3 + 1 - 2 \cdot c_2 \cdot a_3 - c_2 \cdot b_3\right)^2}{\left(c_3 + 1\right)^2} = \frac{970}{9}$$

$$\frac{\left(2 \cdot a_1 \cdot b_2 + 2 \cdot a_1 + 2 \cdot c_1 \cdot b_2 + 2 \cdot c_1 + 2 \cdot b_2 + 2 - 2 \cdot b_1 \cdot a_2 - 2 \cdot b_1 \cdot c_2\right)^2}{\left(b_2 + 1\right)^2} + \frac{\left(2 \cdot a_3 \cdot b_2 + 2 \cdot a_3 + 2 \cdot b_2 \cdot c_3 + 2 \cdot c_3 + 2 \cdot b_2 + 2 - 2 \cdot b_3 \cdot a_2 - 2 \cdot c_2 \cdot b_3\right)^2}{\left(b_2 + 1\right)^2} = \frac{272}{25}$$

$$\frac{\left(a_1 \cdot b_2 + b_2 + 2 \cdot c_2 \cdot a_1 + 2 \cdot c_2 + a_1 + 1 - b_1 \cdot a_2 - 2 \cdot a_2 \cdot c_1\right)^2}{\left(a_1 + 1\right)^2} + \frac{\left(b_3 \cdot a_1 + b_3 + 2 \cdot a_1 \cdot c_3 + 2 \cdot c_3 + 2 \cdot a_1 + 2 - a_3 \cdot b_1 - 2 \cdot c_1 \cdot a_3\right)^2}{\left(a_1 + 1\right)^2} = \frac{685}{9}$$

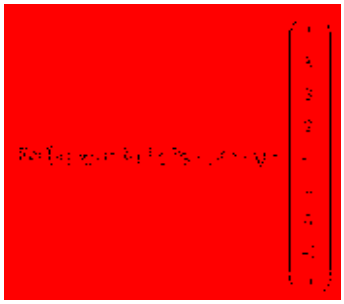

Change the initial value:

$$A := \begin{pmatrix} 2 \\ 2 \\ 4 \\ 1 \\ 4 \\ 2 \\ 1 \\ 4 \\ 2 \end{pmatrix} \qquad L_1 := 2 \qquad L_2 := 2 \qquad L_3 := 1$$

$a_1 := A_{0,0}$ $a_2 := A_{1,0}$ $a_3 := A_{2,0}$ $b_1 := A_{3,0}$ $b_2 := A_{4,0}$ $b_3 := A_{5,0}$ $c_1 := A_{6,0}$ $c_2 := A_{7,0}$ $c_3 := A_{8,0}$

Given

$$\frac{-\left(a_2 \cdot c_3 + a_2 - c_2 \cdot a_3\right)}{\left(-a_1 \cdot c_3 - a_1 - c_3 - 1 + c_1 \cdot a_3\right)} = \frac{3}{4}$$

$$\frac{-\left(b_2 \cdot c_3 + b_2 + c_3 + 1 - c_2 \cdot b_3\right)}{\left(-b_1 \cdot c_3 - b_1 + c_1 \cdot b_3\right)} = \frac{9}{7}$$

$$\frac{\left(2 \cdot a_1 \cdot c_3 + 2 \cdot a_1 + b_1 \cdot c_3 + b_1 + 2 \cdot c_3 + 2 - 2 \cdot c_1 \cdot a_3 - c_1 \cdot b_3\right)^2 + \left(2 \cdot a_2 \cdot c_3 + 2 \cdot a_2 + b_2 \cdot c_3 + b_2 + c_3 + 1 - 2 \cdot c_2 \cdot a_3 - c_2 \cdot b_3\right)^2}{\left(-2 \cdot a_1 \cdot c_3 - 2 \cdot a_1 - 2 \cdot c_3 - 2 + 2 \cdot c_1 \cdot a_3 + b_1 \cdot c_3 + b_1 - c_1 \cdot b_3\right)^2 + \left(-2 \cdot a_2 \cdot c_3 - 2 \cdot a_2 + 2 \cdot c_2 \cdot a_3 + b_2 \cdot c_3 + b_2 + c_3 + 1 - c_2 \cdot b_3\right)^2} = \frac{97}{9}$$

$$\frac{\left(-a_3 \cdot b_2 - a_3 + b_3 \cdot a_2\right)}{\left(-a_1 \cdot b_2 - a_1 - b_2 - 1 + b_1 \cdot a_2\right)} = \frac{-1}{6}$$

$$\frac{\left(b_2 \cdot c_3 + b_2 + c_3 + 1 - c_2 \cdot b_3\right)}{\left(c_1 \cdot b_2 + c_1 - b_1 \cdot c_2\right)} = \frac{-9}{4}$$

$$\frac{\left[\left(2 \cdot a_1 \cdot b_2 + 2 \cdot a_1 + 2 \cdot c_1 \cdot b_2 + 2 \cdot c_1 + 2 \cdot b_2 + 2 - 2 \cdot b_1 \cdot a_2 - 2 \cdot b_1 \cdot c_2\right)^2 + \left(2 \cdot a_3 \cdot b_2 + 2 \cdot a_3 + 2 \cdot b_2 \cdot c_3 + 2 \cdot c_3 + 2 \cdot b_2 + 2 - 2 \cdot b_3 \cdot a_2 - 2 \cdot c_2 \cdot b_3\right)^2\right]}{\left[\left(-2 \cdot a_1 \cdot b_2 - 2 \cdot a_1 - 2 \cdot b_2 - 2 + 2 \cdot b_1 \cdot a_2 + 2 \cdot c_1 \cdot b_2 + 2 \cdot c_1 - 2 \cdot b_1 \cdot c_2\right)^2 + \left(-2 \cdot a_3 \cdot b_2 - 2 \cdot a_3 + 2 \cdot b_3 \cdot a_2 + 2 \cdot b_2 \cdot c_3 + 2 \cdot c_3 + 2 \cdot b_2 + 2 - 2 \cdot c_2 \cdot b_3\right)^2\right]} = \frac{17}{50}$$

$$\frac{\left(-b_3 \cdot a_1 - b_3 + a_3 \cdot b_1\right)}{\left(-a_1 \cdot b_2 - a_1 - b_2 - 1 + b_1 \cdot a_2\right)} = \frac{1}{2}$$

$$\frac{\left(-a_1 \cdot c_3 - a_1 - c_3 - 1 + c_1 \cdot a_3\right)}{\left(-c_2 \cdot a_1 - c_2 + a_2 \cdot c_1\right)} = \frac{4}{3}$$

$$\frac{\left[\left(a_1 \cdot b_2 + b_2 + 2 \cdot c_2 \cdot a_1 + 2 \cdot c_2 + a_1 + 1 - b_1 \cdot a_2 - 2 \cdot a_2 \cdot c_1\right)^2 + \left(b_3 \cdot a_1 + b_3 + 2 \cdot a_1 \cdot c_3 + 2 \cdot c_3 + 2 \cdot a_1 + 2 - a_3 \cdot b_1 - 2 \cdot c_1 \cdot a_3\right)^2\right]}{\left[\left(2 \cdot c_2 \cdot a_1 + 2 \cdot c_2 - 2 \cdot a_2 \cdot c_1 - a_1 \cdot b_2 - b_2 - a_1 - 1 + b_1 \cdot a_2\right)^2 + \left(2 \cdot a_1 \cdot c_3 + 2 \cdot c_3 + 2 \cdot a_1 + 2 - 2 \cdot c_1 \cdot a_3 - b_3 \cdot a_1 - b_3 + a_3 \cdot b_1\right)^2\right]} = \frac{137}{41}$$

$$\frac{\left(2 \cdot a_1 \cdot c_3 + 2 \cdot a_1 + b_1 \cdot c_3 + b_1 + 2 \cdot c_3 + 2 - 2 \cdot c_1 \cdot a_3 - c_1 \cdot b_3\right)^2}{\left(c_3 + 1\right)^2} + \frac{\left(2 \cdot a_2 \cdot c_3 + 2 \cdot a_2 + b_2 \cdot c_3 + b_2 + c_3 + 1 - 2 \cdot c_2 \cdot a_3 - c_2 \cdot b_3\right)^2}{\left(c_3 + 1\right)^2} = \frac{970}{9}$$

$$\frac{\left(2 \cdot a_1 \cdot b_2 + 2 \cdot a_1 + 2 \cdot c_1 \cdot b_2 + 2 \cdot c_1 + 2 \cdot b_2 + 2 - 2 \cdot b_1 \cdot a_2 - 2 \cdot b_1 \cdot c_2\right)^2}{\left(b_2 + 1\right)^2} + \frac{\left(2 \cdot a_3 \cdot b_2 + 2 \cdot a_3 + 2 \cdot b_2 \cdot c_3 + 2 \cdot c_3 + 2 \cdot b_2 + 2 - 2 \cdot b_3 \cdot a_2 - 2 \cdot c_2 \cdot b_3\right)^2}{\left(b_2 + 1\right)^2} = \frac{272}{25}$$

$$\frac{\left(a_1 \cdot b_2 + b_2 + 2 \cdot c_2 \cdot a_1 + 2 \cdot c_2 + a_1 + 1 - b_1 \cdot a_2 - 2 \cdot a_2 \cdot c_1\right)^2}{\left(a_1 + 1\right)^2} + \frac{\left(b_3 \cdot a_1 + b_3 + 2 \cdot a_1 \cdot c_3 + 2 \cdot c_3 + 2 \cdot a_1 + 2 - a_3 \cdot b_1 - 2 \cdot c_1 \cdot a_3\right)^2}{\left(a_1 + 1\right)^2} = \frac{685}{9}$$

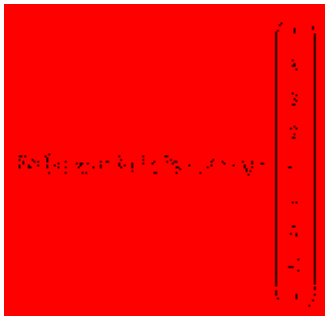

$$A := \begin{pmatrix} 2 \\ 1 \\ 2 \\ 1 \\ 4 \\ 2 \\ 1 \\ 3 \\ 2 \end{pmatrix} \qquad L_1 := 2 \qquad L_2 := 2 \qquad L_3 := 1$$

$$a_1 := A_{0,0} \quad a_2 := A_{1,0} \quad a_3 := A_{2,0} \quad b_1 := A_{3,0} \quad b_2 := A_{4,0} \quad b_3 := A_{5,0} \quad c_1 := A_{6,0} \quad c_2 := A_{7,0} \quad c_3 := A_{8,0}$$

Given

$$\frac{-\left(a_2 \cdot c_3 + a_2 - c_2 \cdot a_3\right)}{\left(-a_1 \cdot c_3 - a_1 - c_3 - 1 + c_1 \cdot a_3\right)} = \frac{3}{4}$$

$$\frac{-\left(b_2 \cdot c_3 + b_2 + c_3 + 1 - c_2 \cdot b_3\right)}{\left(-b_1 \cdot c_3 - b_1 + c_1 \cdot b_3\right)} = \frac{9}{7}$$

$$\frac{\left(2 \cdot a_1 \cdot c_3 + 2 \cdot a_1 + b_1 \cdot c_3 + b_1 + 2 \cdot c_3 + 2 - 2 \cdot c_1 \cdot a_3 - c_1 \cdot b_3\right)^2 + \left(2 \cdot a_2 \cdot c_3 + 2 \cdot a_2 + b_2 \cdot c_3 + b_2 + c_3 + 1 - 2 \cdot c_2 \cdot a_3 - c_2 \cdot b_3\right)^2}{\left(-2 \cdot a_1 \cdot c_3 - 2 \cdot a_1 - 2 \cdot c_3 - 2 + 2 \cdot c_1 \cdot a_3 + b_1 \cdot c_3 + b_1 - c_1 \cdot b_3\right)^2 + \left(-2 \cdot a_2 \cdot c_3 - 2 \cdot a_2 + 2 \cdot c_2 \cdot a_3 + b_2 \cdot c_3 + b_2 + c_3 + 1 - c_2 \cdot b_3\right)^2} = \frac{97}{9}$$

$$\frac{\left(-a_3 \cdot b_2 - a_3 + b_3 \cdot a_2\right)}{\left(-a_1 \cdot b_2 - a_1 - b_2 - 1 + b_1 \cdot a_2\right)} = \frac{-1}{6}$$

$$\frac{\left(b_2 \cdot c_3 + b_2 + c_3 + 1 - c_2 \cdot b_3\right)}{\left(c_1 \cdot b_2 + c_1 - b_1 \cdot c_2\right)} = \frac{-9}{4}$$

$$\frac{\left[\left(2 \cdot a_1 \cdot b_2 + 2 \cdot a_1 + 2 \cdot c_1 \cdot b_2 + 2 \cdot c_1 + 2 \cdot b_2 + 2 - 2 \cdot b_1 \cdot a_2 - 2 \cdot b_1 \cdot c_2\right)^2 + \left(2 \cdot a_3 \cdot b_2 + 2 \cdot a_3 + 2 \cdot b_2 \cdot c_3 + 2 \cdot c_3 + 2 \cdot b_2 + 2 - 2 \cdot b_3 \cdot a_2 - 2 \cdot c_2 \cdot b_3\right)^2\right]}{\left[\left(-2 \cdot a_1 \cdot b_2 - 2 \cdot a_1 - 2 \cdot b_2 - 2 + 2 \cdot b_1 \cdot a_2 + 2 \cdot c_1 \cdot b_2 + 2 \cdot c_1 - 2 \cdot b_1 \cdot c_2\right)^2 + \left(-2 \cdot a_3 \cdot b_2 - 2 \cdot a_3 + 2 \cdot b_3 \cdot a_2 + 2 \cdot b_2 \cdot c_3 + 2 \cdot c_3 + 2 \cdot b_2 + 2 - 2 \cdot c_2 \cdot b_3\right)^2\right]} = \frac{17}{50}$$

$$\frac{\left(-b_3 \cdot a_1 - b_3 + a_3 \cdot b_1\right)}{\left(-a_1 \cdot b_2 - a_1 - b_2 - 1 + b_1 \cdot a_2\right)} = \frac{1}{2}$$

$$\frac{\left(-a_1 \cdot c_3 - a_1 - c_3 - 1 + c_1 \cdot a_3\right)}{\left(-c_2 \cdot a_1 - c_2 + a_2 \cdot c_1\right)} = \frac{4}{3}$$

$$\frac{\left[\left(a_1 \cdot b_2 + b_2 + 2 \cdot c_2 \cdot a_1 + 2 \cdot c_2 + a_1 + 1 - b_1 \cdot a_2 - 2 \cdot a_2 \cdot c_1\right)^2 + \left(b_3 \cdot a_1 + b_3 + 2 \cdot a_1 \cdot c_3 + 2 \cdot c_3 + 2 \cdot a_1 + 2 - a_3 \cdot b_1 - 2 \cdot c_1 \cdot a_3\right)^2\right]}{\left[\left(2 \cdot c_2 \cdot a_1 + 2 \cdot c_2 - 2 \cdot a_2 \cdot c_1 - a_1 \cdot b_2 - b_2 - a_1 - 1 + b_1 \cdot a_2\right)^2 + \left(2 \cdot a_1 \cdot c_3 + 2 \cdot c_3 + 2 \cdot a_1 + 2 - 2 \cdot c_1 \cdot a_3 - b_3 \cdot a_1 - b_3 + a_3 \cdot b_1\right)^2\right]} = \frac{137}{41}$$

$$\frac{\left(2 \cdot a_1 \cdot c_3 + 2 \cdot a_1 + b_1 \cdot c_3 + b_1 + 2 \cdot c_3 + 2 - 2 \cdot c_1 \cdot a_3 - c_1 \cdot b_3\right)^2}{\left(c_3 + 1\right)^2} + \frac{\left(2 \cdot a_2 \cdot c_3 + 2 \cdot a_2 + b_2 \cdot c_3 + b_2 + c_3 + 1 - 2 \cdot c_2 \cdot a_3 - c_2 \cdot b_3\right)^2}{\left(c_3 + 1\right)^2} = \frac{970}{9}$$

$$\frac{\left(2\cdot a_1\cdot b_2 + 2\cdot a_1 + 2\cdot c_1\cdot b_2 + 2\cdot c_1 + 2\cdot b_2 + 2 - 2\cdot b_1\cdot a_2 - 2\cdot b_1\cdot c_2\right)^2}{\left(b_2 + 1\right)^2} + \frac{\left(2\cdot a_3\cdot b_2 + 2\cdot a_3 + 2\cdot b_2\cdot c_3 + 2\cdot c_3 + 2\cdot b_2 + 2 - 2\cdot b_3\cdot a_2 - 2\cdot c_2\cdot b_3\right)^2}{\left(b_2 + 1\right)^2} = \frac{272}{25}$$

$$\frac{\left(a_1\cdot b_2 + b_2 + 2\cdot c_2\cdot a_1 + 2\cdot c_2 + a_1 + 1 - b_1\cdot a_2 - 2\cdot a_2\cdot c_1\right)^2}{\left(a_1 + 1\right)^2} + \frac{\left(b_3\cdot a_1 + b_3 + 2\cdot a_1\cdot c_3 + 2\cdot c_3 + 2\cdot a_1 + 2 - a_3\cdot b_1 - 2\cdot c_1\cdot a_3\right)^2}{\left(a_1 + 1\right)^2} = \frac{685}{9}$$

$$\text{Find}\left(a_1, a_2, a_3, b_1, b_2, b_3, c_1, c_2, c_3\right) = \begin{pmatrix} 2 \\ 3 \\ 1 \\ 3 \\ 4 \\ 2 \\ 1 \\ 3 \\ 2 \end{pmatrix}$$

Appendix B. Define the Tangent Parallelogram

There are infinite tangent parallelograms for an ellipse. The tangent parallelogram has a feature that the four tangent points of the ellipse are identical to the center points of the four sides of the tangent parallelogram, and there is only one tangent parallelogram has this feature. The procedure on how to define the tangent parallelogram of the ellipse is demonstrated in Fig 2-4.

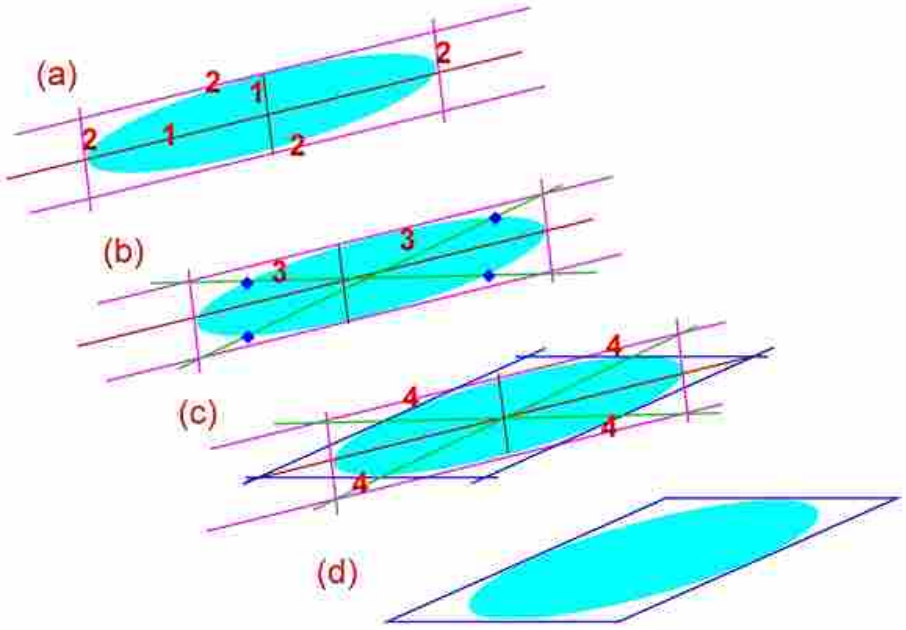

Figure B-1 Procedure on how to define the tangent parallelogram of the ellipse

The first step is to draw the major and minor axes (Lx and Ly) of the ellipse; and then, draw the four tangent lines of the ellipse that are parallel to the major and minor axes respectively as shown in Fig 2-4 (a). Thus, a tangent rectangle is created. Secondly, two diagonal lines of the created tangent rectangle were drawn. Four intersection points between the ellipse and two diagonal lines were determined, which is illustrated in Fig 2-4 (b). The third step is to draw the four tangent lines which are parallel to the two diagonal lines of the tangent rectangle respectively. These four tangent lines generate a new parallelogram, and the tangent points of this tangent parallelogram are identical to the intersection points (Fig 2-4 (b)).

Appendix C. Determine the Displacement Coefficient of FSW 718

$$A := \begin{pmatrix} 0.063 \\ 0.425 \\ 0.426 \\ 0.638 \\ 0.427 \\ 0.498 \\ 0.715 \\ 0.518 \\ 0.378 \end{pmatrix}$$

$a_1 := A_{0,0}$ $a_2 := A_{1,0}$ $a_3 := A_{2,0}$ $b_1 := A_{3,0}$ $b_2 := A_{4,0}$ $b_3 := A_{5,0}$ $c_1 := A_{6,0}$ $c_2 := A_{7,0}$ $c_3 := A_{8,0}$

Given

$$\frac{-\left(a_2 \cdot c_3 + a_2 - c_2 \cdot a_3\right)}{\left(-a_1 \cdot c_3 - a_1 - c_3 - 1 + c_1 \cdot a_3\right)} = .30400757978113054140$$

$$\frac{-\left(b_2 \cdot c_3 + b_2 + c_3 + 1 - c_2 \cdot b_3\right)}{\left(-b_1 \cdot c_3 - b_1 + c_1 \cdot b_3\right)} = 3.2671175108493965743$$

$$\frac{\left[\left(3.9 a_1 \cdot c_3 + 3.9 a_1 + 3.6 b_1 \cdot c_3 + 3.6 b_1 + 3.9 c_3 + 3.9 - 3.9 c_1 \cdot a_3 - 3.6 c_1 \cdot b_3\right)^2 + \left(3.9 a_2 \cdot c_3 + 3.9 a_2 + 3.6 b_2 \cdot c_3 + 3.6 b_2 + 3.6 c_3 + 3.6 - 3.9 c_2 \cdot a_3 - 3.6 c_2 \cdot b_3\right)^2\right]}{\left[\left(-3.9 a_1 \cdot c_3 - 3.9 a_1 - 3.9 c_3 - 3.9 + 3.9 c_1 \cdot a_3 + 3.6 b_1 \cdot c_3 + 3.6 b_1 - 3.6 c_1 \cdot b_3\right)^2 + \left(-3.9 a_2 \cdot c_3 - 3.9 a_2 + 3.9 c_2 \cdot a_3 + 3.6 b_2 \cdot c_3 + 3.6 b_2 + 3.6 c_3 + 3.6 - 3.6 c_2 \cdot b_3\right)^2\right]} = 3.35260217614750$$

$$\frac{\left(-a_3 \cdot b_2 - a_3 + b_3 \cdot a_2\right)}{\left(-a_1 \cdot b_2 - a_1 - b_2 - 1 + b_1 \cdot a_2\right)} = .31853857139139630117$$

$$\frac{\left(b_2 \cdot c_3 + b_2 + c_3 + 1 - c_2 \cdot b_3\right)}{\left(c_1 \cdot b_2 + c_1 - b_1 \cdot c_2\right)} = 2.4759021618182399238$$

$$\frac{\left(3.9 a_1 \cdot b_2 + 3.9 a_1 + 3.3 c_1 \cdot b_2 + 3.3 c_1 + 3.9 b_2 + 3.9 - 3.9 b_1 \cdot a_2 - 3.3 b_1 \cdot c_2\right)^2 + \left(3.9 a_3 \cdot b_2 + 3.9 a_3 + 3.3 b_2 \cdot c_3 + 3.3 c_3 + 3.3 b_2 + 3.3 - 3.9 b_3 \cdot a_2 - 3.3 c_2 \cdot b_3\right)^2}{\left(-3.9 a_1 \cdot b_2 - 3.9 a_1 - 3.9 b_2 - 3.9 + 3.9 b_1 \cdot a_2 + 3.3 c_1 \cdot b_2 + 3.3 c_1 - 3.3 b_1 \cdot c_2\right)^2 + \left(-3.9 a_3 \cdot b_2 - 3.9 a_3 + 3.9 b_3 \cdot a_2 + 3.3 b_2 \cdot c_3 + 3.3 c_3 + 3.3 b_2 + 3.3 - 3.3 c_2 \cdot b_3\right)^2} = 4.4139546867170191$$

$$\frac{\left(-b_3 \cdot a_1 - b_3 + a_3 \cdot b_1\right)}{\left(-a_1 \cdot b_2 - a_1 - b_2 - 1 + b_1 \cdot a_2\right)} = .20666194054390365650$$

$$\frac{\left(-a_1 \cdot c_3 - a_1 - c_3 - 1 + c_1 \cdot a_3\right)}{\left(-c_2 \cdot a_1 - c_2 + a_2 \cdot c_1\right)} = 4.6995870824602489830$$

$$\frac{\left(3.6 a_1 \cdot b_2 + 3.6 b_2 + 3.3 c_2 \cdot a_1 + 3.3 c_2 + 3.6 a_1 + 3.6 - 3.6 b_1 \cdot a_2 - 3.3 a_2 \cdot c_1\right)^2 + \left(3.6 b_3 \cdot a_1 + 3.6 b_3 + 3.3 a_1 \cdot c_3 + 3.3 c_3 + 3.3 a_1 + 3.3 - 3.6 a_3 \cdot b_1 - 3.3 c_1 \cdot a_3\right)^2}{\left(3.3 c_2 \cdot a_1 + 3.3 c_2 - 3.3 a_2 \cdot c_1 - 3.6 a_1 \cdot b_2 - 3.6 b_2 - 3.6 a_1 - 3.6 + 3.6 b_1 \cdot a_2\right)^2 + \left(3.3 a_1 \cdot c_3 + 3.3 c_3 + 3.3 a_1 + 3.3 - 3.3 c_1 \cdot a_3 - 3.6 b_3 \cdot a_1 - 3.6 b_3 + 3.6 a_3 \cdot b_1\right)^2} = 2.326031388261695848$$

$$\frac{\left(3.9 a_1 \cdot c_3 + 3.9 a_1 + 3.6 b_1 \cdot c_3 + 3.6 b_1 + 3.9 c_3 + 3.9 - 3.9 c_1 \cdot a_3 - 3.6 c_1 \cdot b_3\right)^2}{\left(c_3 + 1\right)^2} + \frac{\left(3.9 a_2 \cdot c_3 + 3.9 a_2 + 3.6 b_2 \cdot c_3 + 3.6 b_2 + 3.6 c_3 + 3.6 - 3.9 c_2 \cdot a_3 - 3.6 c_2 \cdot b_3\right)^2}{\left(c_3 + 1\right)^2} = 51.80404169250000000$$

$$\frac{\left(3.9 a_1 \cdot b_2 + 3.9 a_1 + 3.3 c_1 \cdot b_2 + 3.3 c_1 + 3.9 b_2 + 3.9 - 3.9 b_1 \cdot a_2 - 3.3 b_1 \cdot c_2\right)^2}{\left(b_2 + 1\right)^2} + \frac{\left(3.9 a_2 \cdot c_3 + 3.9 a_2 + 3.6 b_2 \cdot c_3 + 3.6 b_2 + 3.6 c_3 + 3.6 - 3.9 c_2 \cdot a_3 - 3.6 c_2 \cdot b_3\right)^2}{\left(b_2 + 1\right)^2} = 53.1777766906648216$$

$$\frac{\left(3.6 a_1 \cdot b_2 + 3.6 b_2 + 3.3 c_2 \cdot a_1 + 3.3 c_2 + 3.6 a_1 + 3.6 - 3.6 b_1 \cdot a_2 - 3.3 a_2 \cdot c_1\right)^2}{\left(a_1 + 1\right)^2} + \frac{\left(3.6 b_3 \cdot a_1 + 3.6 b_3 + 3.3 a_1 \cdot c_3 + 3.3 c_3 + 3.3 a_1 + 3.3 - 3.6 a_3 \cdot b_1 - 3.3 c_1 \cdot a_3\right)^2}{\left(a_1 + 1\right)^2} = 44.8708998045411926$$

$$\mathrm{MinErr}(a_1, a_2, a_3, b_1, b_2, b_3, c_1, c_2, c_3) = \begin{pmatrix} 0.063 \\ 0.425 \\ 0.426 \\ 0.638 \\ 0.427 \\ 0.498 \\ 0.715 \\ 0.518 \\ 0.378 \end{pmatrix}$$

The approximate solution is set as the initial values, the optimization performed in the MatLab.

x0=[0.063 0.425 0.426 0.638 0.427 0.498 0.715 0.518 0.378]'

The results:

f =

1.0e-004 *

-0.2675 0.0231 0.0380 0.0490 -0.0053 -0.0005 0.0554 -0.0060 -0.0189

f =

1.0e-004 *

Columns 1 through 9

-0.2675 0.0231 0.0380 0.0490 -0.0053 -0.0005 0.0554 -0.0060 -0.0189

Columns 10 through 11

0 0.0084

f =

1.0e-004 *

Columns 1 through 9

-0.2675 0.0231 0.0380 0.0490 -0.0053 -0.0005 0.0554 -0.0060 -0.0189

Columns 10 through 12

0 0.0084 -0.0015

Optimization terminated: magnitude of search direction less than TolX.

x =

0.2641

0.4756

0.5018

0.6573

0.4744

0.5105

0.8444

0.5952

0.6395

Change the initial values:

x0=[0.1 0.4 0.4 0.5 0.5 0.5 0.7 0.5 0.4]'

The results:

f =

1.0e-004 *

-0.2677 0.0231 0.0365 0.0491 -0.0054 -0.0010 0.0557 -0.0025 -0.0184

f =

1.0e-004 *

Columns 1 through 9

-0.2677 0.0231 0.0365 0.0491 -0.0054 -0.0010 0.0557 -0.0025 -0.0184

Columns 10 through 11

0 0.0057

f =

1.0e-004 *

Columns 1 through 9

-0.2677 0.0231 0.0365 0.0491 -0.0054 -0.0010 0.0557 -0.0025 -0.0184

Columns 10 through 12

0 0.0057 0.0055

Optimization terminated: directional derivative along

search direction less than TolFun and infinity-norm of

gradient less than 10*(TolFun+TolX).

x =

0.2641

0.4756

0.5018

0.6573

0.4744

0.5105

0.8444

0.5952

0.6395

Change the initial values

x0=[0.1 0.1 0.1 0.1 0.1 0.1 0.1 0.1 0.1]'

The results:

f =

1.0e-004 *

Columns 1 through 9

-0.2676 0.0232 0.0370 0.0489 -0.0054 -0.0141 0.0548 -0.0018 -0.0227

Columns 10 through 11

0 0.0525

f =

1.0e-004 *

Columns 1 through 9

-0.2676 0.0232 0.0370 0.0489 -0.0054 -0.0141 0.0548 -0.0018 -0.0227

Columns 10 through 12

0 0.0525 0.0233

Optimization terminated: magnitude of search direction less than TolX.

x =

0.2551

0.6756

0.8018

0.6573

0.4345

0.7105

0.9444

0.6952

-0.6895

Appendix D. Position Coordinates of the Thermocouples

A total of 56 thermocouples were used in the experiments. The position coordinates of the thermocouples are displayed in Table D-1.

Table D-1 The Locations of the thermocouples.

Hole Number	X(mm)	Y (mm)	Depth (mm)	Hole Number	X (mm)	Y (mm)	Depth (mm)
1	0	203.2	3.35	29	10.14999	584.2	1.75
2	8.749995	228.6	3.35	30	-10.1501	584.2	1.75
3	-8.75005	228.6	3.35	31	8.749995	609.6	1.75
4	5.799988	254.0	3.35	32	-8.75005	609.6	1.75
5	-5.80009	254.0	3.35	33	6.849999	635.0	1.75
6	3.350006	279.4	3.35	34	-7.10006	635.0	1.75
7	-3.70002	279.4	3.35	35	3.350006	660.4	1.75
8	1.299997	304.8	3.35	36	-3.70002	660.4	1.75
9	-1.89992	304.8	3.35	37	10.14999	685.8	1.15
10	0	330.2	2.90	38	-10.1501	685.8	1.15
11	10.14999	355.6	2.85	39	8.749995	711.2	1.15
12	-10.1501	355.6	2.85	40	-8.75005	711.2	1.15
13	8.749995	381.0	2.85	41	5.799988	736.6	1.15
14	-8.75005	381.0	2.85	42	-5.80009	736.6	1.15
15	6.849999	406.4	2.85	43	10.14999	762.0	0.65
16	-7.10006	406.4	2.85	44	-10.1501	762.0	0.65
17	4.519981	431.8	2.85	45	9.649993	787.4	0.65
18	-4.64998	431.8	2.85	46	-9.64997	787.4	0.65
19	1.319987	457.2	2.85	47	8.749995	812.8	0.65
20	-1.84988	457.2	2.85	48	-8.75005	812.8	0.65
21	10.14999	482.6	2.35	49	6.849999	838.2	0.65
22	-10.1501	482.6	2.35	50	-7.10006	838.2	0.65
23	8.749995	508.0	2.35	51	10.14999	863.6	0.05
24	-8.75005	508.0	2.35	52	-10.1501	863.6	0.05
25	5.799988	533.4	2.35	53	9.649993	889.0	0.05
26	-5.80009	533.4	2.35	54	-9.64997	889.0	0.05
27	2.319985	558.8	2.35	55	8.749995	914.4	0.05
28	-2.75006	558.8	2.35	56	-8.75005	914.4	0.05

Appendix E. Tool Dimension

The tool dimension is demonstrated in Figure E-1

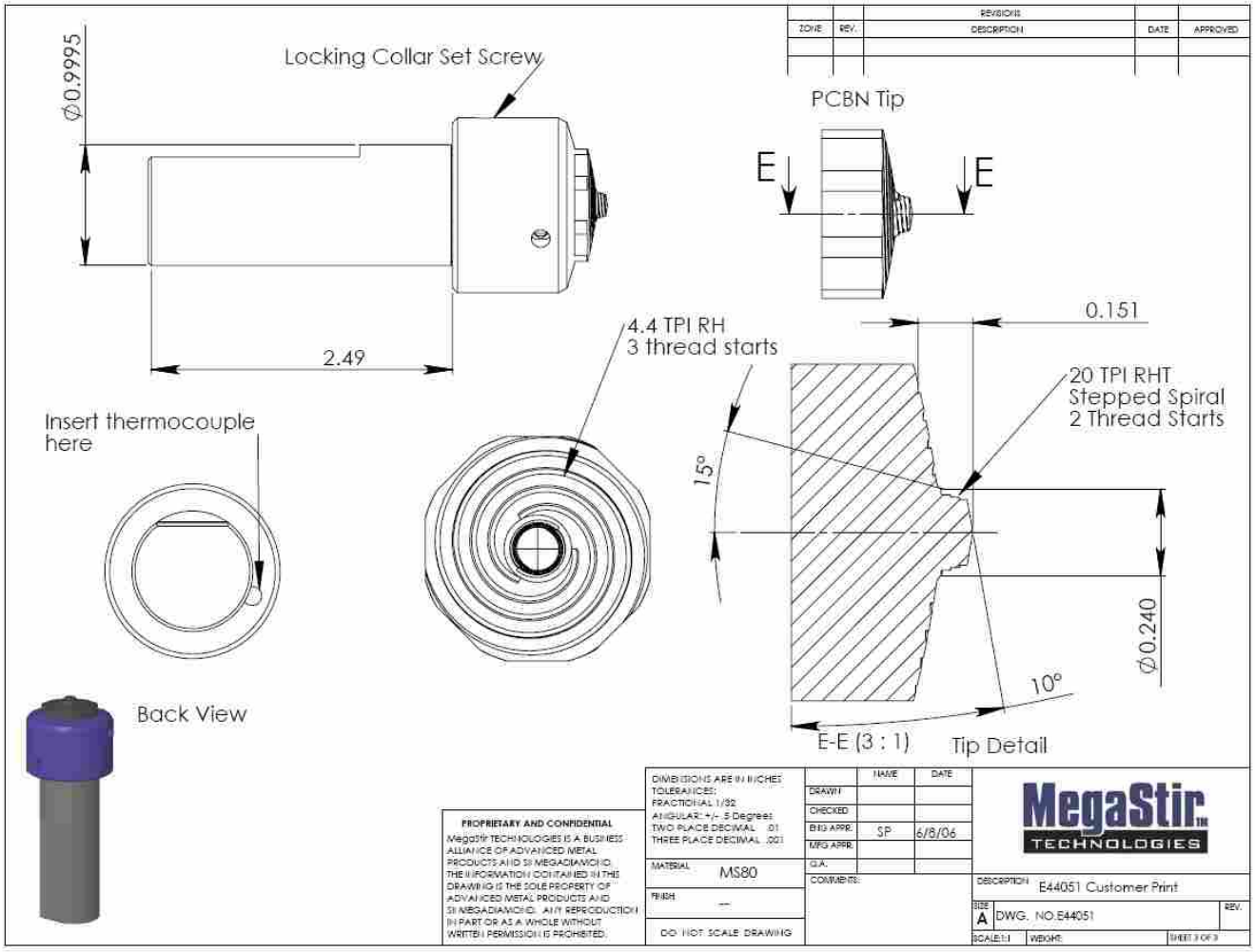

Figure E-1 The tool dimension